International Journal of Mechanical Sciences 331 (2026) 112212

Contents lists available at ScienceDirect

International Journal of Mechanical Sciences

journal homepage: www.elsevier.com/locate/ijmecsci

# Microstructure-informed ICME framework for laser-assisted flange forming of S700 steel

Karthik Ramalingam [a,*], Tobias Schmid [b], Bohang Gao [a], Florian Hüsing [b], Christian Haase [c], Christian Brecher [b,d], Ulrich Krupp [a]

[a] RWTH Aachen University, IEHK Steel Institute, Intzestrasse 1, Aachen, D-52072, Germany
[b] Fraunhofer Institute for Production Technology IPT, Steinbachstrasse 17, Aachen, D-52074, Germany
[c] TU Berlin, Chair Materials for Additive Manufacturing, Ernst-Reuter-Platz 1, Berlin, D-10587, Germany
[d] RWTH Aachen University, Laboratory for Machine Tools and Production Engineering WZL, Campus-Boulevard 30, Aachen, D-52074, Germany

ARTICLE INFO

*Keywords:*
ICME
Process-chain simulation
Sheet metal forming
Flange forming process
Dislocation density
S700MC

ABSTRACT

In multi-step sheet metal forming, the deformation and damage state inherited from upstream operations can govern failure during subsequent processing. Conventional process-chain simulations commonly transfer macroscopic quantities such as equivalent plastic strain, which do not uniquely represent the underlying microstructural state. This work presents an Integrated Computational Materials Engineering (ICME) framework for laser-assisted flange forming of S700MC steel, sequentially coupling shear cutting, localized laser heating, and flange forming through deterministic transfer of dislocation densities and void fraction as microstructural state variables (MSV) using a damage-integrated thermo-micro-mechanical (D-TMM) formulation. A circumferential binning procedure is introduced to quantify spatial variations of each field along the flange edge. The simulations reveal persistent damage localization near 35° and 70°, robust to circumferential discretization, evaluation-region height, and removal of one symmetry plane. A conventional formulation transferring equivalent plastic strain and void fraction predicts higher mean plastic strain but does not reproduce this localization. D-TMM control simulations show that the shear-sensitive damage contribution is required for the angular damage pattern, while transferred MSVs increase its severity. Increasing the forming-zone temperature from approximately 350 °C to 550 °C reduces numerical fracture by about 72%, while blank inversion yields an overall reduction of about 85% relative to the 350 °C condition. Representative experiments support the predicted response through forming-force and flange-thickness comparisons. The mean grain aspect ratio decreases from 4.55 to 2.47 from cold to laser-assisted forming, while simulated wall-immobile dislocation densities are of the same order of magnitude as EBSD-derived GND densities, differing by approximately a factor of 1.4. The framework therefore provides a microstructure-informed basis for assessing edge fracture in sequential forming processes.

## 1. Introduction

The development of advanced manufacturing strategies for high-strength steels increasingly relies on the ability to predict, rather than empirically discover, how each step of a forming chain shapes the microstructure and damage state of the final component. This introduction positions the present work within three connected bodies of literature. First, the experimental and numerical understanding of edge formability in shear-cut (blanked) high-strength sheet steels is reviewed, with emphasis on the role of shear-cutting damage in the subsequent flange forming process. Second, recent process-chain simulation efforts that attempt to inherit upstream manufacturing history into downstream forming models are critically discussed, examining the variables used to represent the inherited material state. Third, Integrated Computational Materials Engineering (ICME) approaches for metal forming process chains are surveyed, with attention to where physics-based microstructural state variables (MSVs) have not been transferred between process steps. The section closes with a statement of the gap addressed by the present work.

* Corresponding author.
*E-mail address:* karthik.ramalingam@iehk.rwth-aachen.de (K. Ramalingam).

https://doi.org/10.1016/j.ijmecsci.2026.112212
Received 7 July 2026; Received in revised form 3 October 2026; Accepted 10 October 2026
Available online 12 October 2026
0020-7403/© 2026 The Author(s). Published by Elsevier Ltd. This is an open access article under the CC BY license (http://creativecommons.org/licenses/by/4.0/).
Open access funding enabled and organized by Projekt DEAL.

**Nomenclature**

| Symbol | Description |
|---|---|
| $A$ | Austenitizing temperature [$^{\circ}C$] |
| $C$ | Relative cut clearance – shear cutting process [%] |
| $D$ | Blank diameter [$mm$] |
| $G$ | Shear modulus [$MPa$] |
| $J$ | Deviatoric stress invariant; invariant-dependent units |
| $M$ | Taylor factor [− ] |
| $N$ | Number of angular bins [− ] |
| $\mathscr{N}$ | Set of active nodes [− ]; subscript $i$ identifies the angular bin |
| $P$ | Applied/ holding force with tooling subscripts [$N$] |
| $P$ | Percentile of the evaluated field; same units as that field |
| $Q$ | Laser power [W] |
| $R$ | Tool radius [$mm$] |
| $S$ | Standard deviation of the void-nucleation strain [− ] |
| $\boldsymbol{S}$ | Microstructural state-variable set [set of all $MSV$s] |
| $T$ | Temperature [$^{\circ}C$] |
| $V$ | Velocity [$mms^{-1}$] |
| $\mathscr{V}$ | Spatial region associated with an angular bin; its scalar volume is $\mathscr{V}_i$ [$mm^3$] |
| $b$ | Burgers vector magnitude [$m$] |
| $c$ | Dislocation-mechanism kinetic coefficient [− ] |
| $d$ | Pre-hole diameter or laser-profile diameter, as specified by its subscript [$mm$] |
| $f$ | Void fraction or characteristic fraction parameter - specified by subscript [− ] |
| $h$ | Flange height or flange-edge evaluation height, as specified [$mm$] |
| $k$ | Thermal conductivity [$Wm^{-1}K^{-1}$] |
| $m$ | Strain-rate sensitivity exponent [− ] |
| $n$ | Number of active nodes; subscript $i$ identifies the angular bin [− ] |
| $q$ | Tvergaard constant; $q_1$, $q_2$,$q_3$ [− ] |
| $r$ | Radial distance [$mm$] |
| $r$ | Temperature-sensitivity coefficient [− ]; with index |
| $s$ | Deviatoric stress component with tensor indices [$MPa$] |
| $s$ | Temperature sensitivity exponent [− ]; with index |
| $t$ | Time [$s$] or Sheet thickness [$mm$] |
| $x$ | Spatial position vector of a node in the deformed configuration [$mm$] |
| $\Phi$ | GTN yield function [− ] |
| $\Omega$ | Triaxiality-dependent weighting function for shear-sensitive damage [− ] |
| $\alpha$ | Dislocation interaction coefficient [− ] |
| $\varepsilon$ | Strain or characteristic nucleation strain, as specified [− ] |
| $\eta$ | Stress triaxiality; $\eta_1$ and $\eta_2$ are lower and upper threshold [− ] |
| $\kappa$ | Dissipation factor [− ] |
| $\lambda$ | Laser wavelength [$nm$] |
| $\mu$ | Friction coefficient [− ] |
| $\nu$ | Poisson's ratio [− ] |
| $\rho$ | Dislocation density [$m^{-2}$]; mass density [$Kgm^{-3}$] |
| $\sigma$ | Stress; its type is specified by subscripts or modifiers [$MPa$] |
| $\phi$ | Circumferential angle [$^{\circ}$] |
| $\psi$ | Generic evaluated field; units depend on the field. |
| $\omega$ | Lode-dependent weighting function for shear-sensitive damage [− ] |

| Modifiers | Description |
|---|---|
| $\dot{a}$ | Time derivative |
| $\overline{a}$ | Equivalent quantity for stress and plastic strain; arithmetic bin mean for $\psi$. |
| $\widehat{a}$ | Normalized quantity |
| $\widetilde{a}$ | Effective dislocation interaction strength when applied to $\alpha$ |
| $\Delta a$ | Increment or interval |
| $f^*$ | Modified void fraction |
| $K'$ | Effective shear-damage coefficient |
| $\boldsymbol{a}$ | Vector, tensor, or state-variable set, as defined for the quantity. |

| Index | Description |
|---|---|
| $BH$ | Blank holder |
| $f_{index}$ | Contributions: $g - growth$, $n - nucleation$, $s - shear$ |
| $f_{index}$ | Fractions: $C - critical$, $F - failure$ |
| $P$ | Punch |
| $cm$ | Cell mobile |
| $ci$ | Cell immobile |
| $wi$ | Wall immobile |
| $an$ | Annihilation |
| $ac$ | Accumulation |
| $nc$ | Nucleation |
| $rm$ | Remobilization |
| $gn$ | Generation |
| $tr$ | Trapping |
| $z$ | Process – $an$, $ac$, $nc$, $rm$, $gn$, $tr$ |
| $p$ | Plastic |
| $c1$, $c3$ | Critical transformation temperatures |
| $x$ | Cell, wall or total ($x = c, w, t$) |
| $i$ | Circumferential bin of interest |
| $\prime$ | Spatial position of node of interest |
| $d$ | Die part |
| $\boldsymbol{v}$ | Viscous contribution |
| $y$ | Yield stress |
| $pc$, $pw$ | Plastic stress from cell and wall dislocations |
| $max$, $min$ | Maximum and minimum, respectively |
| $h$ | Hydrostatic stress |
| 0 | Reference/ initial state |
| 10, 90 | Percentile levels: 10th and 90th |

| Abbreviation | Description |
|---|---|
| $AHSS$ | Advanced high strength steel |
| $DP$ | Dual phase steel |
| $D - TMM$ | Damage integrated thermo-micro-mechanical |
| $EBSD$ | Electron backscatter diffraction |
| $FE$ | Finite element |
| $FLC$ | Forming limit curve |
| $GND$ | Geometrically necessary dislocations |
| $GTN$ | Gurson-Tvergaard-Needleman |
| $HSLA$ | High strength low alloy steel |
| $ICME$ | Integrated computational materials engineering |
| $IE$ | Internal energy |
| $IPF$ | Inverse pole figure |
| $KAM$ | Kernel average misorientation |
| $KE$ | Kinetic energy |
| $MSV$ | Microstructural state variables |
| $ND$ | Normal direction |
| $OES$ | Optical emission spectroscopy |
| $PEEQ$ | Equivalent plastic strain |
| $PF$ | Pole figure |
| $SAZ$ | Shear affected zone |
| $SDV$ | State-dependent variable |
| $SEM$ | Scanning electron microscopy |
| $TMM$ | Thermo-micro-mechanical |
| $TRIP$ | Transformation induced plasticity |
| $VUMAT$ | Vectorized user material |
| $VVF$ | Void volume fraction |

### 1.1. Edge formability and shear-cutting damage in high strength steel sheets

High strength low alloy (HSLA) steel grades are widely used in automotive and structural applications as they combine a high strength-to-weight ratio with sufficient cold formability for industrial sheet processing [1–3]. Typical components, including chassis frames, longitudinal beams, subframes, suspension arms, and cross-members, are produced through cold-forming sequences that combine bending, roll forming, stamping, and stretch flanging. Within these sequences, trimming and shear cutting are usually performed before secondary operations such as hole flanging. Shear cutting introduces severe localized plastic deformation and strain hardening in the edge region, accompanied by micro-damage in the form of microcracks and voids, which substantially reduces edge formability and can cause premature fracture in subsequent forming steps [4,5].

The broader literature on edge formability in high-strength sheet steels covers both material-related damage resistance and the influence of edge preparation. Uthaisangsuk et al. [6] investigated damage and failure in multiphase DP and TRIP steels through constitutive modelling. Overby et al. [7] specifically examined the effects of alloy design and edge preparation on hole expansion in hot-rolled HSLA steel, and Kamibayashi et al. [8] investigated the influence of Ti and Nb on the strength–ductility–hole-expansion balance of hot-rolled high-strength steel. Paul et al. [9] developed a predictive description of the hole-expansion ratio for automotive steels. Adamczyk and Michal [10] used hole-expansion tests to examine how edge preparation, microstructure and tensile properties influence the edge formability of high-strength cold-rolled steels. Gläsner et al. [11] investigated two-stage shear cutting to reduce edge-cracking susceptibility. Comstock et al. [12] compared hole-expansion behavior across different sheet steels, while Centeno et al. [13] and Bambach et al. [14] investigated hole-flanging using incremental sheet-forming approaches in AA1050 aluminum and DC04 steel, respectively. Studies of sheared and trimmed sheet edges show that cutting-induced plastic deformation and microdamage can reduce subsequent edge stretchability and promote premature fracture [15–18]. More recent work has refined this picture by characterizing the cut edge in greater detail. Han et al. [19] systematically compared six damage models against microstructural observations of the shear-affected zone (SAZ) in QP980 steel, identifying microvoids at phase interfaces and inclusion sites as important damage features associated with edge cracking. Ortiz-Membrado et al. [20] mapped cut-edge hardness using high-speed nanoindentation and assessed local residual stresses using FIB–DIC, and Larour et al. [21] documented circumferential edge heterogeneity and its sensitivity to slight tool misalignment. The latter observation directly motivates the circumferential analysis approach adopted later in the present work.

Beyond cutting parameters, hole flangeability is sensitive to a broad set of material and process variables [22], including the microstructural state [23–25], plastic anisotropy and strain-hardening behavior [9], punch geometry (expansion-punch and piercing-punch) [26,27] as well as the quality of the pre-hole, which depends, for example, on the process and the cutting clearance [28–30]. The interaction between these factors and the shear-cutting damage state is what makes physically based prediction of edge formability difficult, and it is what motivates the integrated process-chain modelling effort described in the next subsection.

### 1.2. Process-chain simulation of cold forming with upstream damage transfer

A growing body of work has attempted to incorporate the upstream cutting history into downstream forming simulations rather than treating each process step as isolated. As reviewed in [31], finite element (FE) studies have investigated hole-flanging configurations [32–34], including approaches that carry stress, strain or fracture history from blanking into subsequent forming [32,33]. Earlier generations of process-chain models addressed this approach by transferring geometric edge features and macroscopic deformation measures from the blanking stage to the subsequent forming simulation. Hu et al. [35] developed an integrated FE framework linking hole piercing to hole expansion, mapping accumulated plastic strain and edge geometry to predict edge stretchability. Wang et al. [5] proposed a pre-damage mapping model that transfers equivalent plastic strain and a phenomenological damage variable from a 2D axisymmetric blanking simulation to a 3D hole expansion simulation, demonstrating substantially improved edge fracture prediction for DP780. He et al. [36] used edge-hardness measurements to initialize clearance-dependent pre-hardening distributions in a central-hole tensile simulation of DP590. Park et al. [37] developed a dual-scale FE approach in which the macroscopic hole expansion simulation, informed by the measured edge geometry and hardness profile, transfers its deformation history to a microscale simulation that captures localized inhomogeneous deformation at the level of the ferrite-bainite microstructure. Li et al. [38] developed a ductile fracture model for ultra-high strength steel that maps a phenomenological initial damage value derived from blanking conditions onto the initial state of the downstream edge forming simulation. Qian et al. [39] incorporated blanking-generated edge irregularities into a TRIP800 hole-flanging model, capturing their effect on local stress concentration and edge fracture. Most recently, Sandin et al. [30] applied the particle finite element method to simulate shear cutting of complex-phase steel, transferring edge geometry and residual fields including equivalent plastic strain to subsequent hole expansion simulations through a GISSMO damage model with a modified Mohr–Coulomb failure locus. Within the investigated input ranges, Pham et al. [40] complemented these deterministic frameworks with an uncertainty-quantification study of conical hole expansion in DP800, identifying the maximum punching-induced pre-strain and pre-damage distribution in the SAZ as dominant contributors to the scatter in the predicted hole expansion ratio. A parallel data-driven line of work, exemplified by Jeong et al. [41], correlates image features of the sheared edge with the hole expansion ratio in AHSS, providing fast empirical predictions but without explicitly evolving damage mechanisms in a constitutive process-chain simulation. Beyond conventional single-stage processes, Seyyedi et al. [42] applied a modified Mohr-Coulomb criterion with a nonlinear damage accumulation law to predict fracture in single- and multi-stage incremental hole flanging of aluminum sheets, showing the importance of path-dependent damage accumulation for the investigated multi-stage forming sequences.

These contributions represent the current state of the art in process-chain simulation of cold sheet forming and demonstrate the importance of inherited edge state for predicting subsequent forming. Several approaches describe this state using equivalent plastic strain, phenomenological damage variables, or hardness distributions, while others also incorporate microscale heterogeneity [35,37]. However, these quantities do not fully characterize the underlying microstructural state. Equal accumulated plastic strains reached through different temperature and strain-rate histories need not produce the same dislocation state or subsequent stress response [43,44], while hardness reflects several strengthening contributions and provides only an indirect measure of microstructure. These limitations become particularly relevant when localized heating is introduced between shear cutting and subsequent forming. Localized laser heating around a punched pre-hole has been investigated for hole flanging of DP1000 steel [45], and experiments on S700MC showed crack-free flange formation with laser-preheating, whereas the corresponding cold-forming condition produced severe cracking [46]. Lower forming forces have also been reported for other laser-assisted forming operations [47,48]. Although these studies demonstrate the potential of localized heating, the combined influence of the inherited shear-cut edge state and subsequent thermal treatment on HSLA edge formability remains insufficiently understood. This motivates process-chain frameworks that explicitly represent and transfer

microstructural state variables between successive manufacturing stages.

### 1.3. ICME frameworks and the transfer of microstructural state across forming chains

Capturing both macroscopic deformation and microstructural evolution within a single simulation framework requires constitutive models that retain a physically meaningful state variable through the process chain. In our previous work, a damage-integrated thermo-micro-mechanical (D-TMM) model [49] was developed, building on the dislocation-density-based framework of Motaman et al. [43,44], to describe the coupled evolution of dislocation densities and ductile damage during plastic deformation. The model was first formulated and calibrated to reproduce the strain hardening and damage response of single-phase S700 steel [49], and was subsequently applied to simulate shear cutting and flange forming as separate processes [31]. Validation through electron backscatter diffraction (EBSD) and scanning electron microscopy (SEM) confirmed that the framework captures the evolution of deformation substructures and damage during forming, supporting the use of dislocation densities and void fraction as physically grounded state variables. In these earlier studies, however, blanking and flanging were treated as independent simulations: the initial microstructural state for each process was prescribed rather than inherited from the preceding manufacturing step. The deformation history and the microstructural state generated during cutting were therefore not transferred to the subsequent flanging simulation, and the influence of localized thermal treatments such as laser-assisted edge heating was not considered. Closing this gap requires a structured framework for propagating MSVs across sequential process steps, which is the role that ICME fulfills.

ICME has emerged as a paradigm for connecting processing conditions, microstructural evolution, and component performance across length scales [50–53]. Its application spans several manufacturing routes. In steel casting, CALPHAD-based microstructure calculations have been coupled with FE thermal simulations [54], while additive-manufacturing frameworks integrate process simulation with microstructure, material properties and performance [55]. The broader ICME developments have addressed integrated product-production engineering and the software infrastructure required to connect heterogeneous models and data [56,57]. For metal forming, an early contribution by Karhausen and Kopp [58] linked microstructure evolution during hot deformation to history-dependent flow stress through a semi-empirical model designed for coupling with incremental process simulations. Subsequent studies addressed through-process microstructure modelling and integrated hot-forging workflows [59,60]. Related ICME developments have addressed thermochemical heat-treatment chains, including integrated carburizing–quenching–tempering of steel gears [61] and carbon redistribution and precipitation during high-temperature case hardening [62]. Microstructure-informed ICME approaches have also been extended to downstream forming, including the influence of ferrite-pearlite microstructure on U–O forming simulations of pipeline steels [63].

A central challenge in ICME is the translation of microstructural features into macroscopic material behavior [64]. Crystal plasticity models capture anisotropic deformation and support prediction of macroscopic yield behavior [65–69]. EBSD-informed virtual crystal-plasticity tests have been used to generate yield points and fit macroscopic anisotropic yield functions [65]. Representative volume elements (RVE) based crystal plasticity simulations have also been employed as virtual experiments for calibrating macroscopic damage and fracture models. Mirnia [70] combined crystal-plasticity RVE calculations with an experimentally calibrated macroscopic fracture locus for AA6061-T6 and showed that local damage distributions depend strongly on stress state. The computational expense of full-field crystal plasticity nevertheless remains a barrier to deployment in large-scale process simulations. Homogenization-based approaches provide a route for incorporating microstructural information into component-scale forming simulations [71,72].

Microstructural information can also enter constitutive models through internal state variables, such as dislocation density. Such formulations have been applied to describe hardening behavior in micro-alloyed steels [73], while in-situ SEM/EBSD observations during tension have linked ferrite–bainite morphology to localized deformation and orientation gradients in HSLA steels [74]. These studies complement process-chain approaches that transfer geometric and material-state information from cutting to subsequent edge forming [5,30,36,37,39]. Together, they motivate the present study, which incorporates void fraction and dislocation-density-based state variables into a process chain comprising shear cutting, localized heating, and flange forming.

The constitutive model and the individual mechanical-process models used in the present framework were established in the authors' previous studies [31,49]. The D-TMM constitutive model, including the dislocation-density evolution laws, GTN-based damage formulation, material calibration, and VUMAT implementation, was developed in [49]. Its application to shear cutting and flange forming as separate simulations, together with EBSD and SEM validation of the resulting microstructural states, was reported in [31]. The constitutive formulation and the individual shear-cutting and flange-forming model formulations are retained from these studies. Building on the project-level process-chain development documented in [75], the present work examines the coupling of the previously independent simulations through deterministic transfer of the MSV set ($\rho_{cm}$, $\rho_{ci}$, $\rho_{wi}$, $f$), incorporating localized laser heating as an intermediate process step, and introducing a circumferential binning procedure for evaluating the resulting heterogeneous three-dimensional fields.

### 1.4. Objectives and organization of the present work

Accordingly, the present study investigates how the cutting-induced microstructural state and localized thermal condition influence damage evolution during subsequent flange forming of S700MC steel. Controlled numerical cases are used to distinguish the effects of inherited MSVs, the shear-sensitive damage contribution, forming temperature, and blank orientation. The process-chain predictions are assessed at complementary scales using the standalone cold-forming force response, representative flange-thickness profiles, and EBSD/SEM characterization of cold- and laser-assisted components.

The remainder of the paper is organized as follows. Section 2 summarizes the D-TMM constitutive equations in the form used throughout the process chain. Section 3 describes the material, the experimental procedures including the progressive tool, and the simulation setup. Section 4 presents the two methodological contributions of the work: the deterministic variable-transfer procedure and the circumferential statistical binning method. Section 5 describes the implementation of sequential shear-cutting, laser-heating, and flange-forming simulations. Section 6 presents the numerical and experimental results, Section 7 discusses the physical interpretation, validation scope, and limitations of the framework and Section 8 presents the conclusions of the framework for the physics-based design of multi-stage forming chains.

## 2. D-TMM constitutive model for process-chain simulations

The constitutive description used at every integration point in the present ICME framework is the D-TMM model, previously developed and calibrated for S700MC steel [31,49]. The complete derivation of the model, its calibration against thermo-mechanical tests, and its standalone validation for shear cutting and flange forming are reported in those works and are not repeated here. The present section restates the equations required to identify the MSVs that are transferred between successive simulation steps in the framework of Sections 4 and 5; the full set of parameter expansions, mechanism and damage kinetics are given in Appendix A. The model couples macroscopic FE simulations to the

evolution of dislocation densities and void fraction through a GTN yield surface and a temperature- and strain-rate-dependent flow stress decomposition. Plastic yielding under combined deviatoric and hydrostatic loading is described by the GTN criterion,

$$\Phi = \left(\frac{\bar{\sigma}}{\sigma_y}\right)^2 + 2q_1 f^* cosh\left(\frac{-3q_2\sigma_h}{2\sigma_y}\right) - \left(1 + q_3 f^{*2}\right) = 0, \quad (1)$$

where $\bar{\sigma}$ is the equivalent stress, $f^*$ is the modified void fraction (Eq. (A.4)), $\sigma_h$ is the hydrostatic stress, $\sigma_y$ is the yield stress, and $q_1$, $q_2$ and $q_3$ are calibration constants [76]. The macroscopic yield stress $\sigma_y$ depends on temperature, strain rate, and the evolving MSVs, and is expressed as [44]:

$$\sigma_y = \breve{\sigma}_y(T, \boldsymbol{S}, \dot{\bar{\varepsilon}}_p) = \sigma_v + \sigma_p, \quad (2)$$

where $\sigma_v$ is the viscous stress (Eqs. (A.1)-(A.3)) and $\sigma_p$ is the plastic contribution arising from the dislocation structure. The plastic stress follows the Taylor relation [44]:

$$\sigma_{px} = MbG\widetilde{\alpha}_x\sqrt{\rho_{xi}}\ , x = c, w, \quad (3)$$

$$G\widetilde{\alpha}_x = G_0\widetilde{\alpha}_{x0}\left[1 + r^G_{ax}(\widehat{T} - 1)^{s^G_{ax}}\right],\ r^G_{ax}\langle 0,\ \ s^G_{ax}\rangle\ 0, \quad (4)$$

where $\rho_{xi}$ is the immobile dislocation density (can be cell or wall type), $\widetilde{\alpha}_x$ is the non-local interaction strength related to local density and geometrical arrangement of immobile dislocations of cell and wall species, $b$ is the Burgers vector and $M$ is the Taylor factor ($M \cong 3$). The MSV set $\{\rho_{cm}, \rho_{ci}, \rho_{wi}, f\}$ evolves through balance equations coupling the three dislocation populations (as normalized values $\widehat{\rho}_{xy} = \rho_{xy}/\rho_0$, with $\rho_0$ from Table C.1) and void fraction,

$$\dot{\widehat{\rho}}_{wi} = \dot{\widehat{\rho}}^{nc}_{wi} + \dot{\widehat{\rho}}^{ac}_{wi} + \left(-\dot{\widehat{\rho}}^{an}_{wi} - \dot{\widehat{\rho}}^{rm}_{wi}\right), \quad (5)$$

$$\dot{\widehat{\rho}}_{ci} = \dot{\widehat{\rho}}^{tr}_{cm} + \dot{\widehat{\rho}}^{ac}_{ci} + \left(-\dot{\widehat{\rho}}^{an}_{ci} - \dot{\widehat{\rho}}^{rm}_{ci} - \dot{\widehat{\rho}}^{nc}_{wi}\right), \quad (6)$$

$$\dot{\widehat{\rho}}_{cm} = \dot{\widehat{\rho}}^{gn}_{cm} + \dot{\widehat{\rho}}^{rm}_{ci} + \dot{\widehat{\rho}}^{rm}_{wi} + \left(-2\dot{\widehat{\rho}}^{an}_{cm} - \dot{\widehat{\rho}}^{an}_{ci} - \dot{\widehat{\rho}}^{an}_{wi} - \dot{\widehat{\rho}}^{ac}_{ci} - \dot{\widehat{\rho}}^{ac}_{wi} - \dot{\widehat{\rho}}^{tr}_{cm}\right), \quad (7)$$

$$\dot{f} = \dot{f}_g + \dot{f}_n + \dot{f}_s, \quad (8)$$

whose mechanism rates (generation, annihilation, accumulation, trapping, nucleation, and remobilization) together with their temperature and strain-rate dependence are detailed in Eqs. (A.5)-(A.12). The void fraction evolves through three additive contributions corresponding to growth of existing voids, nucleation of new voids at inclusions or precipitate interfaces, and shear-induced void distortion under low-triaxiality loading (Eqs. (A.13)-(A.16)).

## 3. Material and methods

This section describes the material, the experimental procedures, and the numerical workflow used to realize the ICME-based simulation of laser-assisted flange forming of S700MC steel.

### 3.1. Material and initial microstructure

The investigated material is S700MC, a thermomechanically processed high-strength low-alloy steel with a predominantly ferritic single-phase microstructure. The chemical composition, determined by optical emission spectroscopy (OES), is given in Table 1.

The initial microstructure is summarized in Fig. 1. SEM imaging (Fig. 1b) reveals an equiaxed ferritic grain structure. EBSD analysis quantifies the grain size distribution (Fig. 1c) and the GND density derived from kernel average misorientation (KAM) of the as-received material (Fig. 1d), which serves as the reference state for the KAM analysis after each process step. The inverse pole figure (IPF) indicates a weak, near-random crystallographic texture (Fig. 1a), justifying the use of an isotropic yield function in the D-TMM implementation. Temperature-dependent thermophysical properties (density, thermal expansion coefficient, specific heat capacity, and shear modulus) were calculated using JMatPro from the measured composition according to Table 1 and are listed in Appendix B (Fig. B.1). The constitutive parameters used in D-TMM models are listed in Appendix C (Table C.1, C.2, C.3, C.4, Table C.5).

### 3.2. Experimental methods

This subsection describes the laser-assisted flange forming process, the progressive tool used for experimental validation, and the microstructural characterization procedures applied after each process step.

#### 3.2.1. Laser-assisted flange forming process

Laser-assisted flange forming experiments were carried out on a multi-stage progressive die that combines shear cutting, localized laser heating and flange forming (Fig. 2), together with the auxiliary operations required for the process. The localized heating stage is introduced between cutting and flanging to increase the local formability of the shear-affected edge and reduce the tendency for fracture during the subsequent flange forming.

In the cutting stage, a circular blank of diameter $D$ is clamped between two blank holders applying force $P_{BH}$, and a cylindrical punch advancing at velocity $V_P$ produces a pre-hole of diameter $d_i$ through controlled separation. In the second stage, a laser beam is formed by a freeform mirror [46] to a ring-shaped irradiation of outer diameter $d_h > d_i$, which is applied concentrically around the cut edge, generating localized thermal softening within the SAZ while limiting the thermal exposure of the surrounding sheet. In the third stage, a forming punch advancing at velocity $V_P$ deforms the locally heated edge region radially and axially to produce the flange, with the blank holder force maintained to control material flow. Tool geometries and process parameters are indicated in Fig. 2.

#### 3.2.2. Progressive tool for laser-assisted flange forming process

A progressive die system with localized laser heating (Fig. 3a) was designed to experimentally investigate laser-assisted flanging of S700MC steel sheets. The progressive die was integrated into the servo press, enabling the evaluation of flange quality under different forming conditions. The progressive die was designed to focus on flange quality, including aspects of crack initiation, necking, as well as edge quality after flanging.

The progressive die has four stations (Fig. 3(b–c)): (1) cup forming, (2) pilot hole shearing, (3) localized laser heating, and (4) flange forming. The progressive die has an idle station for integrating the heating module. The heating module (Fig. 3d) is designed to be integrated into the progressive die, enabling localized laser heating of the edge region of the sheet. The heating module was designed using a diode laser (Laserline LDF 4500–30 VGP, $\lambda = 940$–$1064$ nm, $Q_{max} = 4.5$ kW) [46]. The absorption coefficient of S700MC steel at these wavelengths was found to be in the range of 62–65% [75].

The heating ring was designed to use a replaceable mirror optic with

**Table 1**
Chemical composition of S700 steel (wt. %).

| Element | Fe | Mn | Si | Mo | Ti | Al | C | Nb | Cr | Ni | Cu |
|---|---|---|---|---|---|---|---|---|---|---|---|
| wt. % | 96.99 | 1.921 | 0.492 | 0.131 | 0.126 | 0.073 | 0.072 | 0.048 | 0.044 | 0.035 | 0.024 |

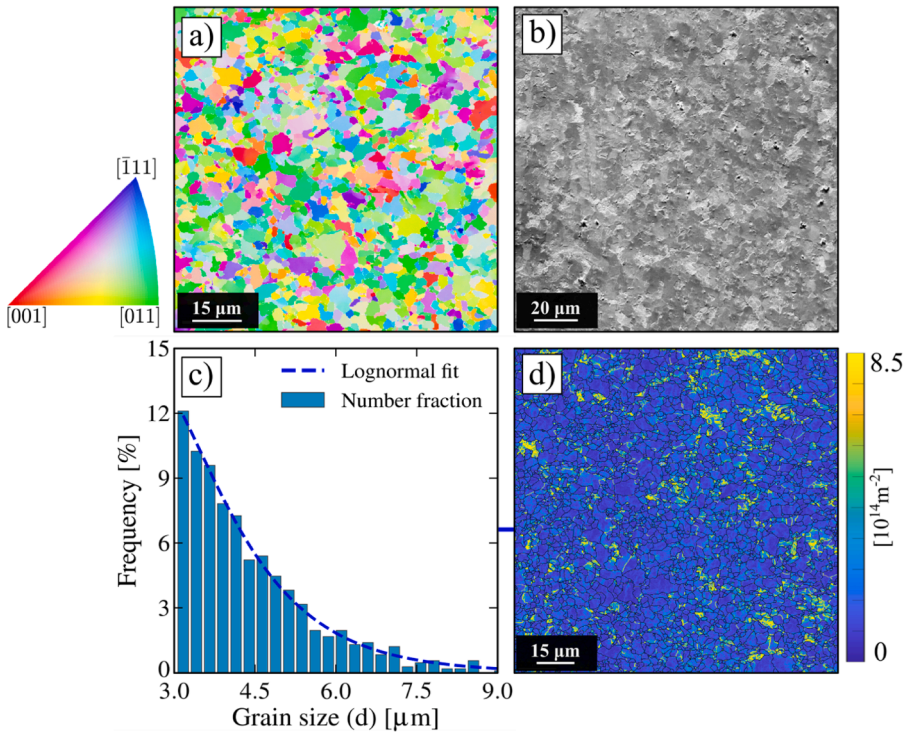



**Fig. 1.** Initial microstructure of S700MC: (a) IPF map; (b) etched SEM micrograph; (c) EBSD grain-size distribution; and (d) KAM derived GND map. Adapted from [31,49].

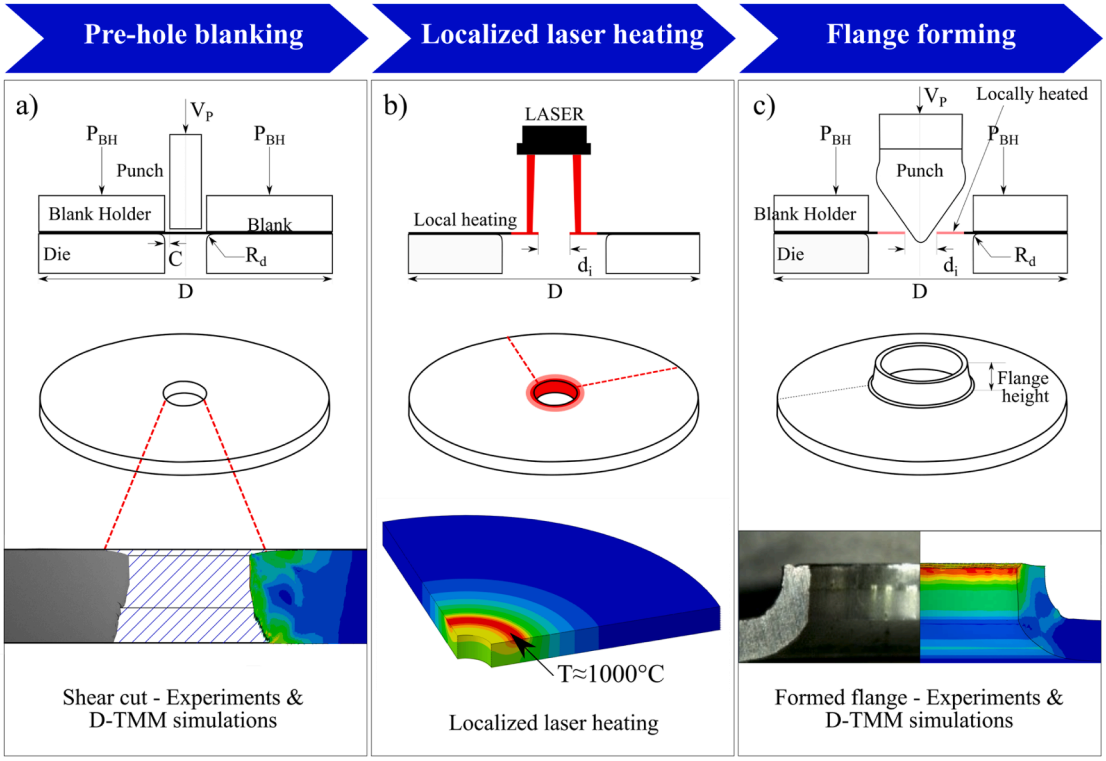



**Fig. 2.** Laser-assisted flange-forming sequence: (a) shear cutting; (b) localized laser heating; and (c) flange forming, with process setups and representative experimental and simulated results [31].

an inner ring diameter of 4.8 mm and an outer ring diameter of 13.0 mm [46], with a working distance of 170 mm, yielding a peak intensity of approximately 6.5 kWcm$^{-2}$. The upper part of the module contains collimation optics, a mirror holder, and an adjustable free-form mirror. The free-form mirror allows for adapting the heating geometry to various forming conditions. Further components include an integrated camera for monitoring the process and a pyrometer for temperature measurement. The system includes a cross-jet for laminar airflow to

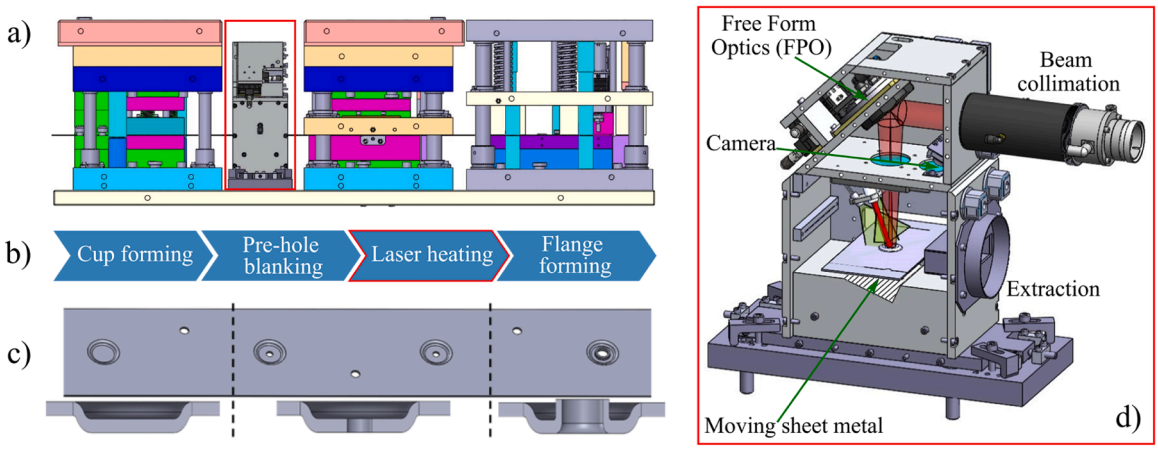



**Fig. 3.** (a) Progressive die design. The heating module is highlighted; (b) Process steps of the progressive die. The highlighted stage indicates the function of the integrated heating module; (c) The metal sheet layouts at each stage in top view and in cross sectional view; (d) hy-PRESS laser heating module.

protect optical components from overheating, an exhaust system for particle removal, and a radiation trap for operator safety. The compact form factor permits full integration into the progressive die, with adjustable parameters including stroke rate, laser power, and exposure time. By adjusting the press stroke rate, various thermo-mechanical interaction conditions during the flange forming process can be investigated. Under the selected operating condition of 30 strokes per minute, a laser power of 2 kW, and an exposure time of 1 s, representative components were formed without macroscopic edge cracking (Fig. 4c) [46].

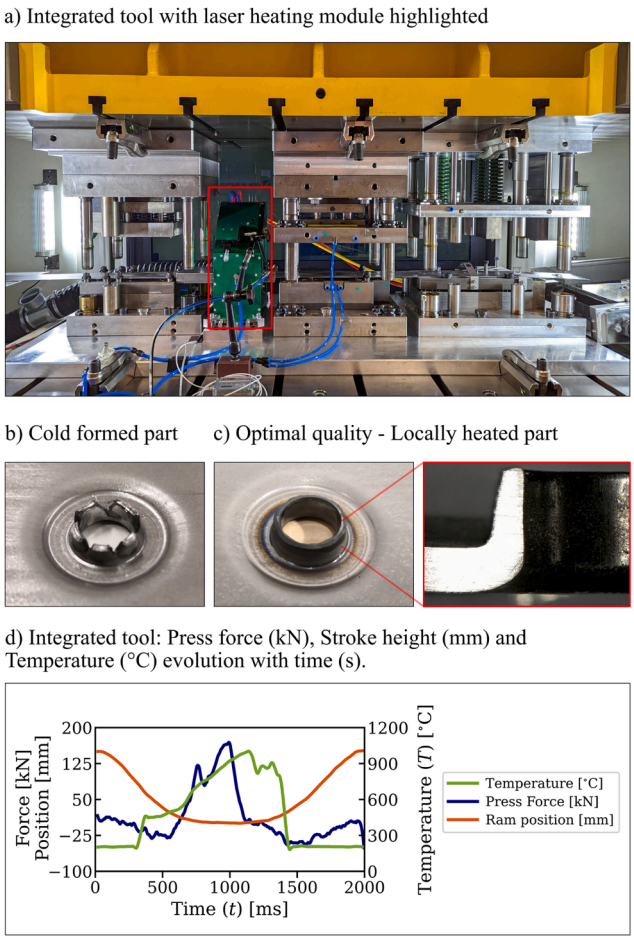



**Fig. 4.** Integration and operation of the hy-PRESS module. (a) Integrated tool; (b,c) cold- and laser-assisted formed parts; (d) press force, ram position and temperature histories [46].

### 3.2.3. Microstructural characterizations

Specimens were extracted from the deformation zones after shear cutting and after flange forming. Samples were mechanically ground and polished to a 1 μm finish, then etched with Nital etching solutions. SEM and EBSD analyses were performed on a Zeiss Sigma field-emission gun SEM (Carl Zeiss Microscopy, Oberkochen, Germany) equipped with an Oxford Instruments EBSD detector (Abingdon, UK). EBSD measurements were collected at 18 kV acceleration voltage, 15 to 17 mm working distance. A step size of 0.3 μm was used to resolve intragranular orientation gradients while maintaining an adequate mapped area. EBSD data were reconstructed and analyzed in the MATLAB-based MTEX toolbox [49,77]. Trends in dislocation density were inferred from KAM, with intragranular misorientations ($< 5°$) used as an indicator of GND accumulation. The microstructural characterization was performed on representative cross-sections from one cold-formed component and one selected laser-assisted component. Each EBSD scan covered an area of $[300 \times 150]$ μm$^2$, capturing approximately 7500 grains per condition. The EBSD and SEM analyses were intended to characterize the local deformation and damage states associated with these contrasting forming conditions rather than to establish specimen-to-specimen statistical repeatability. Consequently, the statistical distributions derived from the EBSD maps (GND density histograms, grain aspect ratio distributions) describe spatial variation within the characterized region and are not interpreted as confidence intervals across independently formed specimens.

## 3.3. Simulation methods

FE simulations of shear cutting, localized laser heating, and flange forming were carried out in Abaqus/Explicit. The D-TMM constitutive model was implemented as a user-defined VUMAT subroutine [49] and the constitutive parameters used are reported in Table C.2-Table C.5. The principal numerical settings are summarized in Table 2.

As reported in [31], the mass scaling factors of $1 \times 10^5$ for cutting and $1 \times 10^6$ for flanging were chosen. After the initial engagement transient, KE/IE falls below 5% before the damage-relevant stage and stays around 1% and 2% during damage evolution, supporting a predominantly quasi-static response during the relevant interval. The local element size of 31.25 μm in the cut and flange-edge zones follows discretization adopted in the previously validated shear-cutting and flange-forming simulations [31] and is sufficient to resolve the strain gradient through the shear-affected zone. The friction coefficient $\mu = 0.3$ at all tool-sheet interfaces follows the calibration in [31] for dry contact

**Table 2**
Overview of the simulation setup and parameters used in the process simulations of the laser-assisted flange forming process.

| Process Stage | Model Type | Mesh Size | Velocity / Time | Mass Scaling | Material Model | Special Conditions |
|---|---|---|---|---|---|---|
| Shear cutting | 2D axisymmetric | 31.25 μm (cut zone) | Punch velocity: 22 mm/s | $1 \times 10^5$ | D-TMM (VUMAT) | Friction μ = 0.3; symmetry BC; rigid tooling |
| Laser heating | 3D symmetric | 31.25 μm (near hole) | Dwell time: as per setup | — | Thermal (JMatPro props.) | Experimentally characterized ring-shaped heat-flux profile; 2-step (heating + diffusion) |
| Flange forming | 3D symmetric | 31.25 μm (near hole) | Punch velocity: 20 mm/s | $1 \times 10^6$ | D-TMM (VUMAT) | Imported temperature field; friction μ = 0.3; rigid tooling |

between the investigated steel and tool steel. The laser heat-flux distribution used in the thermal simulation was derived from the experimentally characterized ring-beam profile of the integrated heating module [46,75]. Optical characterization at the nominal working distance of 170 mm provided the radial intensity distribution, ring dimensions, and circumferential uniformity of the beam. The corresponding spatial profile was mapped onto the FE surface and scaled according to the investigated laser power. An absorptivity of 0.65 for rolled S700MC in the laser wavelength range of 940–1064 nm was applied according to the preceding optical characterization. Heat loss from the free surfaces was represented through radiation and natural convection using an emissivity of 0.8 and convection coefficient of 20W $m^{-2} K^{-1}$ [78], while the tool-contact boundaries were maintained at 25 °C. During the thermal simulation, the microstructural state inherited from shear cutting was retained unchanged. Only the temperature field was evolved during laser heating and the subsequent diffusion period. The post-diffusion temperature field immediately before punch engagement was then combined with the inherited cutting-induced MSVs to initialize the flange-forming simulation. Microstructural evolution associated solely with the transient heating step was not explicitly resolved. For comparison with the measured surface-temperature histories, the numerical response was evaluated within a 1.25 mm-wide annular band centred at the maximum applied heat flux, located 3.35 mm radially outward from the cut edge. Five concentric nodal paths at $r_e = 2.725$, 3.0375, 3.350, 3.6625, and 3.975 mm were evaluated circumferentially. The mean nodal temperature defines the representative simulated response, while the $P_{10}$–$P_{90}$ range characterizes its spatial variation. Since the exact pyrometer footprint and radial position are unavailable, the comparison represents the simulated peak-heating region rather than a pointwise pyrometer location.

### 3.4. ICME positioning and framework requirements

The constitutive and process models described in Sections 2 and 3 originate from a series of previous developments that can be positioned within the conventional material–process–structure–performance architecture of ICME, as summarized in Fig. 5.

At the material (**M**) level, the D-TMM formulation relates macroscopic constitutive response to the MSV set $\{\rho_{cm}, \rho_{ci}, \rho_{wi}, f\}$ and was validated against forming limit curves (FLC, see Fig. 5) under complex loading [31]. At the process (**P**) level, the model was applied to simulate shear cutting and flange forming as separate operations [31,49], while the localized laser-heating stage required for the present manufacturing route had not been integrated into a continuous process-chain simulation. At the structure (**S**) level, the simulated MSV fields were correlated with EBSD and SEM observations to establish a link between process history and local microstructural response (see [31] for detailed results & discussions). At the property (**P**) level, component performance was evaluated through geometry-based metrics such as edge quality and flange height (Fig. 5).

Despite these individual developments, the resulting ICME description remained fragmented. The microstructural state generated during shear cutting was not propagated into the subsequent thermal and forming stages, and the influence of localized heating on the inherited edge state could therefore not be evaluated within a continuous simulation chain. Furthermore, conventional component-level assessment based on quantities such as flange geometry, local thickness, and forming force provides important macroscopic information but does not directly resolve the heterogeneous microstructural and damage state governing edge integrity. For the present problem, a process-quality description therefore requires these engineering quantities to be complemented by microstructure-informed indicators that retain the history of the SAZ.

These limitations define two methodological requirements for the present framework: first, a deterministic procedure is required to transfer the cutting-induced state variables and thermal field between simulations of different dimensionality and discretization; second, a spatial evaluation procedure is required to reduce the heterogeneous three-dimensional flange-edge fields into quantities that can be compared circumferentially and related to local edge integrity. The development of these two methods is presented in Section 4, followed by their application to the complete shear-cutting–localized-heating–-flange-forming process chain in Section 5.

## 4. ICME framework development

The framework requirements identified in Section 3.4 are addressed through two methodological developments. Section 4.1 introduces a deterministic variable-transfer procedure that propagates the cutting-induced geometry and D-TMM state across sequential simulations. Section 4.2 introduces a circumferential binning procedure that converts three-dimensional flange-edge fields into angularly resolved distributions for comparison between process conditions. Together, these methods provide the connection required to transform the previously separate process models into a continuous ICME process chain.

### 4.1. Deterministic variable-transfer procedure

The complete laser-assisted flange forming process is simulated as a four-stage chain: 2D axisymmetric shear cutting, 2D-to-3D reconstruction of the deformed blank, 3D localized laser heating, and 3D flange forming. Fig. 6 summarizes the data flow between these stages.

The transferred process state comprises the deformed geometry, the four MSVs $\rho_{cm}, \rho_{ci}, \rho_{wi}, f$, and the temperature field $T$ where applicable. The deterministic transfer follows four steps. First, integration-point values of the source-stage MSVs are averaged onto element nodes by inverse-distance-weighted interpolation to obtain continuous nodal fields. Second, the source mesh topology is preserved and re-used wherever possible, avoiding additional remeshing and associated smoothing of the strong gradients within the SAZ. Third, during the 2D-to-3D reconstruction, the source geometry and fields are swept about the symmetry axis at $N$ angular increments and mapped to the corresponding destination integration points. Circumferential isotropy is therefore assumed for the reconstructed cutting state; its implications are discussed in Section 7.1 with reference to experimentally observed cut-edge heterogeneity [21]. Fourth, the transferred D-TMM state variables $\rho_{cm}, \rho_{ci}, \rho_{wi}$, and $f$ are stored as SDV1–SDV4, respectively. Their initial parameterization and experimental assessment against EBSD- and SEM-derived microstructural information are described in [31,49].

Equivalent plastic strain is deliberately not transferred as an

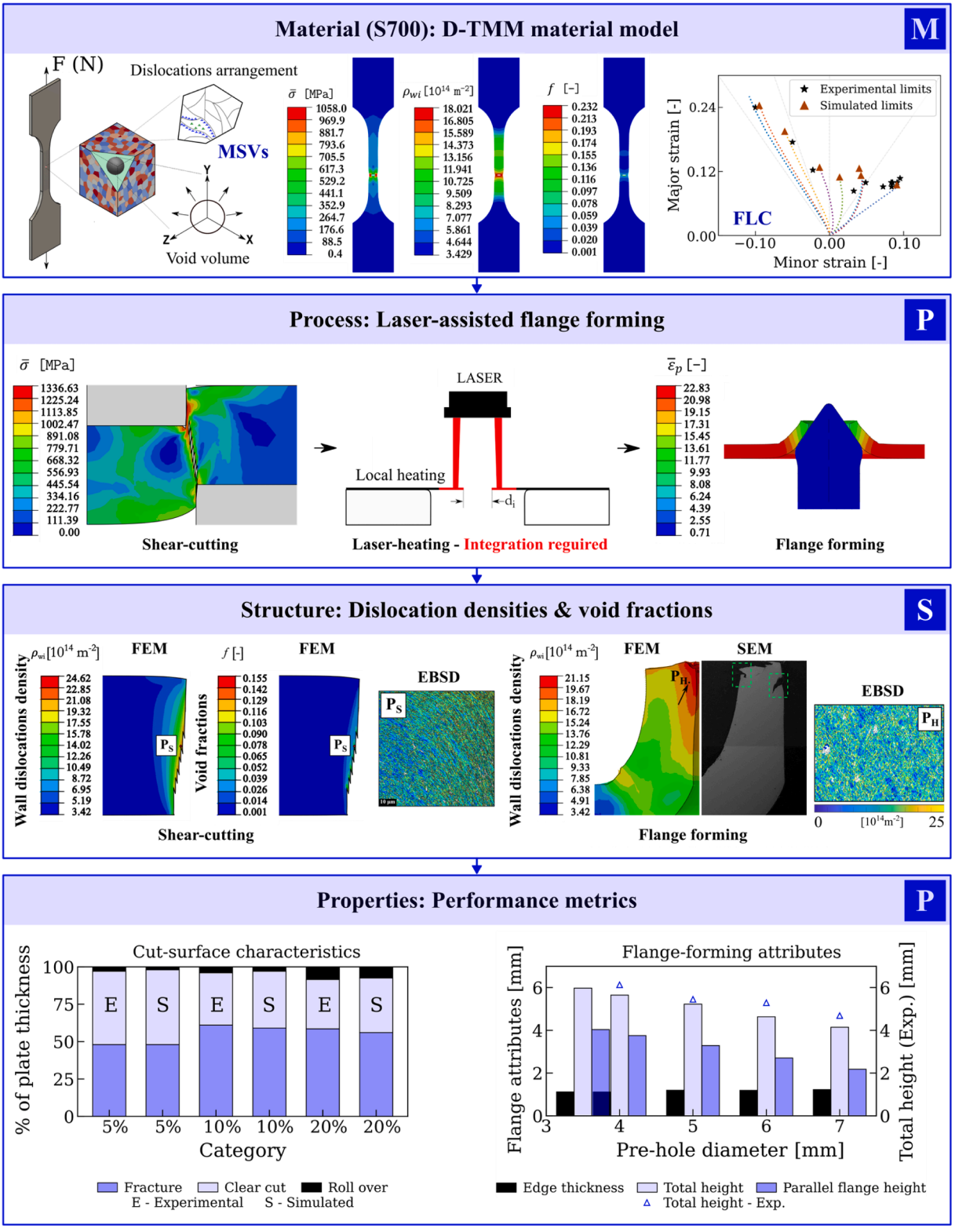



**Fig. 5.** ICME framework linking the D-TMM constitutive model (M), process-chain simulations (P), microstructural characterization (S) and component assessment (P) for laser-assisted flange forming of S700MC [31,49].

additional state variable within the D-TMM process chain, since it is a path-dependent scalar and does not uniquely describe the underlying dislocation substructure. The dislocation-density variables already carry the deformation state used by the D-TMM constitutive formulation. A conventional process-chain configuration transferring equivalent plastic strain and void fraction together with the shear-cut geometry is considered separately in Section 6.5 and discussed in Section 7.2. The thermal field is treated separately. The laser-heating simulation produces a transient temperature field $T(\mathbf{x}, t)$, over the heating duration and the subsequent diffusion period, but only the post-diffusion field $T(\mathbf{x}, t_f)$ immediately before punch engagement is transferred as the initial thermal condition for flange forming. The cutting-induced MSVs are

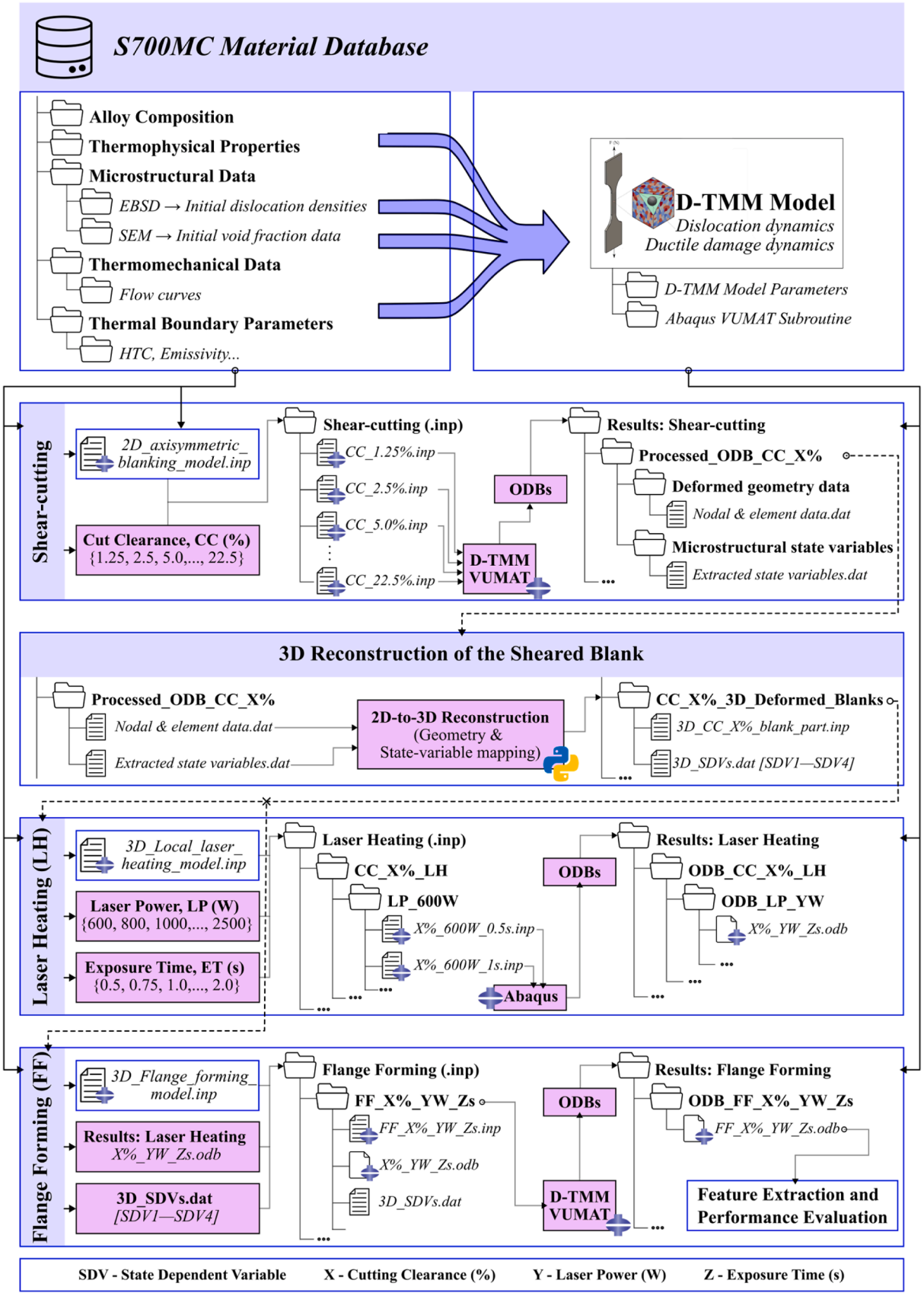



**Fig. 6.** Deterministic variable-transfer procedure: sequential simulation workflow and transfer of geometry, microstructural state variables and temperature between process steps.

retained during the heating and diffusion stages. At the start of flange forming, the temperature-dependent constitutive coefficients of the D-TMM formulation are evaluated using the transferred local temperature field. Microstructural evolution during the preceding thermal transient is not explicitly resolved; the implications of this assumption and the applicable temperature range are discussed in Section 7.5.

The performance evaluation and feature extraction steps indicated in the ICME workflow (Fig. 6) require a method for reducing the spatially heterogeneous three-dimensional fields generated by the process chain to quantitative circumferential distributions using the statistical binning method, which is introduced in Section 4.2.

### 4.2. Circumferential statistical binning method

The ICME simulations generate spatially heterogeneous three-dimensional distributions of geometry, temperature, and MSVs. To enable systematic comparison between process conditions, these fields are reduced to angularly resolved statistical distributions using the circumferential binning procedure summarized in Fig. 7. The evaluation begins with the fully deformed flange geometry (Fig. 7a). Owing to circumferential symmetry, a quarter-section is extracted, and a region of interest is defined within a 2 mm flange-edge zone (Fig. 7 (b–e)), where deformation and damage are concentrated. The selected volume contains the spatially resolved state variables $\{\rho_{cm}, \rho_{ci}, \rho_{wi}, f\}$ together with the mechanical and thermal fields evaluated in the subsequent analyses.

To quantify circumferential variation, the selected volume is subdivided into $N$ equal angular bins measured from the reference X-axis (Fig. 7f). The bin count corresponds directly to the circumferential discretization of the FE mesh generated during the 2D-to-3D reconstruction (Section 4.1), so that each bin represents one angular mesh segment. The sensitivity to this discretization is evaluated in Section 6.1. Using $\phi$ as the circumferential coordinate, the angular width of each bin is

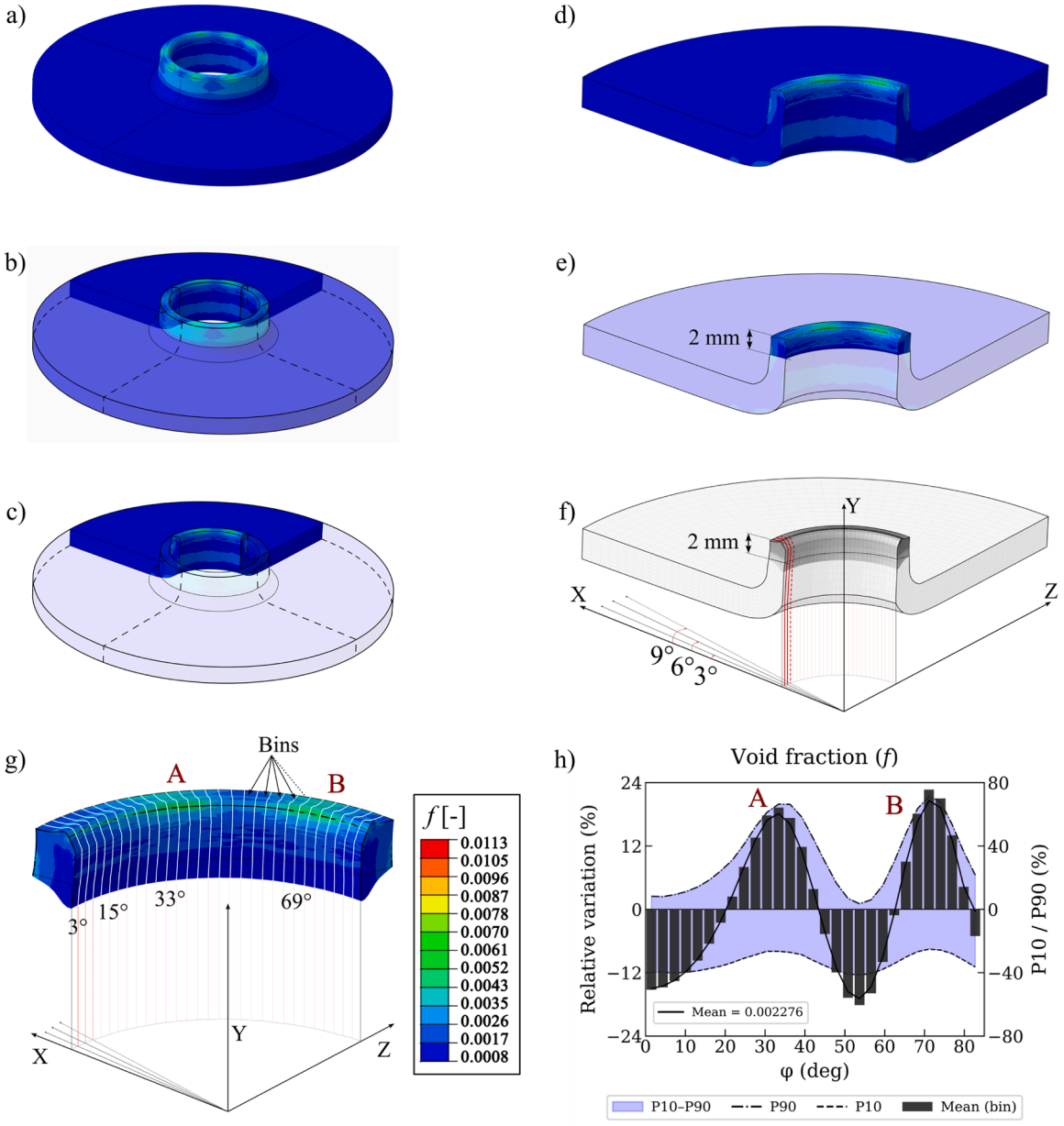



**Fig. 7.** Circumferential spatial quantification framework for the ICME-predicted MSVs: (a) 3D flange formed component; (b-d) Selection of the representative quarter geometry for post-processing; (e) Definition of the critical analysis region; (f) Circumferential coordinate system for angular segmentation; (g) Angular discretization of the spatial distribution of void fraction ***f***, sectors A and B indicate localized regions; (h) Conversion of the 3D results into circumferential statistical distributions showing arithmetic bin-averaged values and the $P_{10}$–$P_{90}$ variability envelope.

therefore defined as

$$\Delta\phi = \frac{\phi_{\max} - \phi_{\min}}{N}, \tag{9}$$

where $\phi_{\max} - \phi_{\min} = 90^{\circ}$ for the quarter section. This corresponds to an angular resolution of approximately $\Delta\phi$ per segment. Each bin thus represents a discrete circumferential location along the flange edge. For each angular segment $i$, the field variables were spatially averaged over the corresponding bin volume $\mathscr{V}_i$. The active nodal set contained within this region is defined as

$$\mathscr{N}_i = \{ j \mid \boldsymbol{x}_j \in \mathscr{V}_i, j \text{ belongs to the active material} \} \tag{10}$$

where $\boldsymbol{x}_j$ denotes the spatial position of node $j$ in the deformed configuration. In practice, the field variables were averaged directly from the nodal values contained within each segment,

$$\overline{\psi}_i = \frac{1}{n_i} \sum_{j \in \mathscr{N}_i} \psi_j, \tag{11}$$

where $\psi_j$ denotes the nodal value of the evaluated field and $n_i = |\mathscr{N}_i|$ is the number of active nodes contained in bin $i$. Since elements may be deleted after reaching the terminal failure condition, the number of contributing active nodes can vary between angular segments and simulation conditions. The resulting mean therefore represents the state of the material remaining active within the corresponding spatial bin at the evaluated frame. Fig. 7g shows the segmented representation of the flange region after angular discretization. Two representative sectors, labeled *A* and *B*, are highlighted as examples of circumferential regions where the evaluated variable exhibits comparatively higher values. To facilitate the interpretation of the results, the bin-averaged results are further represented in two-dimensional statistical form (Fig. 7h). In this representation, the horizontal axis denotes the circumferential position in terms of the quadrant angle from the reference axis, while the vertical axis represents the evaluated field or its relative variation. In addition to the bin mean, the $P_{10}$ and $P_{90}$ percentiles of the active nodal values are reported to characterize through-thickness and radial variability within each angular segment. The $P_{10}$ and $P_{90}$ envelope therefore describes the local spatial spread around the circumferential mean and allows localized sectors of elevated or reduced response to be identified.

This procedure provides a consistent basis for comparing the spatial heterogeneity of flange-edge states resulting from different cutting conditions, thermal histories, and inherited microstructural states and is applied throughout Section 6.

## 5. Implementation of the ICME process chain

The ICME framework introduced in Section 4 was applied to the investigated manufacturing sequence by sequentially coupling shear cutting, localized laser heating, and flange forming. The process state propagated through the chain comprises the deformed geometry, the D-TMM microstructural state variables $\{\rho_{cm}, \rho_{ci}, \rho_{wi}, f\}$, and the temperature field $T$ where applicable. The deterministic transfer procedure and circumferential quantification methodology are defined in Sections 4.1 and 4.2, respectively; the present section describes their implementation for the investigated process conditions.

### 5.1. Reconstruction of the shear-cut blank

The process chain was initiated from the final states obtained from the previously validated shear-cutting simulations [31]. For each investigated cutting condition, the deformed cut-edge geometry and the corresponding distributions of $\rho_{cm}$, $\rho_{ci}$, $\rho_{wi}$, and $f$ were transferred to the reconstructed three-dimensional blank according to Section 4.1.

The deformed two-dimensional cutting configurations were revolved about the symmetry axis to generate the corresponding three-dimensional blanks while retaining the original mesh topology in the shear-affected region (Fig. 8). Fig. 9 presents the transferred D-TMM state variables. The resulting configurations therefore preserve the cutting-induced geometrical and microstructural gradients entering the subsequent process stages. Because the source cutting simulations are axisymmetric, the reconstructed geometry and material state are circumferentially uniform at this stage. They consequently represent idealized cutting conditions with constant clearance and without circumferential variations arising from tool wear, eccentricity, or misalignment. Any angular heterogeneity developing during subsequent flange forming therefore originates from the three-dimensional forming response rather than from a prescribed circumferential variation in the reconstructed cutting state.

### 5.2. Localized heating and thermal-state transfer

The reconstructed shear-cut blanks were subsequently subjected to the localized ring-heating conditions defined in Section 3.3. The thermal simulation was performed directly on the reconstructed three-dimensional geometry, preserving the spatial relationship between the laser-heated region and the inherited shear-cut edge. Fig. 10(a–d) shows the applied ring-shaped heat input and the resulting thermal field during the heating and diffusion stages.

For each thermal condition, the temperature field after the prescribed heating and diffusion period and immediately before punch engagement was transferred as the initial thermal state for flange forming. The cutting-induced MSVs were retained during this stage, so that the state entering flange forming combines the inherited geometry and microstructural condition with the spatially varying post-diffusion temperature field. Microstructural evolution during the isolated heating and diffusion stage is not explicitly resolved, as defined in Section 4.1. The resulting post-diffusion temperature fields provide the thermal conditions used to investigate the influence of localized heating on the subsequent flange-edge response, which is discussed further in Section 6.7.

### 5.3. Initialization and post-processing of the flange-forming simulations

The flange-forming simulations were initialized using the reconstructed shear-cut geometry together with the inherited D-TMM state $\{\rho_{cm}, \rho_{ci}, \rho_{wi}, f\}$, and the case-specific post-diffusion temperature field for the laser-assisted conditions. Fig. 11 shows the three-dimensional forming assembly and the state of the critical cut-edge region immediately before punch displacement. Equivalent plastic strain is not introduced as an additional transferred D-TMM state variable and evolves during flange forming according to the constitutive response defined in Section 2.

Following flange forming, the nodal and element-based output fields were exported from Abaqus and reconstructed in Python using the initial and deformed coordinates. The evaluated quantities comprise the three dislocation-density populations, equivalent plastic strain, void fraction, and temperature. Fig. 12 shows the resulting spatial representation for the complete quarter model together with the flange-edge region retained for subsequent analysis. These fields were subsequently processed using the circumferential statistical binning method of Section 4.2 to obtain angularly resolved distributions for the comparison of flange-edge states resulting from different cutting conditions, thermal histories, and inherited microstructural states.

### 5.4. Controlled simulation configurations

In addition to the complete process-chain simulations, controlled flange-forming calculations were performed to separate the effects of inherited cutting condition, constitutive description, shear-sensitive damage, MSV inheritance, thermal condition, and blank orientation. The investigated configurations are summarized in Table 3. The cutting-

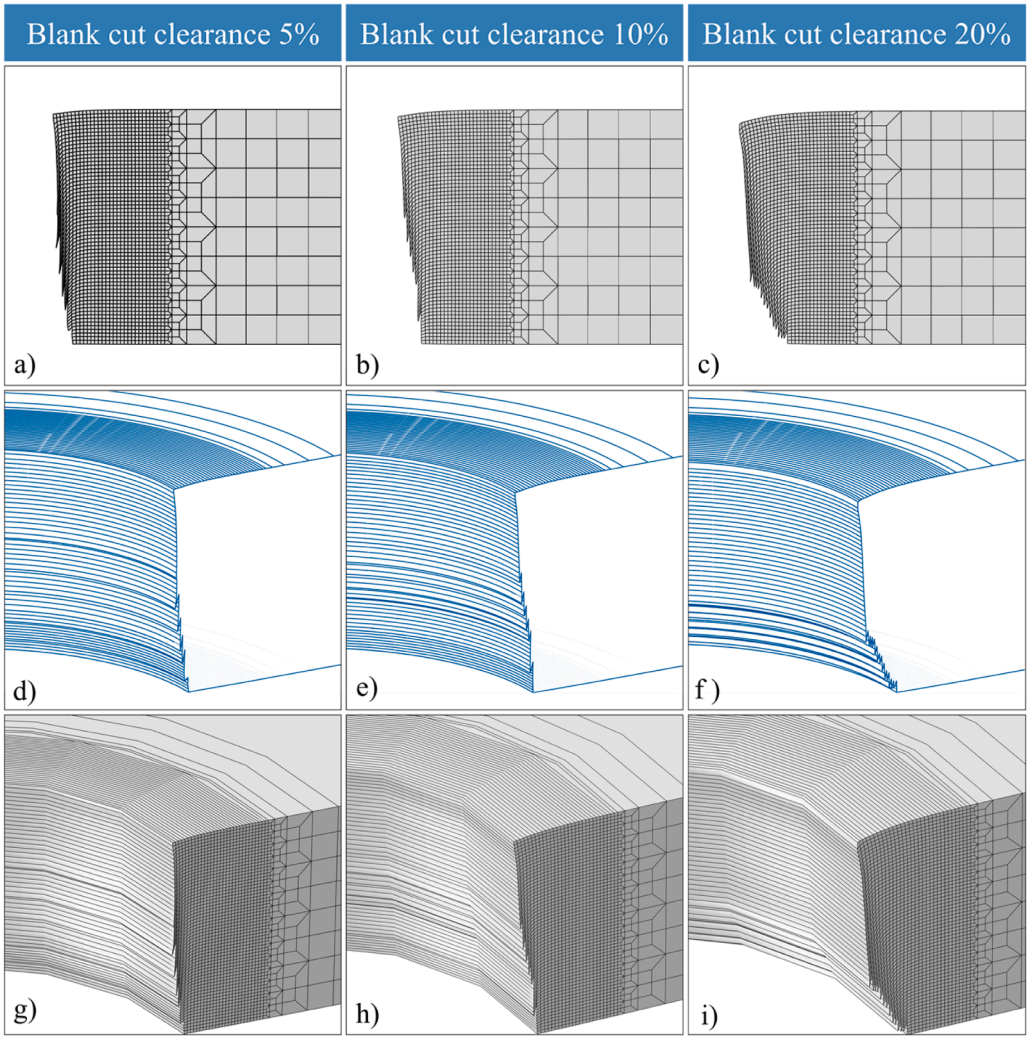



**Fig. 8.** Reconstruction of three-dimensional shear-cut blanks for 5%, 10% and 20% cut clearances: (a–c) deformed two-dimensional meshes; (d–f) revolved geometries; and (g–i) reconstructed 3D edge meshes.

state series compares the ideal reference edge with reconstructed shear-cut geometries and the corresponding cases including transferred MSVs, thereby separating geometrical cutting effects from inherited microstructural-state effects. The constitutive-control series uses a common shear-cut geometry to compare the conventional transferred-state formulation with successive D-TMM variants, isolating the roles of the shear-sensitive damage contribution and MSV inheritance. Finally, the thermal/process series retains the reconstructed cutting state while varying the post-diffusion thermal field and, for the inverted configuration, the orientation of the inherited cut edge. These controlled cases provide the basis for the comparisons presented in Sections 6.3, 6.5, and 6.7.

## 6. Results

The results are presented in terms of the spatially resolved and circumferentially quantified material states (Section 4.2) obtained from the coupled process-chain simulations (Section 5). The numerical robustness of the circumferential analysis is first established with respect to angular discretization, evaluation-region height, and model symmetry. The subsequent sections evaluate the circumferential state generated during flange forming, compare the ICME formulation with conventional state-transfer approaches, examine the development of fracture under cold forming, assess the influence of localized heating and blank orientation, and compare the predicted material states with experimental observations.

### 6.1. Numerical robustness of circumferential analysis

The sensitivity of the circumferential quantification procedure (from Section 4.2) was evaluated on the baseline configuration B4D, which uses the D-TMM constitutive model with an ideal punched hole and no inherited cutting history, as defined in Table 3. The assessed parameters include the angular discretization $\Delta\phi$, the height $\Delta h$ of the analyzed flange-edge region, and the imposed model symmetry. The angular discretization is not an independent post-processing parameter: each circumferential bin corresponds to one angular segment of the 3D mesh generated during the 2D-to-3D reconstruction (Section 4.1). Increasing the bin count from 15 to 30 to 60 therefore doubles the number of circumferential elements at each step, directly affecting the spatial resolution of the FE solution itself. Fig. 13 compares the void-fraction distributions obtained using 15, 30, and 60 circumferential bins, corresponding to angular resolutions of 6°, 3°, and 1.5°. All three discretizations reveal two regions of elevated void fraction at approximately $\phi = 35°$ and 70°. Increasing the number of bins primarily sharpens the local variation, while the 30- and 60-bin distributions show close agreement in both the location and shape of these regions, indicating that the 30-bin discretization is sufficient to resolve the characteristic angular pattern for the present analysis. Variation of the evaluated flange-edge height changes the amplitude and spatial

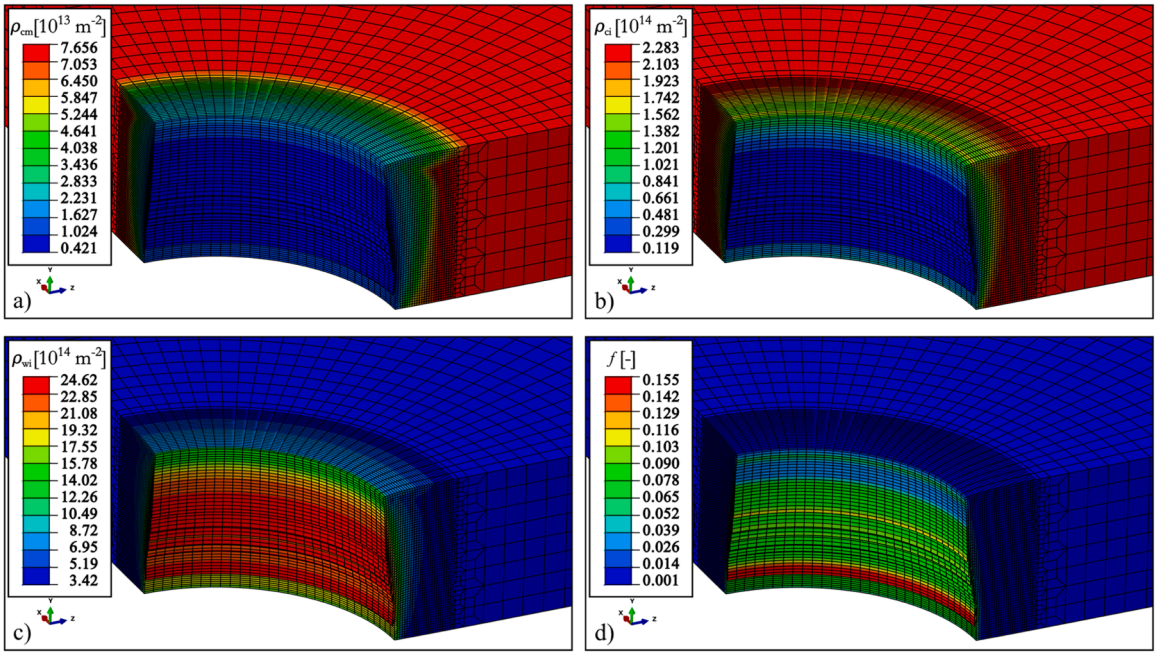



**Fig. 9.** Transfer of cutting-induced state variables (from 10% cut clearance) to the reconstructed three-dimensional blank: (a) Cell mobile dislocation density $\rho_{cm}$; (b) Cell immobile dislocation density $\rho_{ci}$; (c) Wall immobile dislocation density $\rho_{wi}$; (d) Void volume fraction $f$.

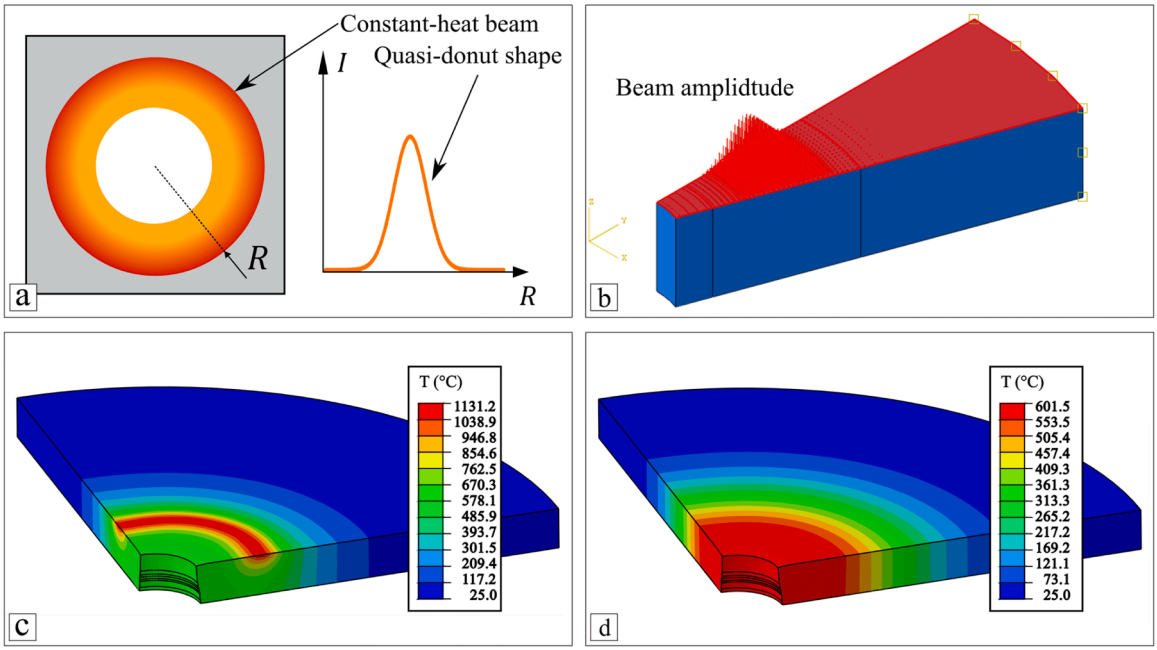



**Fig. 10.** Localized laser heating simulations: (a) annular beam profile; (b) applied amplitude distribution; (c) temperature after heating; and (d) post-diffusion temperature transferred to flange forming.

averaging of the void-fraction response but retains the two characteristic angular regions. Likewise, replacing the quarter model with a half model preserves the principal localization positions, indicating that they are not generated solely by the quarter-model symmetry boundaries.

### 6.2. Thermal parameter study

The thermal parameter study was centred on the experimentally applied reference condition (Section 3.2.2) of 2000 W laser power and 1 s exposure time [46,75]. Fig. 14 compares the predicted post-diffusion temperature fields for variations in laser power (1000 to 2000 W), exposure time (1 to 2 s), and beam size parameter (4 to 5 mm). The comparison is evaluated immediately before punch engagement, as this temperature field defines the thermal state transferred to flange forming (Section 4.1).

Increasing laser power raises the overall temperature level, while longer exposure extends thermal penetration and broadens the heated region. The beam size parameter primarily controls the radial temperature gradient: a smaller beam concentrates the heat input and produces a steeper temperature decrease toward the forming zone, whereas a larger beam distributes the thermal input more gradually. The selected condition produces a forming-zone temperature of approximately

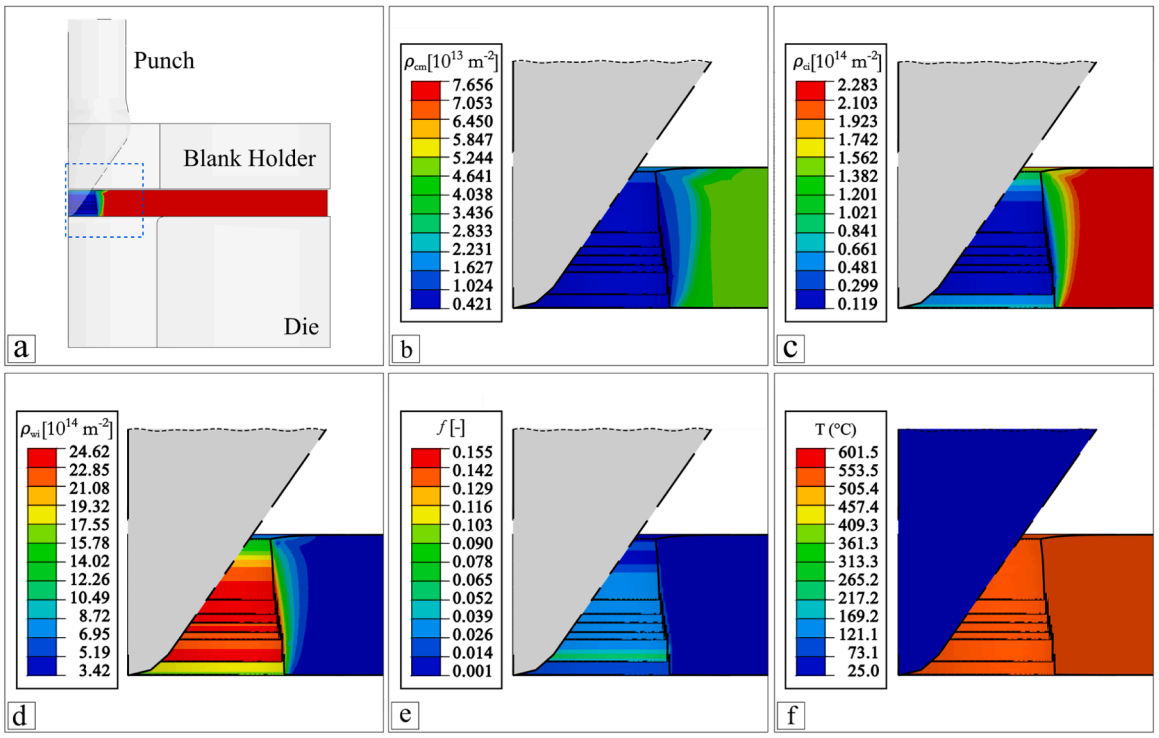



**Fig. 11.** Flange-forming initialization: (a) finite element setup of the flange forming assembly; (b–f) zoomed-in view of the shear-cut edge region showing transferred microstructural and thermal fields: (b) cell mobile dislocation density $\boldsymbol{\rho_{cm}}$; (c) cell immobile dislocation density $\boldsymbol{\rho_{ci}}$; (d) wall immobile dislocation density $\boldsymbol{\rho_{wi}}$; (e) void fraction distribution $\boldsymbol{f}$; and (f) post-diffusion temperature field before flange forming $\boldsymbol{T}$.

550–600 °C. This temperature is slightly above the approximately 500 °C calibration range of the D-TMM formulation [49] and therefore represents a limited constitutive extrapolation. It nevertheless remains below the reported $A_{c1}$ temperature of S700MC [79], and provides sufficient reduction in the flow stress and suppresses sharp hardening gradients inherited from shear cutting.

The parameter variations show that similar peak temperatures during irradiation can produce different post-diffusion thermal states depending on the spatial distribution of the heat input. Conditions producing steep gradients across the critical edge region were considered less suitable even when the peak temperature was high. The 2000 W, 1 s, 5 mm condition provides the most stable radial profile within the forming zone and is retained as the reference for the subsequent process-chain analyses in Sections 6.3 to 6.5. The influence of alternative thermal conditions and the inverted-blank configuration on flange-forming damage is evaluated in Section 6.7.

### 6.3. Circumferential flange-edge state and influence of the inherited cutting condition

Following the robustness assessment in Section 6.1, the circumferential distributions of the D-TMM state variables were evaluated using the 30-bin discretization and the 2 mm flange-edge region at 2000 W, 1 s, 5 mm laser condition. Fig. 15 shows the resulting distributions of $\rho_{cm}$, $\rho_{ci}$,$\rho_{wi}$, equivalent plastic strain $\bar{\varepsilon}_p$, void fraction $f$, and temperature $T$ for the baseline configuration B4D. The dislocation-density components exhibit distinct circumferential variations, while the equivalent plastic strain shows a comparatively smaller modulation. The void fraction displays the clearest localization, with two dominant regions of elevated damage around 35° and 70°. In contrast, the circumferential temperature variation remains small.

The same circumferential analysis was applied to the other configurations (from cutting-series) summarized in Table 3, spanning three cutting clearances (5%, 10%, 20%) with and without transfer of the corresponding D-TMM state variables. The absolute distributions in Fig. 16 indicate that the cutting condition primarily changes the overall level of the state variables entering and evolving during flange forming. Increasing the severity of the inherited edge state results in higher accumulated damage within the critical flange-edge region, while the principal angular positions identified in Section 6.1 remain evident across the investigated configurations.

The effect of MSV transfer is most pronounced in the void-fraction response. Compared with simulations using the reconstructed cut-edge geometry without the corresponding microstructural state, transfer of $\rho_{cm}$,$\rho_{ci}$,$\rho_{wi}$, and $f$ increases the magnitude of the localized damage while retaining the same dominant circumferential sectors. The mean-normalized distributions in Fig. 17 therefore distinguish the inherited level shift from the redistribution that develops during flange forming: the cutting state controls the magnitude of the downstream response, whereas the angular variation develops during the three-dimensional forming stage.

The $\rho_{cm}$,$\rho_{ci}$,$\rho_{wi}$ populations respond differently to the downstream deformation. Their absolute levels retain a clear dependence on the transferred cutting state, while their circumferential variations indicate redistribution of the dislocation substructure during flange forming. Equivalent plastic strain exhibits comparatively weak circumferential modulation, whereas the void-fraction response shows substantially stronger localization, confirming that plastic flow sets the circumferential envelope within which damage concentrates. These differences are considerably smaller in the temperature field, confirming that the angular variation of the mechanical and microstructural state is not associated with a corresponding circumferential variation of the imposed thermal condition.

Overall, the process-chain simulations show that the flange-edge response contains two superimposed contributions: an inherited level determined by the preceding shear-cut state and a circumferential redistribution generated during flange forming. The extent to which this response depends on the constitutive representation of the transferred

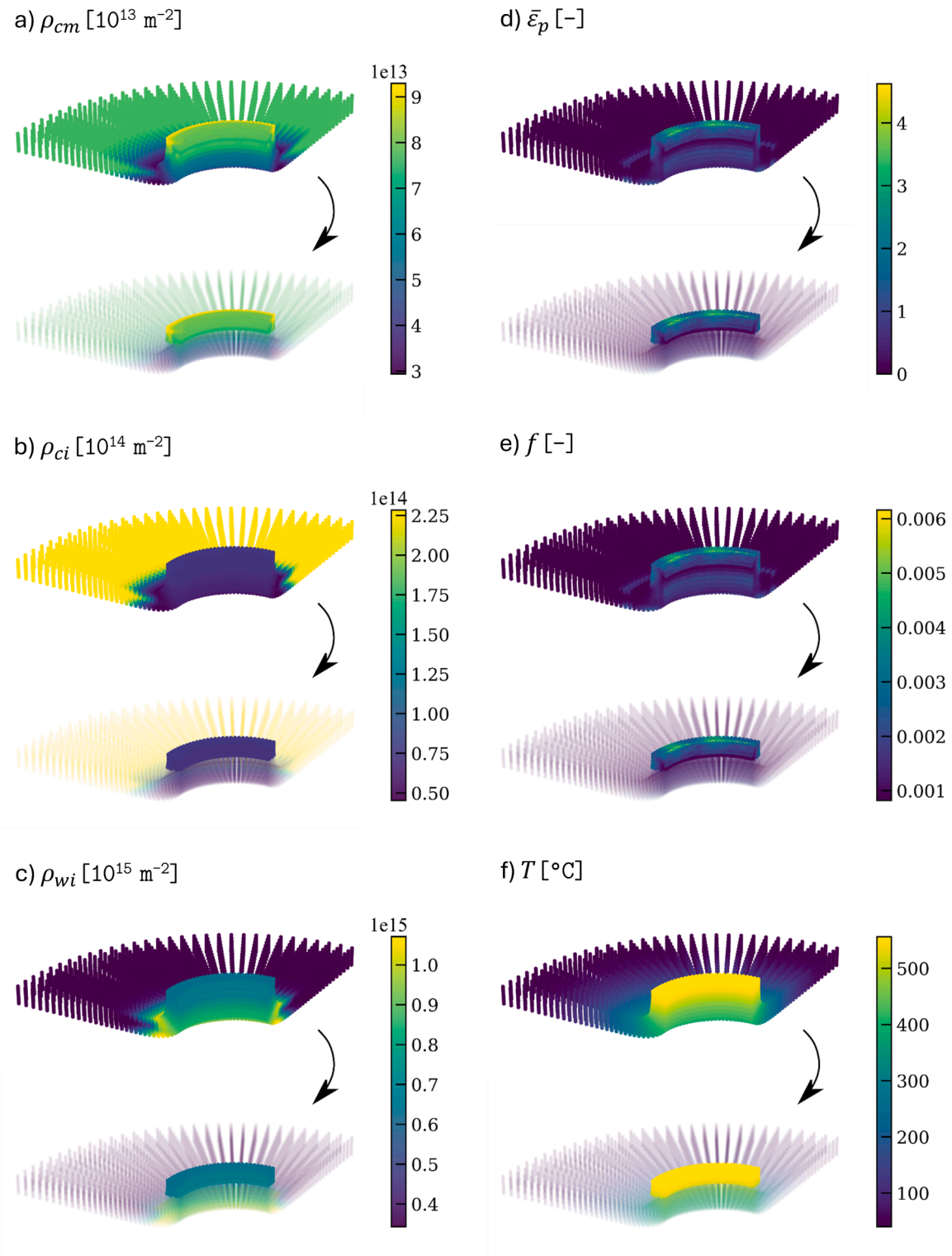



**Fig. 12.** Spatial distribution of ICME-predicted state variables in the flange edge region: (a) Cell mobile dislocation density $\rho_{cm}$; (b) Cell immobile dislocation density $\rho_{ci}$; (c) Wall immobile dislocation density $\rho_{wi}$; (d) Equivalent plastic strain $\bar{\varepsilon}_p$; (e) Void fraction $f$; (f) Temperature $T$. Upper images show the simulated quarter geometry; lower images highlight the extracted critical edge region used for further analysis.

state is examined in Section 6.5 using the conventional and D-TMM baseline calculations.

### 6.4. Numerical force response across inherited edge conditions

The force-time responses of the investigated warm-formed edge conditions (Section 6.3) are compared in Fig. 18. All configurations exhibit a similar overall loading sequence and comparable peak forming forces of approximately 26–27 kN, with a spread of about 1–2 kN across the cutting and MSV-transfer cases. Differences are most apparent during the loading ramp and near the peak, whereas the unloading response remains similar. Compared with the pronounced differences in the

**Table 3**
Controlled flange-forming configurations used to distinguish the effects of inherited cutting state, constitutive/state-transfer strategy, shear-sensitive damage contribution, thermal condition, and blank orientation.

| Simulation Group | Configuration | Material description | Initial / transferred state | Shear-sensitive damage | Primary comparison |
|---|---|---|---|---|---|
| Cutting-state series | B4D | D-TMM | Ideal/reference edge state without inherited cutting history | Active | Reference state |
| | B4D20C, B4D40C, B4D80C | D-TMM | Reconstructed shear-cut geometry only (Cut-clearance effect) | Active | Influence of cut-edge geometry/condition |
| | B4D20C + MSV, B4D40C + MSV, B4D80C + MSV | D-TMM | Reconstructed geometry + transferred $\rho_{cm}$, $\rho_{ci}$, $\rho_{wi}$, $f$ | Active | Influence of inherited MSV state |
| Constitutive-control series | Conventional transferred-state case | Tabulated plasticity + conventional GTN | Common shear-cut geometry + transferred $\bar{\varepsilon}_p$ and $f$ | Not applicable | Conventional scalar-history baseline |
| | D-TMM, No Shear | D-TMM | Common shear-cut geometry; no transferred MSVs | Not active | Effect of suppressing shear-sensitive damage |
| | D-TMM + Shear | D-TMM | Common shear-cut geometry; no transferred MSVs | Active | Effect associated with shear-sensitive formulation |
| | D-TMM + Shear + MSV | D-TMM | Common shear-cut geometry + transferred $\rho_{cm}$, $\rho_{ci}$, $\rho_{wi}$, $f$ | Active | Additional influence of inherited MSVs |
| Thermal/process series | C01–C04 | D-TMM | Reconstructed geometry + MSVs + case-specific post-diffusion temperature field | Active | Influence of laser condition |
| | C05 | D-TMM | Same thermal condition as selected reference case + MSVs + inverted blank orientation | Active | Influence of blank orientation |

circumferential void-fraction and dislocation-density fields reported in Section 6.3, the global numerical force response is relatively insensitive to the inherited edge condition (see Section 7.4).

### 6.5. Conventional baseline and constitutive-control comparison

To assess the influence of the constitutive representation on the predicted flange-edge damage, the conventional transferred-state formulation was compared with the D-TMM control calculations (Table 3 - Constitutive-control series). The conventional model combines tabulated plasticity (experimental flow curves from [49]) and the conventional GTN formulation with transferred shear-cut geometry, equivalent plastic strain (PEEQ), and void fraction (VVF). The D-TMM calculations use microstructure-based constitutive formulation and additionally allow the effects of the shear-sensitive damage contribution and transferred MSVs to be examined through internal control cases. The conventional-to-D-TMM comparison therefore represents a comparison of complete constitutive/state-transfer strategies, whereas the D-TMM controls are used to isolate individual model contributions.

Fig. 19 compares the resulting flange-edge damage response for the representative control configurations. The spatial fields (Fig. 19(a–c)) show the final fracture states, while the circumferential comparison of equivalent plastic strain (Fig. 19(d)), void fraction (Fig. 19(e)), and stress triaxiality (Fig. 19(f)) is evaluated at a punch displacement of 5 mm, corresponding to the onset of fracture in the complete D-TMM case. This provides a common pre-deletion state for comparison across all formulations. The conventional transferred-state formulation produces a comparatively uniform void-fraction distribution along the flange edge. The D-TMM formulation without the shear-sensitive contribution similarly shows only weak circumferential variation, whereas activation of the shear-sensitive contribution produces two localized regions of elevated void fraction near $\phi \approx 35^\circ$ and $70^\circ$. Transfer of the cutting-induced MSVs further increases the magnitude of the localized damage while retaining the same principal angular positions.

The corresponding equivalent-plastic-strain and stress-triaxiality distributions (Fig. 19(d-f)) provide additional context for this response. The conventional transferred-state baseline exhibits the highest circumferential mean equivalent plastic strain, while the complete D-TMM case develops the strongest localized void-fraction response despite a lower mean strain level. The localized damage pattern therefore cannot be explained solely by the magnitude of accumulated equivalent plastic strain. Similarly, the circumferential mean stress triaxiality remains moderately positive for both formulations. However, the $P_{10}$ and $P_{90}$ envelope of the complete D-TMM case spans a wider range of local stress states, with the lower tail approaching low-triaxiality conditions within the critical sectors.

Overall, the conventional transferred-state baseline does not reproduce the localized response obtained with the complete D-TMM framework under the investigated conditions. Because the two formulations differ in both constitutive description and state representation, this comparison is interpreted as a comparison of complete modelling strategies rather than as an isolated test of PEEQ/VVF versus MSV transfer. Within the D-TMM control series (Table 3), the shear-sensitive damage contribution is associated with the emergence of circumferential localization, while the transferred MSVs increase the severity of the response without substantially altering the principal angular positions.

### 6.6. Edge fracture under cold forming conditions

The evolution of the localized damage response was examined further for the cold-forming condition. Fig. 20 compares the simulated void-fraction field at an intermediate stage of flange forming, the final numerical fracture state after completion of the process, and the experimentally fractured component for the same process conditions.

At the intermediate stage, elevated void fraction is already concentrated within discrete circumferential regions of the flange edge. With continued punch displacement, these localized regions develop into separated zones of element deletion, resulting in a discontinuous fracture pattern around the flange circumference rather than uniform edge failure. The final simulation therefore preserves the spatially localized character of the damage observed at the earlier stage.

The representative cold-formed component exhibits multiple discrete edge cracks rather than continuous fracture around the complete circumference. The numerical result similarly develops spatially separated regions of element deletion. The comparison is therefore restricted to qualitative agreement in the localized fracture morphology. The available experimental dataset does not permit validation of the number, angular position, or initiation sequence of individual cracks. The simulation consequently demonstrates localized numerical fracture under a forming condition that experimentally produces discrete edge cracking, while pointwise prediction of individual crack-initiation sites

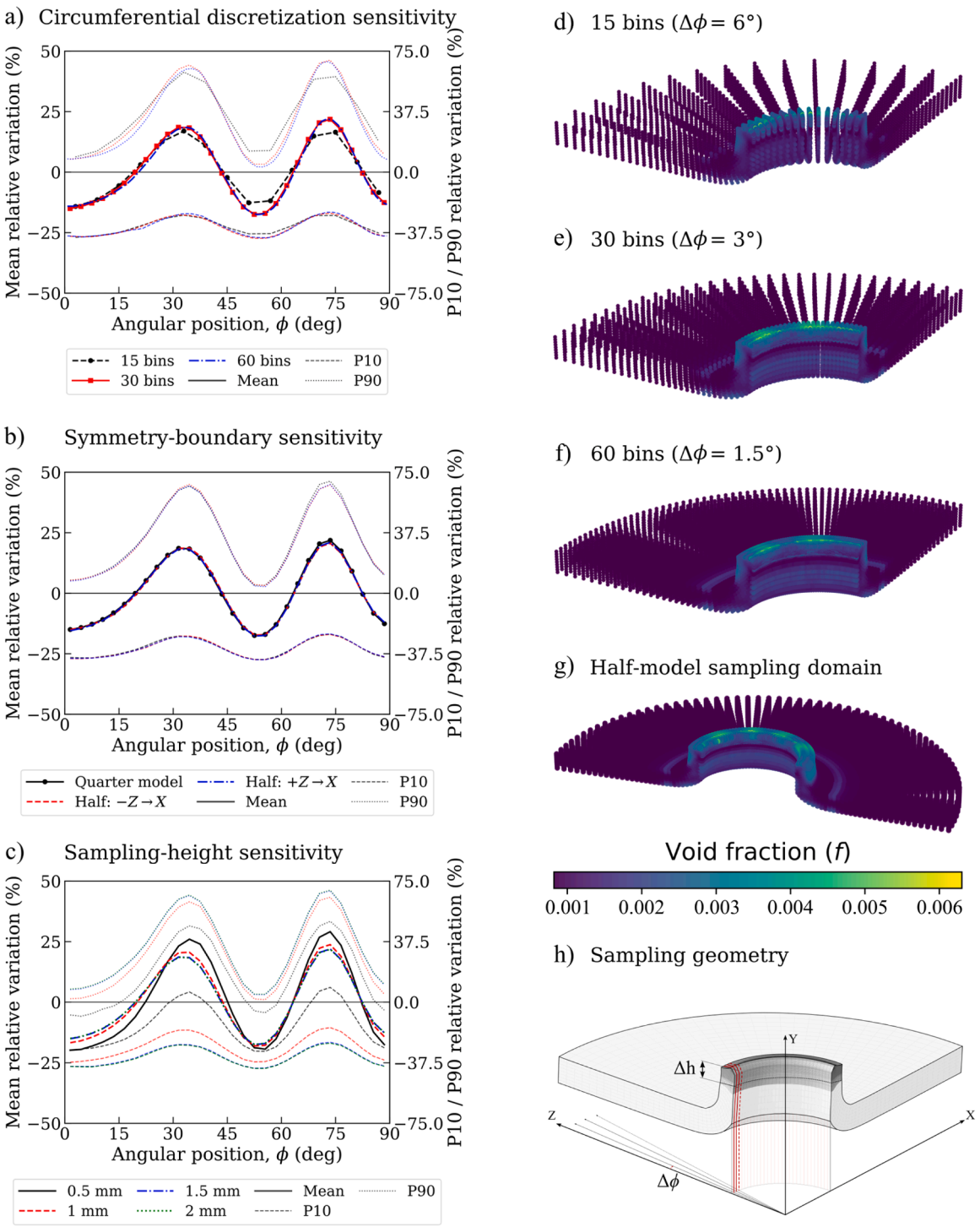



**Fig. 13.** Numerical robustness of circumferential void-fraction localization: sensitivity to (a) angular discretization Δϕ, (b) model symmetry and (c) sampling height Δ*h*; fields for (d–f) 15, 30 and 60 bins and (g) the half model; and (h) sampling geometry defining the angular increment ΔΦ and height interval Δh. The void-fraction colour scale applies to (d–g).

remains outside the available validation scope.

### *6.7. Influence of thermal condition and blank orientation on flange-forming damage*

The thermal study in Section 6.2 identified the 2000 W, 1 s, 5 mm condition as the experimental reference state. To assess the influence of the thermal condition and blank orientation on subsequent flange forming, five configurations (C01–C05) were propagated through the complete process chain. C01–C04 vary laser power and beam-size parameter at a constant exposure time of 1 s, producing forming-zone temperatures from approximately 357 °C to 554 °C. C05 uses the same nominal laser parameters as C04, but with the blank orientation inverted such that the fracture-zone side of the shear-cut edge faces the inner flange surface. Fig. 21 compares the resulting temperature, wall-immobile dislocation density, and void-fraction fields, while Fig. 22 summarizes the corresponding edge-region metrics.

The predicted failure response shows a clear dependence on the

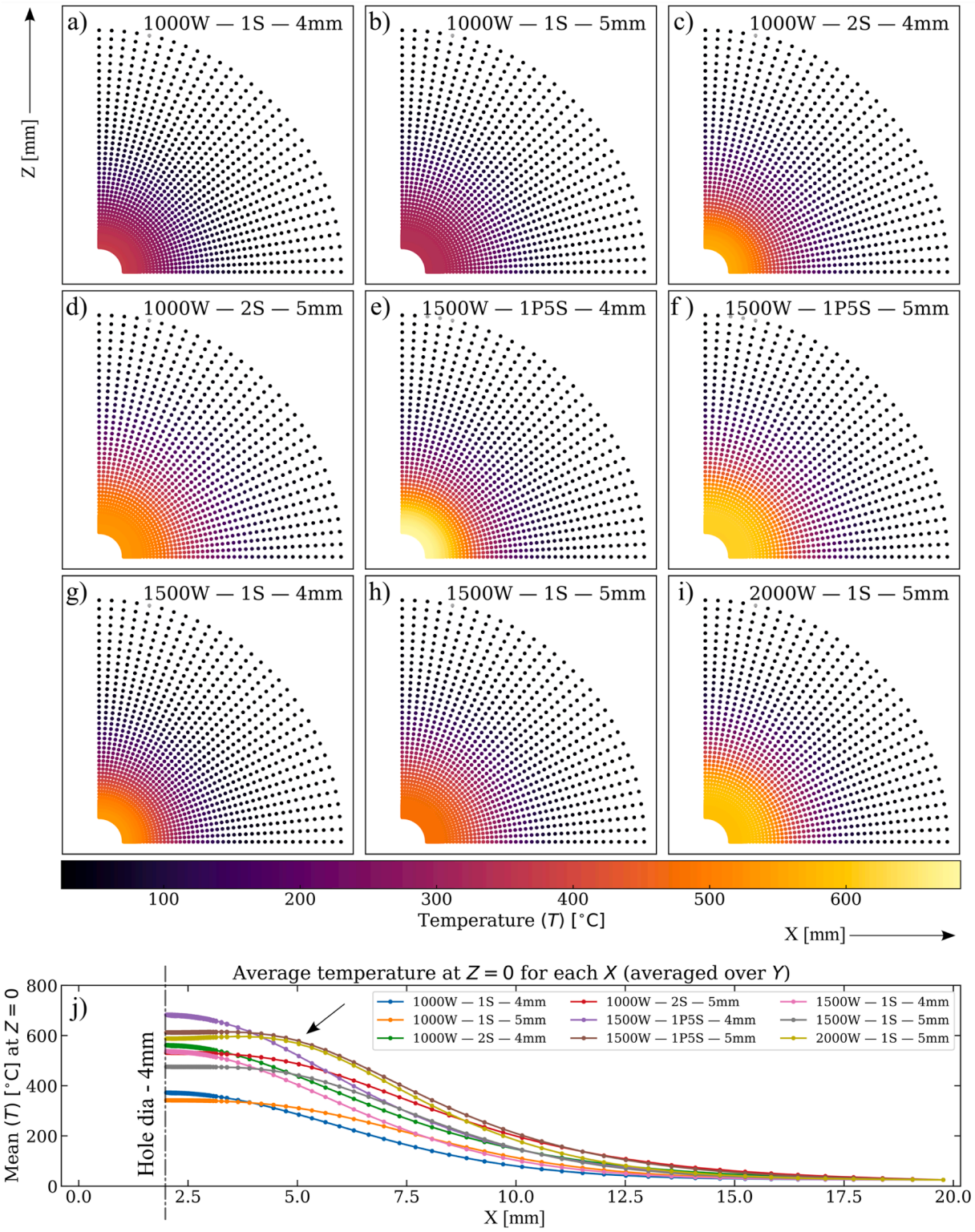



**Fig. 14.** Temperature distribution in shear cut samples post localized laser heating process for different laser process parameters: (a–i) Spatial temperature fields for varying power, exposure time, and spot size. (j) Average temperature at Z = 0 as a function of distance from the cut edge (X), averaged over sheet thickness (Y).

thermal condition. The lowest-temperature condition, C01, results in 92 deleted elements, whereas C02–C04, with forming-zone temperatures of approximately 526–554 °C, exhibit 25–26 deleted elements, corresponding to a reduction of approximately 72% relative to C01. Increasing temperature is also accompanied by a more spatially uniform wall-immobile dislocation-density distribution across the flange-edge region. The approximately 550 °C values reported for C02–C04 represent averages over the 2 mm edge region used for quantitative comparison; the local forming-zone temperature of the selected condition reaches approximately 550–600 °C, as described in Section 6.2.

Element deletion occurs when the local damage state reaches the prescribed terminal failure condition of the GTN formulation [49]. A deleted element therefore represents a region in which the simulated material has lost its load-carrying capacity after the local void-fraction

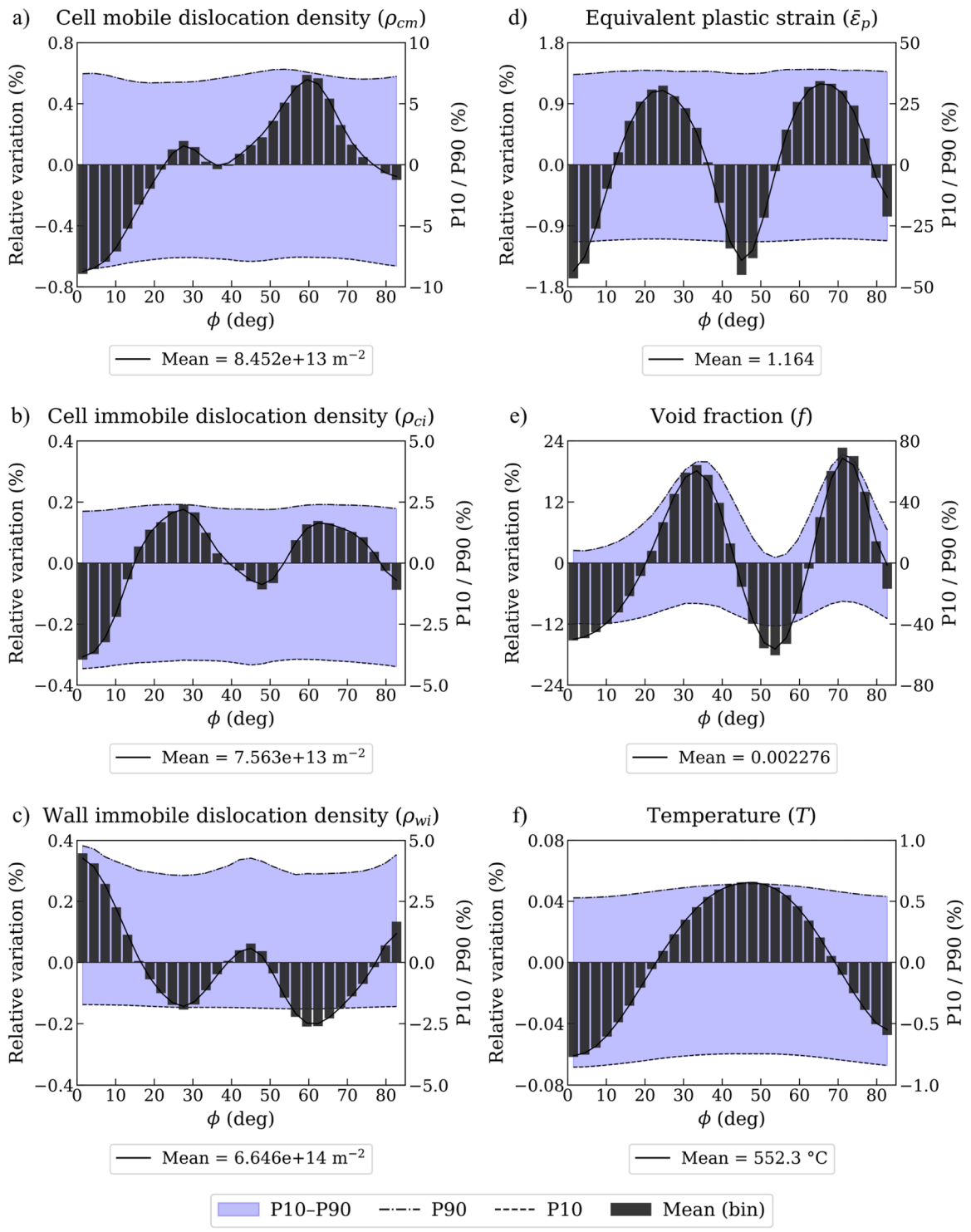



**Fig. 15.** Circumferential quantification of ICME output fields along the flange edge using angular binning: Angular distributions of B4D case (a) Cell mobile dislocation density $\rho_{cm}$, (b) Cell immobile dislocation density $\rho_{ci}$, (c) Wall immobile dislocation density $\rho_{wi}$, (d) Equivalent plastic strain $\bar{\varepsilon}_p$, (e) Void fraction $f$, and (f) Temperature $T$. Bars show deviations of arithmetic bin means from the corresponding circumferential mean, while the shaded region indicates the $P_{10}$–$P_{90}$ variability range.

evolution reaches the failure criterion; it is not interpreted as an individual physical pore, crack, or direct measure of crack length. Since all configurations employ the same mesh, constitutive parameters, failure criterion, and post-processing procedure, the deleted-element count provides a relative measure of the spatial extent of numerical fracture between the investigated cases. The final mean void fraction, in contrast, is evaluated only from elements remaining active at the final frame and therefore characterizes the retained damage state of the surviving material. The two quantities are consequently treated as complementary indicators (Section 7.6).

Blank inversion in C05 further modifies the predicted failure distribution. Positioning the more severely damaged fracture-zone side of the shear-cut edge toward the inner flange surface results in 14 deleted elements, the lowest count among the investigated configurations, while a

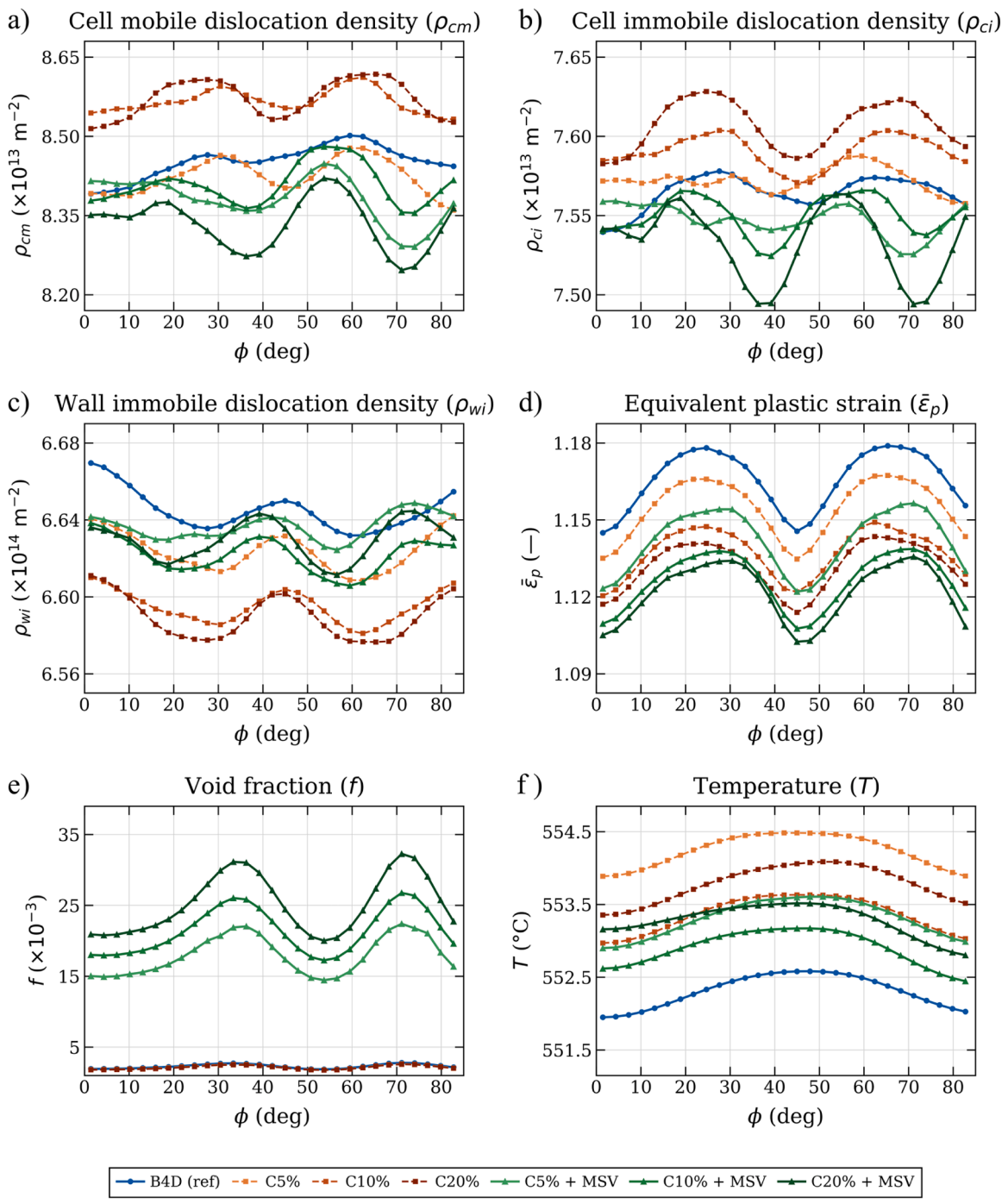



**Fig. 16.** Angular distribution of microstructural and mechanical state variables along the flange edge: (a) cell mobile dislocation density $\rho_{cm}$, (b) cell immobile dislocation density $\rho_{ci}$, (c) wall immobile dislocation density $\rho_{wi}$, (d) equivalent plastic strain $\bar{\varepsilon}_p$, (e) void fraction $f$, and (f) temperature $T$. Results compare the baseline case (B4D), different clearances (C5–C20%), and simulations with microstructural state variable (MSV) inheritance.

non-zero void-fraction field remains in the surviving edge material ($f = 0.0207$, compared to 0.017 to 0.018 for C02 through C04). Relative to the corresponding non-inverted configuration C04, the deleted-element count is reduced by approximately 44%. The result indicates a redistribution of the critical edge state with respect to the tensile outer flange surface rather than complete removal of the inherited damage.

### 6.8. *Macroscopic experimental assessment of cold and laser-assisted flange forming*

The macroscopic forming response was assessed using representative experimental cross-sections and the corresponding FE predictions for the cold and laser-assisted conditions. Fig. 23(a–d) compares the final flange geometries, while Fig. 23(e–f) shows the local thickness profiles along the flange height. For both conditions, the simulations reproduce the characteristic thickness evolution from the flange root toward the edge, including the pronounced thinning in the upper flange region. Local deviations remain in the intermediate-height region, where the cold-forming simulation predicts somewhat greater retained thickness, whereas the laser-assisted simulation locally overpredicts thinning. The mean absolute thickness deviation between experiment and simulation is 0.1885 mm for cold forming and 0.1454 mm for laser-assisted forming.

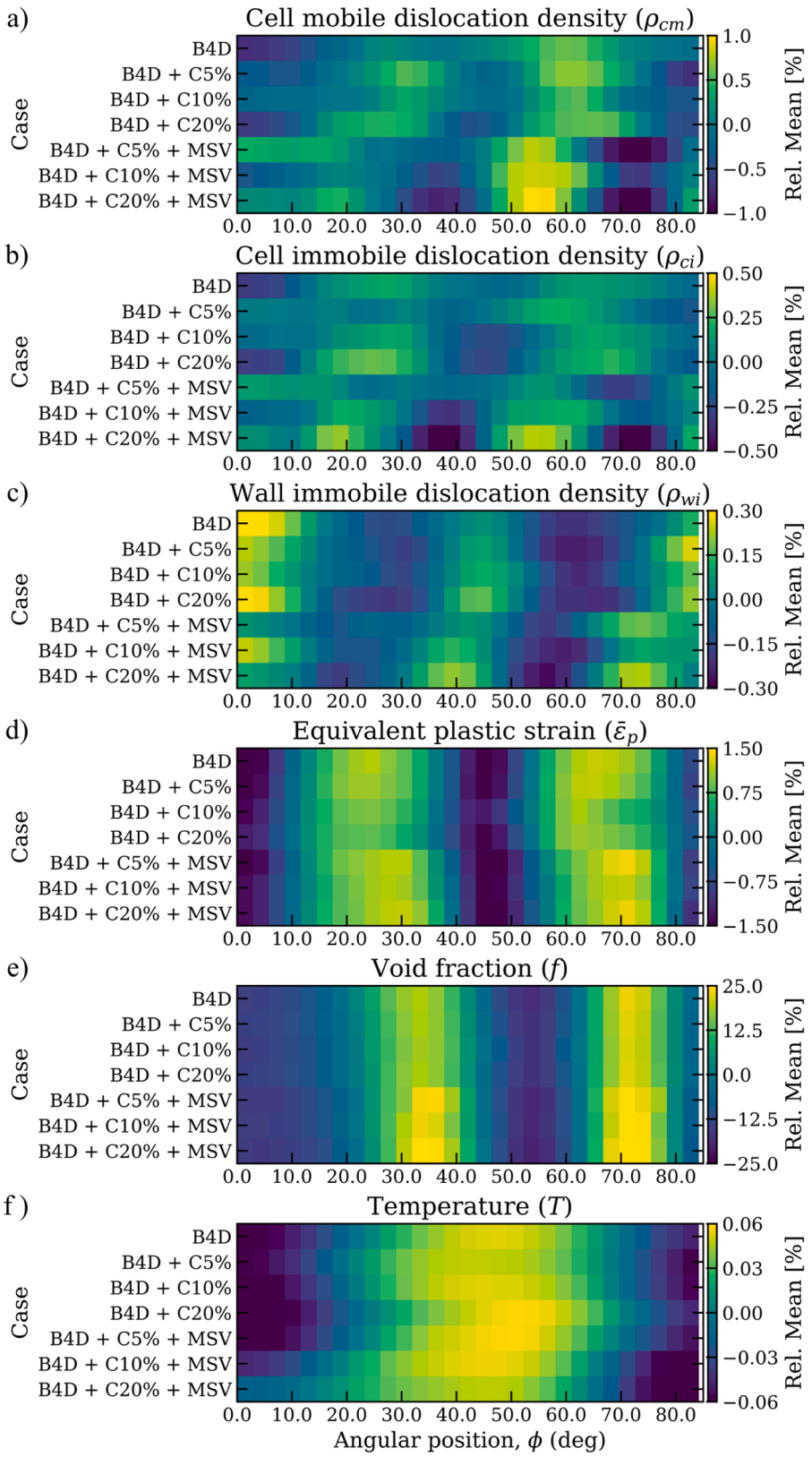



**Fig. 17.** Angular distributions of relative microstructural state variables along the flange edge:(a) cell mobile dislocation density $\rho_{cm}$, (b) cell immobile dislocation density $\rho_{ci}$, (c) wall immobile dislocation density $\rho_{wi}$, (d) equivalent plastic strain $\bar{\varepsilon}_p$, (e) void fraction $f$, and (f) temperature $T$. Values are expressed as deviations from the case-specific mean for each configuration.

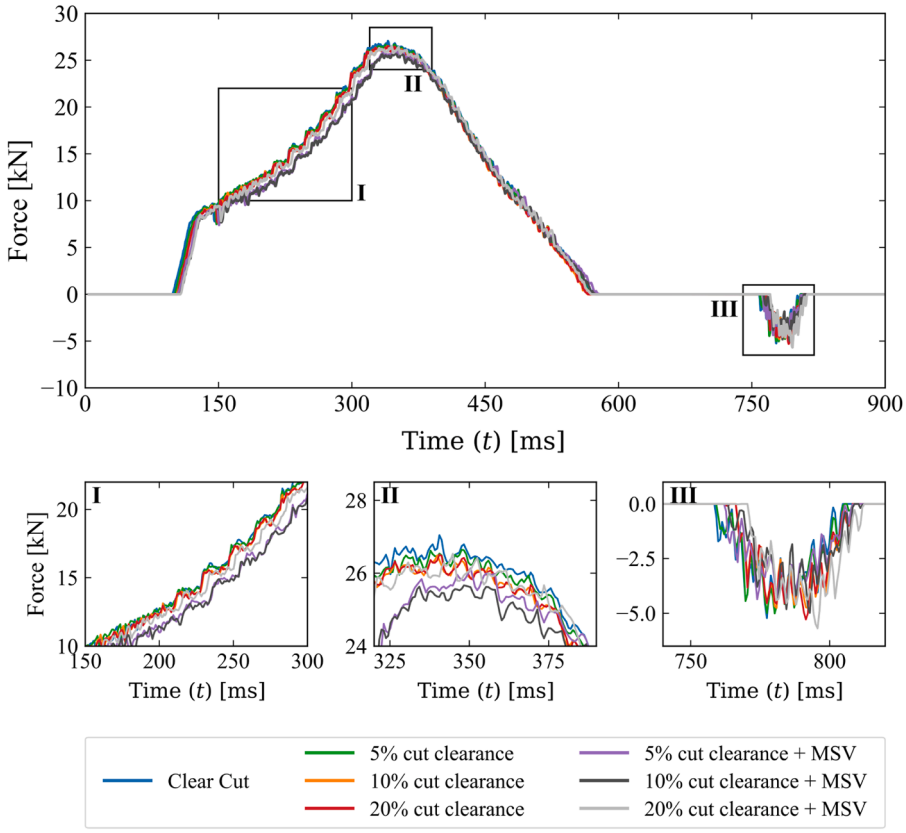



**Fig. 18.** Simulated flange-forming force histories for the ideal reference and clearance cases with and without MSV inheritance. Insets I–III highlight initial loading, peak force and unloading.

The thickness comparison is based on one representative cross-section for each condition and therefore quantifies the agreement for the investigated components rather than specimen-to-specimen variability. Moreover, the circumferential analysis presented in the preceding sections demonstrates that the flange-edge response is spatially heterogeneous. Consequently, the measured local thickness profile can depend on the angular position of the selected cross-section. Since the experimental sections were not spatially registered to the corresponding circumferential positions in the FE model, the reported deviations are interpreted as representative engineering-scale measures of geometrical agreement rather than pointwise circumferential validation.

The global mechanical response provides a complementary quantitative assessment. Fig. 23(g) compares the force history measured during the standalone cold-forming test with the corresponding numerical prediction. The experimental peak force is 33.727 kN, compared with 32.729 kN in the simulation, corresponding to an underprediction of 2.96%. The simulation also reproduces the characteristic evolution of the measured loading and unloading response. The laser-assisted simulation predicts a lower forming-force level than the cold-forming simulation, reflecting the temperature-dependent reduction in forming resistance. Together, the thickness-profile and force comparisons show that the framework reproduces the characteristic macroscopic material-flow and mechanical response of the flange-forming process. The close agreement in peak forming force is accompanied by representative agreement in the final thickness profiles, while local deviations in the thickness distribution remain.

Fig. 24 compares the simulated and experimentally measured surface-temperature histories for the investigated laser powers. During irradiation, both experiment and simulation show the expected increase in temperature with laser power, with comparatively close agreement near the peak-heating state. After the laser is switched off, the numerical response cools more rapidly than the measured response, and the deviation increases with laser power during the subsequent diffusion period. Because the exact spatial footprint and radial position represented by the pyrometer signal are not documented, the comparison is interpreted as an assessment of the temperature level and transient response within the simulated peak-heating region rather than as a pointwise validation of the forming-zone temperature. The implications of the post-irradiation discrepancy for the transferred thermal state are discussed in Section 7.5.

### 6.9. *Local microstructural assessment of the cold and laser-assisted flange states*

Following the macroscopic assessment in Section 6.8, the same representative cold- and laser-assisted components used for the thickness-profile comparison were examined locally using EBSD and SEM observations from the corresponding flange-edge regions. The assessment focuses on the dislocation-density distribution, grain morphology, crystallographic orientation, and visible damage features. The comparisons are based on representative cross-sections from one component for each forming condition. They are therefore used to assess local magnitude and qualitative spatial tendencies rather than specimen-to-specimen repeatability.

Fig. 25 compares the simulated wall-immobile dislocation density $\rho_{wi}$ with the EBSD-derived GND distributions. The cold-formed condition exhibits a broader and more heterogeneous $\rho_{wi}$ distribution near the flange edge, with a mean value of approximately $5.91 \times 10^{14}$ m$^{-2}$. The laser-assisted condition shows a narrower and more spatially uniform distribution centered at approximately $6.75 \times 10^{14}$ m$^{-2}$. The EBSD-derived GND distributions show mean values close to $8 \times 10^{14}$ m$^{-2}$ for both forming conditions. The simulated $\rho_{wi}$ and experimentally derived GND densities therefore remain within approximately a factor of 1.4 in magnitude. Because the two quantities represent different dislocation

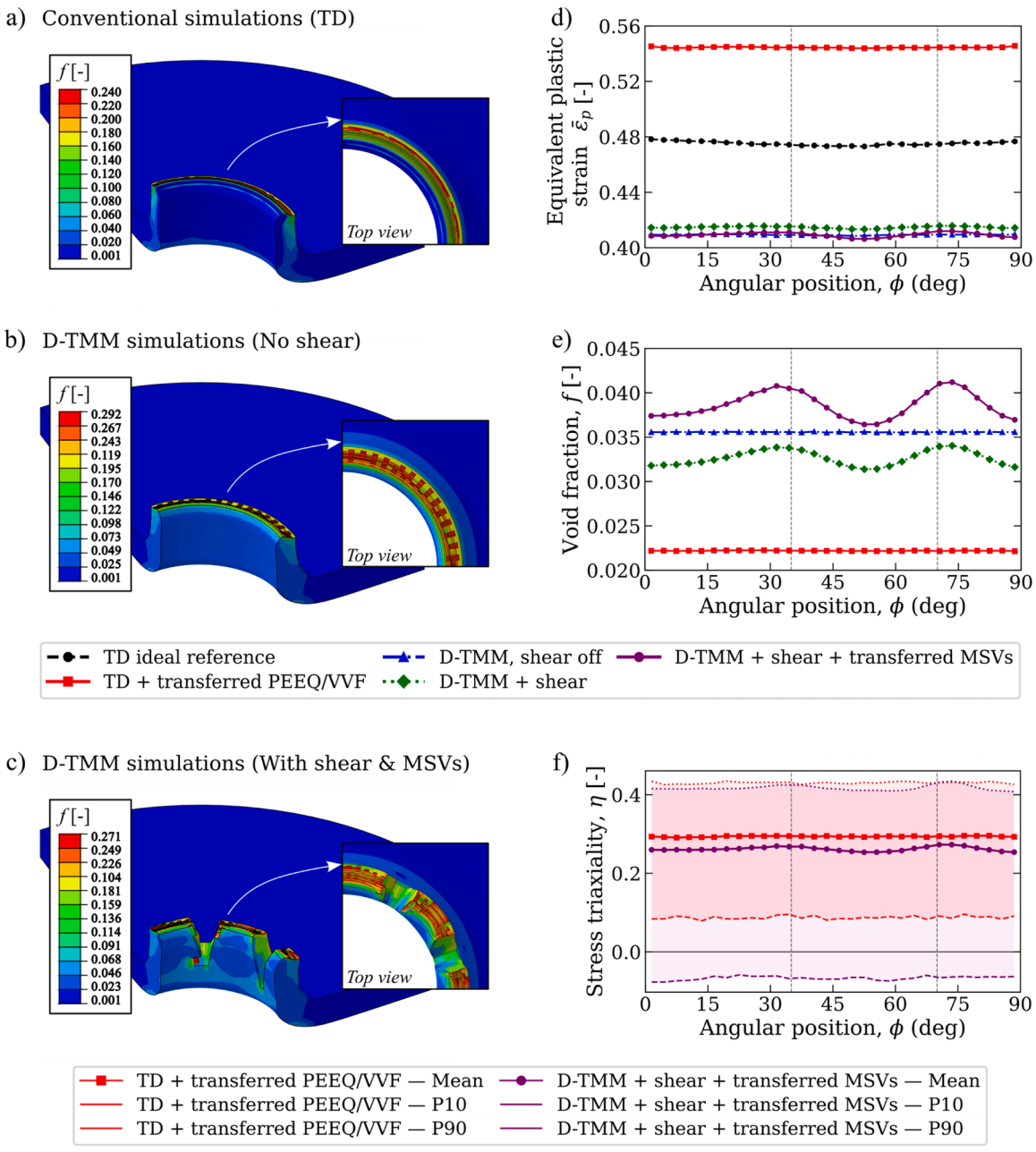



**Fig. 19.** Constitutive-control comparison of the flange-edge response. Final void-fraction fields: (a) tabulated-data (TD) model; (b) D-TMM without shear-sensitive damage; and (c) D-TMM with shear-sensitive damage and transferred MSVs. Circumferential (d) equivalent plastic strain, (e) void fraction and (f) stress triaxiality at 5 mm punch displacement; (f) includes bin means and $P_{10}$–$P_{90}$ bounds.

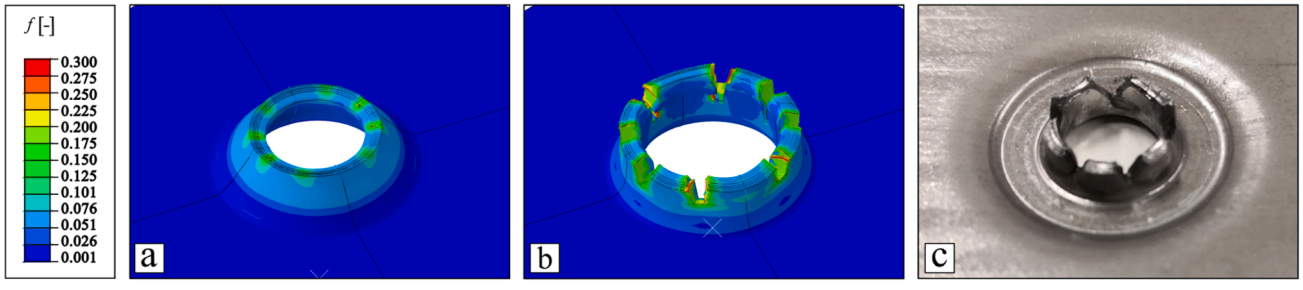



**Fig. 20.** Localized edge fracture during cold forming: (a) void fraction at 5 mm punch displacement; (b) final simulated element-deletion pattern; and (c) representative experimental edge cracks, shown for qualitative comparison.

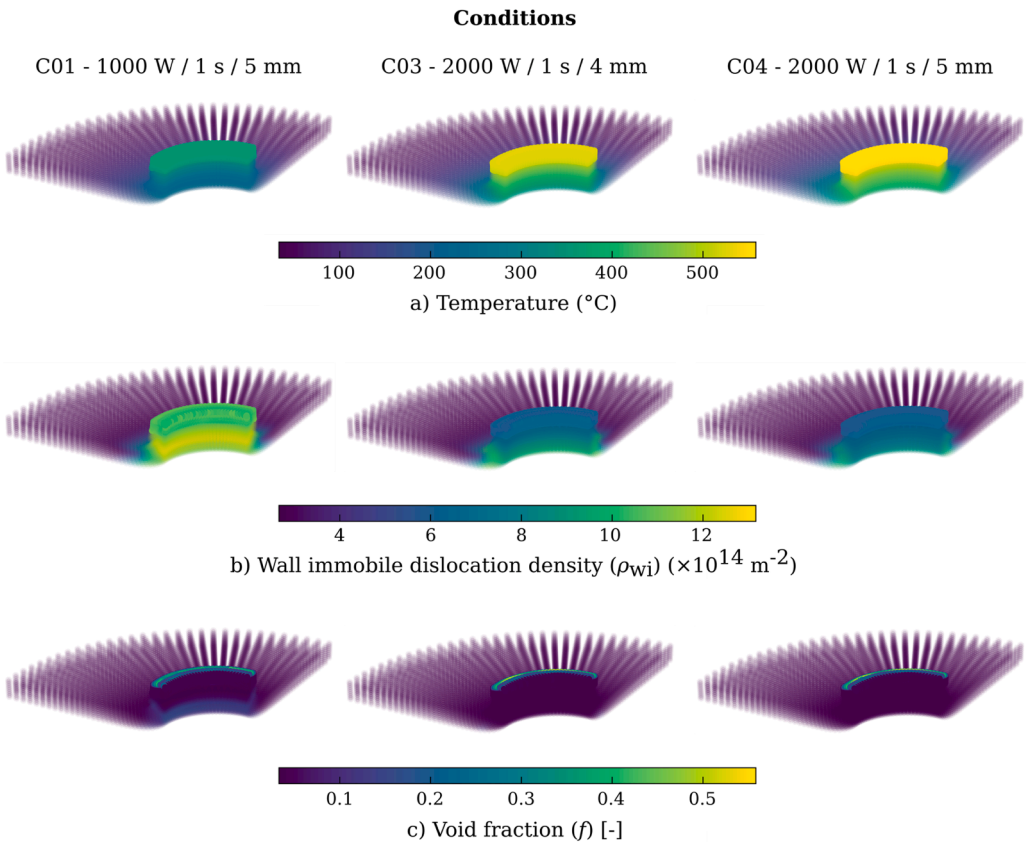



**Fig. 21.** ICME-predicted fields for selected laser-heating conditions. Columns: C01, C03, and C04; rows: (a) temperature $\boldsymbol{T}$, (b) wall immobile dislocation density $\boldsymbol{\rho_{wi}}$, and (c) void fraction $\boldsymbol{f}$.

measures and the EBSD data originate from representative local sections, this comparison is interpreted as an order-of-magnitude assessment rather than direct quantitative validation.

A direct pointwise correspondence between the two quantities is not expected. The D-TMM variable $\rho_{wi}$ represents the wall-immobile dislocation population of the constitutive model, whereas the EBSD-derived GND density represents the geometrically necessary dislocation content inferred from measured lattice-orientation gradients [80,81]. In addition, the EBSD measurements were acquired slightly below the extreme flange edge because of sample-preparation constraints. The comparison is therefore interpreted in terms of order of magnitude and distributional tendency rather than direct equivalence between the two dislocation-density measures.

The corresponding microstructural and damage observations are shown in Fig. 26. The cold-formed condition exhibits pronounced edge tearing and local microcracking. The grains in the flange-edge region are strongly elongated, with a mean aspect ratio of approximately 4.55. The elongation follows the circumferential direction of the flange, indicating a strongly directional deformation morphology. In the laser-assisted condition, the outer flange edge remains largely intact and the extent of visible cracking is markedly reduced. The grain morphology is also less elongated, with a mean aspect ratio of approximately 2.47. Compared with the cold-formed condition, the flange-edge microstructure therefore shows substantially less circumferential stretching after laser-assisted forming.

The EBSD-IPF maps show a corresponding difference in crystallographic orientation distribution. The inverse pole figures are plotted with respect to the sheet normal direction (ND), corresponding to the Z-axis of the specimen coordinate system. The cold-formed condition shows preferred orientation toward ⟨101⟩//ND, while the laser-assisted condition moderately shifts toward ⟨111⟩//ND. Since crystallographic orientation is not included as a state variable in the D-TMM formulation, the IPF observations are reported as experimental characteristics of the final deformation state. These observations characterize the different final deformation states produced by the cold and laser-assisted forming routes. The mechanistic interpretation of these observations in the context of the D-TMM framework is presented in Section 7.5.

## 7. Discussion

The coupled process-chain results provide a basis for examining how the material state introduced during shear cutting is carried through localized laser heating, combined with the resulting thermal field, and subsequently evolves during flange forming. The discussion focuses on the origin of the circumferential damage localization, the additional information introduced by dislocation-based state inheritance, and the interaction between deformation, stress state, and ductile damage. The implications of localized heating and blank orientation are then considered together with experimental evidence and the principal limitations of the numerical framework.

### 7.1. Circumferential localization and inherited edge condition

The circumferential analysis identifies two persistent regions of elevated damage near $\phi \approx 35^\circ$ and $70^\circ$. These regions remain at comparable angular positions when the circumferential discretization is varied, when the evaluated flange-edge height is changed, and when the quarter model is replaced by a half model. Their amplitudes are affected by the spatial averaging and angular resolution, whereas their locations remain comparatively stable (Section 6.1). The predicted localization is therefore considered a robust feature of the simulated three-dimensional forming response rather than an artifact of a particular post-processing choice or solely of the imposed quarter-model symmetry.

This distinction is important because the reconstructed shear-cutting

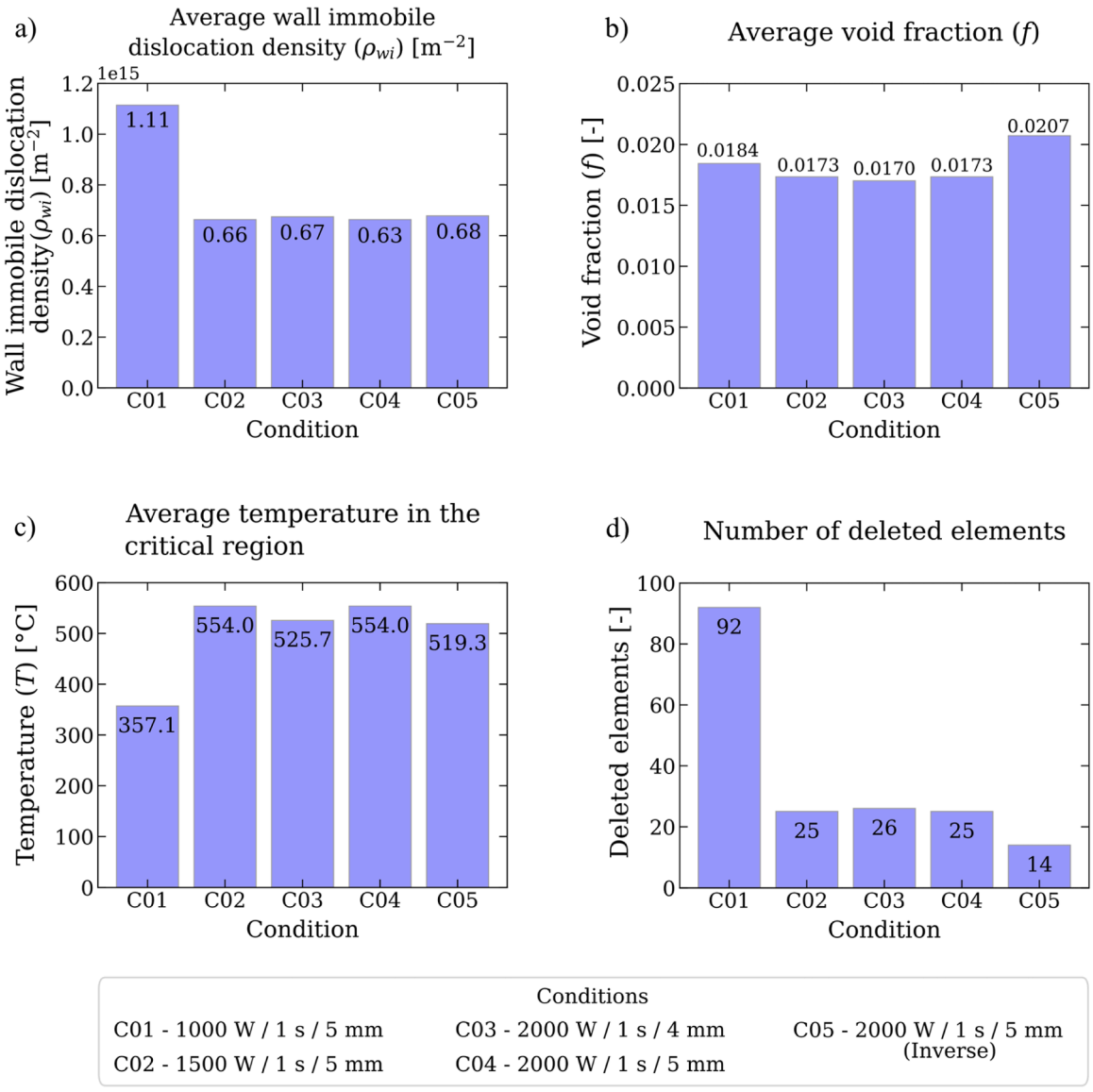



**Fig. 22.** Flange-edge response for conditions C01–C05: (a) Average wall immobile dislocation density, $\rho_{wi}$; (b) average void fraction, $f$; (c) average temperature in the critical region; and (d) number of deleted elements. C05 uses the inverted blank configuration.

state is circumferentially uniform, having been generated from an axisymmetric cutting simulation (Section 4.1). The angular heterogeneity appearing during flange forming is therefore not prescribed by the transferred initial state. Instead, it develops through the three-dimensional forming kinematics, evolving contact conditions, and the resulting local deformation and stress paths around the flange edge. The constitutive-control calculations support this interpretation (Section 6.5): when the shear-sensitive damage contribution is suppressed, these mechanical variations produce only weak circumferential variation in void fraction, whereas activation of the shear contribution produces pronounced damage maxima within the same characteristic sectors. The shear-sensitive formulation therefore does not create the preferred angular positions; rather, it makes the mechanically generated circumferential heterogeneity strongly expressed in the damage response.

The inherited cutting state primarily controls the severity of this response. Changing the transferred cutting condition substantially alters the absolute dislocation-density and void-fraction levels, while the principal angular positions remain comparatively stable. Likewise, inclusion of the cutting-induced dislocation-density state increases the damage accumulated within the critical sectors without fundamentally relocating them (Section 6.3). The simulations therefore suggest a clear hierarchy: the three-dimensional forming process establishes the circumferential mechanical heterogeneity, the shear-sensitive damage formulation converts that heterogeneity into localized ductile damage, and the inherited cutting state modifies the intensity of the subsequent response.

The predicted sectors should nevertheless not be interpreted as universal fracture angles. Real shear-cut edges can exhibit circumferential variations arising from clearance variation, tool wear, eccentricity, and misalignment [21]. Such heterogeneity would introduce a non-uniform initial state that may reinforce, weaken, or shift the forming-induced damage maxima. Resolving this interaction would require either a fully three-dimensional cutting simulation or

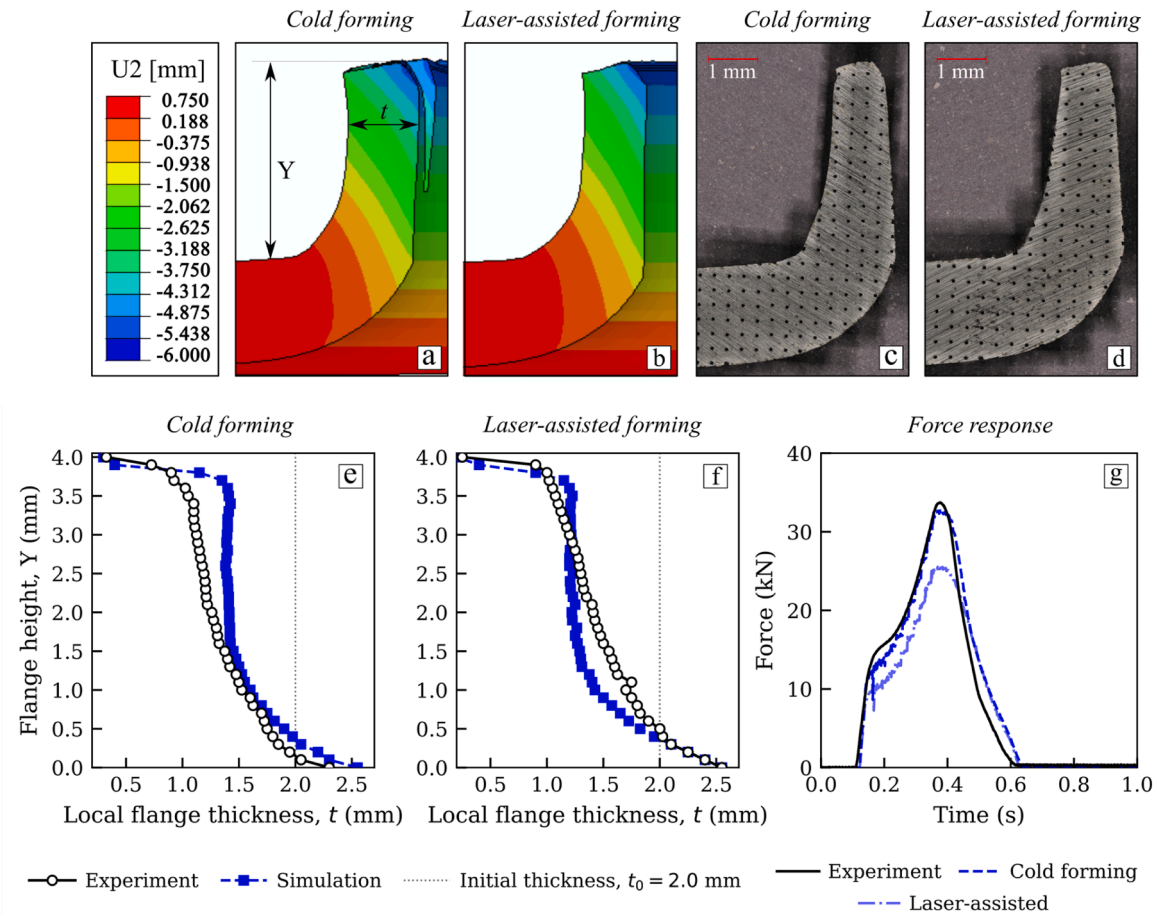



**Fig. 23.** Cold and laser-assisted flange forming: (a,b) simulated cross-sections; (c,d) experimental cross-sections; (e,f) thickness profiles, with the initial 2 mm thickness dotted; and (g) forming-force histories. Force measurements are available only for cold forming.

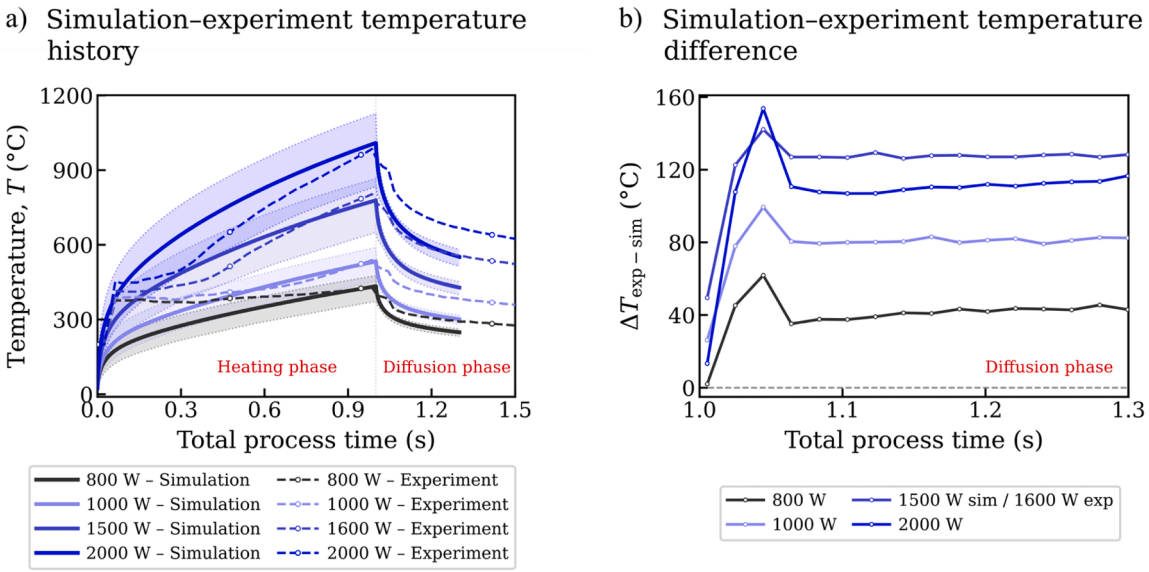



**Fig. 24.** Simulated and measured laser-heating temperatures: (a) heating (0–1 s) and diffusion (1–1.5 s) histories; solid/dashed lines denote simulations/measurements [75], and shading denotes spatial $\boldsymbol{P}_{10} - \boldsymbol{P}_{90}$ variation. (b) Experiment–simulation temperature deviation during diffusion. The 1500 W simulation is paired with the 1600 W experiment.

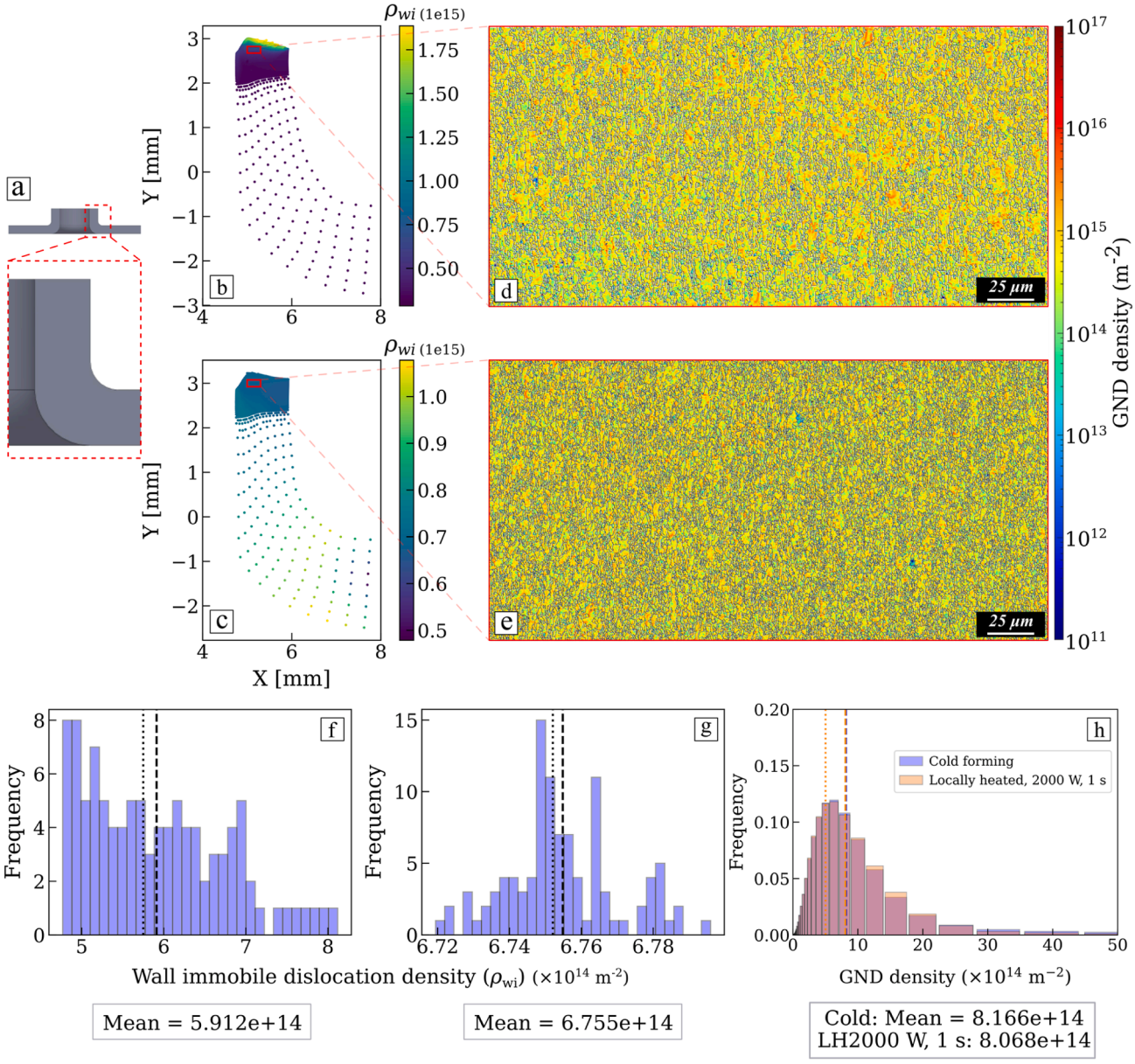



**Fig. 25.** Comparison of simulated wall immobile dislocation density ($\rho_{wi}$) and EBSD-derived GND density for cold and laser-assisted flange forming. (a) Selected flange-edge region; (b,c) simulated $\rho_{wi}$ distributions for cold forming and laser-assisted forming, respectively; (d,e) corresponding EBSD-GND maps; (f,g) simulated $\rho_{wi}$ distributions extracted from the critical region; and (h) experimental GND density distributions.

experimentally measured circumferential edge-state information and remains outside the scope of the present study.

### 7.2. Role of constitutive description and microstructural-state inheritance

The comparison with the conventional baseline clarifies what is gained by transferring an internal microstructural state rather than macroscopic history variables alone (Section 6.5). Previous process-chain approaches have improved edge-formability predictions by transferring quantities such as geometry, equivalent plastic strain, hardness, phenomenological damage, or residual-state variables from cutting to subsequent forming [5,30,35–37,39]. These studies establish the importance of upstream history but generally summarize that history through macroscopic scalar quantities. Related multi-stage hole-flanging simulations have likewise shown that damage accumulation depends on the non-proportional loading history rather than on an instantaneous strain state alone [42].

Under the present conditions, however, transfer of the shear-cut geometry together with equivalent plastic strain (PEEQ) and void volume fraction (VVF) does not reproduce the spatial damage response obtained with the complete D-TMM formulation. At the common punch displacement of 5 mm, the conventional formulation remains almost circumferentially uniform, whereas the complete D-TMM develops two pronounced regions of elevated void fraction. This difference cannot be explained by a greater accumulated plastic strain in the D-TMM calculation: the conventional model develops a higher and more uniform incremental equivalent plastic strain while simultaneously predicting a lower and substantially more uniform void fraction, despite use of the

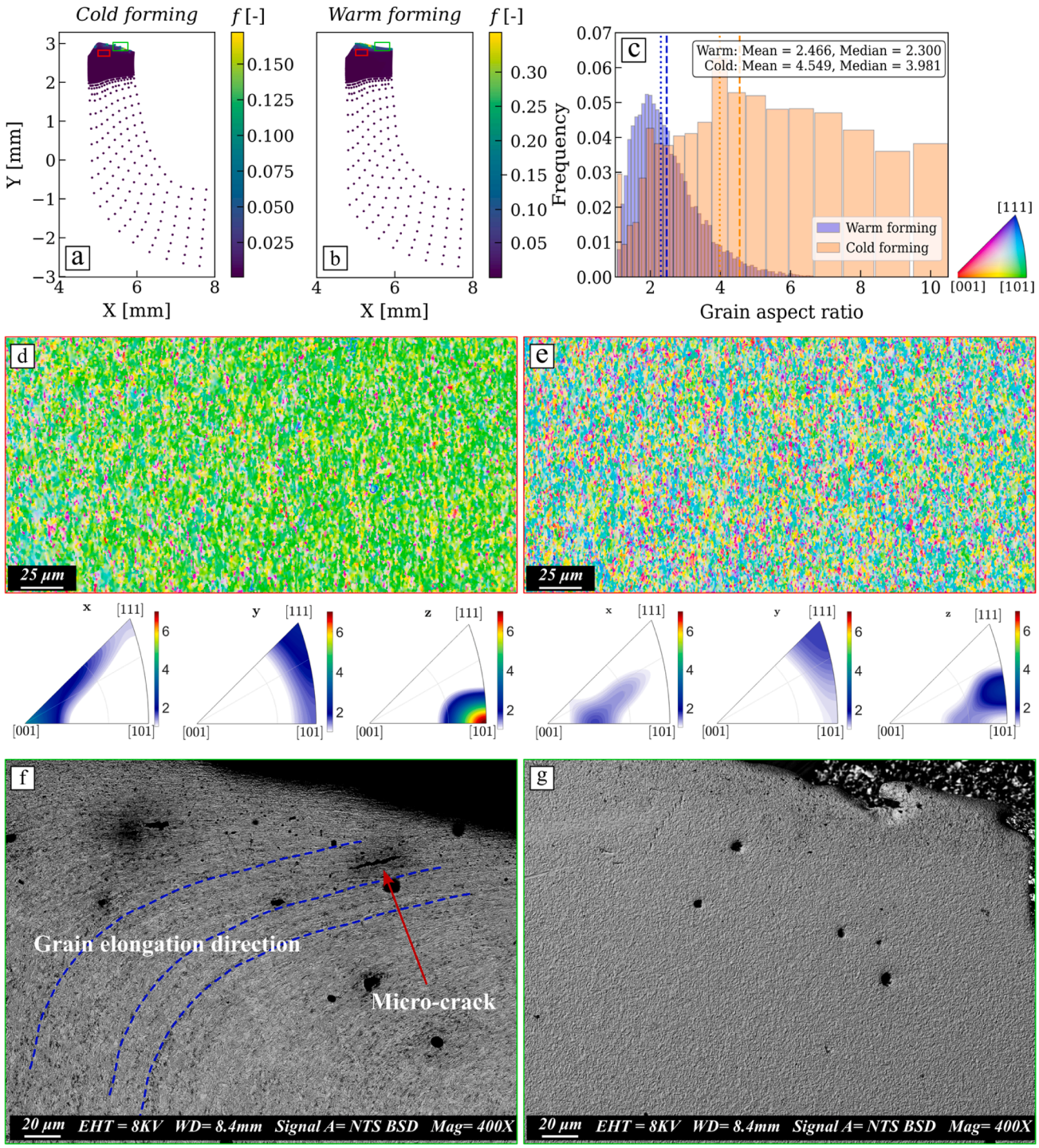



**Fig. 26.** Comparison of simulated damage and experimentally observed microstructure for cold and laser-assisted flange forming. (a,b) Simulated void fraction distributions for cold forming and reference laser-assisted condition, respectively; (c) grain aspect ratio distributions; (d,e) EBSD-IPF maps and corresponding inverse pole figures; and (f,g) SEM images showing edge microstructure and damage features for cold and laser-assisted conditions.

same conventional GTN damage formulation and parameter set.

This result, when compared with the state of failure in the representative sample, supports the motivation for transferring dislocation-based state variables. Equivalent plastic strain is a path-dependent scalar and does not uniquely describe the underlying dislocation structure [43], while hardness combines several strengthening contributions and provides only an indirect measure of microstructural state. This comparison addresses one specific conventional baseline and does not exclude the possibility that other formulations may perform differently. The amplification caused by MSV inheritance (Section 7.1) is not restricted to the initial Taylor-hardening contribution. In the D-TMM formulation, $\rho_{cm}$, $\rho_{ci}$, and $\rho_{wi}$ form a coupled internal state whose evolution follows competing dislocation mechanisms [44,49]. Mobile dislocations are generated through source activation, cross-slip and mobile-junction formation, but are simultaneously removed from the mobile population by annihilation, trapping and accumulation into

immobile structures. Trapping at stable junctions, including Lomer–Cottrell-type locks, and progressive accumulation increase $\rho_{ci}$, whereas sufficiently developed cell-immobile structures contribute to wall formation and thereby increase $\rho_{wi}$. Both immobile populations can in turn be reduced through annihilation and remobilization, the latter representing thermally activated return of previously immobilized dislocations to the mobile population [44,49]. The distinction between mobile and relatively immobile forest dislocations follows the two–density framework of Estrin and Kubin [82], while the distinction between dislocation-rich walls and softer cell interiors is consistent with Mughrabi's composite description [83] and subsequent cell–wall models [84]. The specific coupling and evolution laws for the three state variables used here follow the D-TMM formulation [44,49].

Importantly, these mechanisms depend on the **current dislocation state rather than on accumulated strain alone**. In the constitutive equations, mobile-dislocation generation scales with $\rho_{cm}/\sqrt{\rho_{ci}+\rho_{wi}}$, trapping with $\rho_{cm}^{3/2}$, wall nucleation with $\rho_{ci}^{3/2}\rho_{cm}$, annihilation with products of the mobile and interacting dislocation populations, and remobilization with the corresponding immobile density [44,49]. The cutting-generated state therefore changes not only the initial flow resistance through the Taylor relation, but also the subsequent rates of dislocation generation, storage, rearrangement and recovery during flanging. Two material points with the same transferred equivalent plastic strain can consequently enter the forming step with different dislocation partitions and follow different hardening and plastic-flow trajectories. This explains why transfer of $\rho_{cm}, \rho_{ci}$, and $\rho_{wi}$ can amplify the strain and void-fraction response even when the conventional PEEQ-based baseline predicts a similar or higher accumulated plastic strain. The individual dislocation populations should, however, not be interpreted as direct damage indicators: the preceding flange-forming study showed that highly deformed edge regions may exhibit depletion of $\rho_{cm}$ together with redistribution, rather than monotonic growth, of the immobile populations [31]. Their significance lies in controlling the evolving constitutive state from which damage subsequently develops, not in serving as direct indicators of fracture.

### 7.3. Damage evolution and fracture interpretation

The implemented damage formulation combines strain-driven void nucleation $(\dot{f}_n)$, conventional stress-state-dependent void growth $\left(\dot{f}_g\right)$, and a shear-sensitive contribution $(\dot{f}_s)$ to the evolution of the void fraction. Nucleation follows the Chu–Needleman formulation [85] (Eq. (A.14)), in which the nucleation rate is governed by accumulated equivalent plastic strain through a Gaussian distribution centred on the characteristic nucleation strain. Conventional GTN growth, in contrast, is promoted by positive hydrostatic stress and becomes progressively less effective as stress triaxiality decreases. The shear contribution follows the modification of Nahshon and Hutchinson [86] and is multiplied by the triaxiality-dependent weighting proposed by Nielsen and Tvergaard [87] (Eq. (A.16)). It therefore provides a phenomenological representation of shear-assisted damage that cannot be captured by hydrostatic void expansion alone.

The observed spatial precedence of $\bar{\varepsilon}_p$ over $f$ is consistent with the strain-controlled nucleation kinetics, but the constitutive interaction is not one-directional. Within the D-TMM formulation, the plastic strain increment, hydrostatic stress, void fraction, and the three dislocation-density populations are solved as a coupled material-point state [49]. The immobile populations $\rho_{ci}$ and $\rho_{wi}$ modify the local flow resistance through the Taylor relation [44,49], while mobile-dislocation activity associated with $\rho_{cm}$ governs the plastic strain rate. The resulting plastic increment simultaneously drives dislocation evolution and Chu–Needleman nucleation, whereas the evolving void fraction modifies the porous GTN yield surface and hence the subsequent plastic correction. The local response therefore develops through a feedback between dislocation substructure, plastic flow, stress state, and void evolution rather than through accumulated plastic strain alone (Section 7.2).

The local stress-state evolution explains why pronounced damage develops despite only moderate variation in equivalent plastic strain. Although the bin-averaged triaxiality within the critical sectors remains positive, the distribution broadens during deformation, and individual material points approach lower-triaxiality states (Fig. 19). As $\eta$ decreases below $\eta_1$, the weighting function $\Omega\eta$ equals to unity, which increases the shear-sensitive contribution, while conventional volumetric void growth becomes less dominant. Micromechanically, low-triaxiality ductile failure is associated with void distortion, elongation and rotation together with shearing of the ligaments between neighbouring voids, ultimately promoting localization and coalescence [86–88]. The present model does not resolve these changes in void morphology explicitly; their macroscopic effect is represented through the additional shear-dependent void-fraction evolution term. Void nucleation, conventional growth, and shear-assisted evolution can therefore act concurrently, with their relative contributions changing continuously with the evolving local deformation and stress state.

Regions of elevated void fraction are present before extensive element deletion and subsequently develop into separated numerical fracture zones with continued forming. The cold-formed specimens similarly exhibit discrete circumferential edge cracking rather than continuous failure around the flange, providing qualitative support for the predicted progression from localized damage accumulation to separated fracture (Section 6.6). The experimental evidence is, however, limited to the final fractured state and therefore does not validate the temporal crack-initiation sequence or the exact angular positions of the individual simulated fracture sites.

### 7.4. Global response versus local damage prediction

The global force response provides an important engineering-scale assessment of the forming model, but it also illustrates why macroscopic agreement alone is insufficient for evaluating edge-formability predictions. For the standalone cold-forming experiment, the measured peak force of 33.727 kN is reproduced by the simulation at 32.729 kN, corresponding to an underprediction of only 2.96%. The representative thickness profiles provide a second macroscopic measure, with mean absolute deviations of 0.1885 mm for cold forming and 0.1454 mm for laser-assisted forming. The selected laser-assisted simulation additionally reduces the peak forming force to approximately 25–26 kN, i.e. about 20–22% below the simulated cold-forming peak, reflecting the reduced forming resistance of the locally heated edge. This latter force reduction is a numerical comparison; the progressive-die force signal cannot provide an equivalent experimental flange-force value because several stations contribute simultaneously. These global measures are comparatively insensitive to some of the local changes revealed by the process-chain analysis. Variation of the inherited cutting state produces substantial differences in the edge-region dislocation-density and damage fields, while the corresponding force histories remain closely grouped. The cutting-clearance and state-transfer configurations, for example, produce peak forces of approximately 26–27 kN, with a spread of approximately 1–2 kN, despite markedly different local damage levels.

This difference in sensitivity arises from the spatial scales represented by the respective measures. Punch force integrates the mechanical resistance over the complete tool–sheet interaction region, whereas the cutting-induced gradients and subsequent damage localization are

confined to a comparatively small volume near the flange edge. Significant changes in the constitutive trajectory of this region can therefore control fracture without producing a proportionally large change in the resultant force. The circumferential state-variable analysis is consequently not a substitute for global force validation but a complementary level of assessment: the force response evaluates the overall forming resistance, whereas the spatially resolved fields distinguish process histories that appear nearly equivalent at the macroscopic scale.

### 7.5. Effect of localized heating and process configuration

The temperature comparison in Section 6.8 provides the starting point for interpreting the laser-assisted forming results. During the 1 s irradiation, the simulations reproduce the experimentally observed increase in surface temperature with laser power and show close agreement in the peak-heating response. For the directly comparable 800, 1000, and 2000 W conditions, the differences near the end of irradiation are approximately 10–30 °C, while the 1500 W simulation and 1600 W experiment are not treated as a direct error pair because of the different applied powers. After the laser is switched off, the agreement progressively decreases, particularly at the higher powers: the numerical model cools more rapidly, and the temperature difference reaches over 100 °C during the subsequent diffusion period for the highest-power conditions. This distinction is important because the temperature retained after diffusion, rather than the instantaneous laser-heating peak, defines the thermal state transferred to flange forming.

Part of this deviation is associated with limits of the thermal comparison itself. The exact radial position and optical footprint of the experimental pyrometer are not documented, whereas the simulated temperature varies substantially across the width of the irradiated ring (Section 3.3). The good agreement in peak temperature therefore supports the imposed heat-input magnitude, while the faster predicted cooling indicates remaining uncertainty in the transient thermal description that cannot presently be separated from the pyrometer spatial averaging. The deviation during cooling is particularly relevant to the process-chain prediction because an error in the transferred forming temperature propagates directly into the temperature-dependent flow and dislocation-evolution relations of the D-TMM formulation [44,49].

The constitutive validity of the selected thermal state must therefore be considered separately for the critical flange edge and the directly irradiated ring. The D-TMM formulation was calibrated experimentally up to approximately 500 °C [49], whereas the selected condition produces an average edge-region temperature of approximately 550 °C and a local post-diffusion forming-zone temperature of approximately 550–600 °C. Its application during flange forming consequently represents a moderate extrapolation of the calibrated temperature-dependent constitutive functions. Dilatometric measurements on S700MC give $A_{c1} \approx 794$ °C and $A_{c3} \approx 860$ °C at slow heating rates, with both transformation temperatures shifting upward as the heating rate increases [79]. The critical edge region considered in the damage assessment remains below the reported austenitization range. This argument does not extend to the directly irradiated annulus, where transient temperatures approach approximately 1100 °C; phase transformation may occur locally there and is not represented by the present single-phase D-TMM framework.

The short and highly transient nature of the laser cycle further constrains what can be inferred about recrystallization. Recrystallization temperature is not a fixed material constant but depends on prior deformation, heating rate, peak temperature, and holding time. Rapid-heating experiments on cold-worked low-carbon ferritic steels show that increasing the heating rate shifts the recrystallization-start temperature upward and reduces the extent of recrystallization achieved during continuous heating [89]. Overlap between ferrite recrystallization and austenite formation has likewise been reported under sufficiently rapid heating [90]. The present 1 s laser pulse followed immediately by diffusion and cooling cannot be assessed using conventional long-duration recrystallization data alone. Together with the substantially lower 550–600 °C temperature in the critical forming region, this makes extensive recrystallization at the flange edge unlikely but does not establish its absence. Since neither recrystallized fraction nor phase fraction was measured experimentally, and neither process is represented in the model, no specific recrystallization or transformation state is assigned to the flange edge.

Within these limitations, the numerical results show a clear effect of temperature on the subsequent forming response (Section 6.7). Increasing the forming-zone temperature reduces the number of deleted elements and produces a more distributed dislocation-density and damage response across the flange edge. The reduction in forming force is consistent with the lower forming resistance reported for laser-assisted forming [47,48]. The improved flange-edge response is likewise consistent with previous laser-assisted hole-flanging studies [45] reporting enhanced edge formability. In the present model, the effect arises through the complete temperature-dependent constitutive response, including the flow stress and the competing dislocation-evolution mechanisms [44,49], and should not be attributed to recrystallization or another unmeasured microstructural process.

The experimental grain morphology (Section 6.9) provides complementary evidence for this change in deformation mode. The mean grain aspect ratio decreases from approximately 4.55 after cold forming to 2.47 after laser-assisted forming. This reduction is interpreted here as evidence of less pronounced circumferential grain stretching and a more distributed deformation state, rather than as evidence of recrystallization. The laser-assisted grains nevertheless remain elongated and show a component of deformation along the $Z$-direction (tangential tensile stress direction); the deformation is therefore not fully homogeneous. This is consistent with the circumferential analysis, which shows that substantial local heterogeneity remains even under the heated condition (Section 6.3). An additional limitation is that only one metallographic section was evaluated for each forming condition. Both cold- and laser-assisted specimens were sectioned with the same orientation relative to the rolling direction, so the comparison is directionally consistent; however, their exact circumferential positions were not registered. The measured aspect ratios may therefore contain a contribution from the angular heterogeneity identified numerically and should be interpreted as representative local observations rather than circumferential averages.

Blank orientation provides a second process-control mechanism that is independent of the thermal input. Inverting the shear-cut blank changes which side of the inherited edge state forms the inner and outer flange surfaces (Section 6.7). The C05 configuration produces the lowest deleted-element count and improved predicted integrity of the outer flange surface, while a non-zero retained void-fraction field remains (see Section 7.6 for interpretation of these measures). The result therefore reflects a redistribution of the inherited high-damage region relative to the surface subjected to the critical forming state rather than elimination of the cutting-induced damage. Taken together, the results identify localized heating and blank orientation as complementary means of modifying the flange-edge response. These configurations represent the most favourable conditions within the investigated parameter space, but not a general process optimum.

### 7.6. Failure criterion and scope of process assessment

Ductile damage is represented by the GTN void-fraction variable $f$. Within the implemented formulation, the critical void fraction $f_C$ marks

the onset of accelerated coalescence, whereas $f_F$ defines the terminal failure state [49], which is associated with element deletion in the VUMAT implementation. These quantities are constitutive damage variables calibrated against forming-induced fracture and should not be interpreted as directly measurable porosity or physical defect-size thresholds. Deleted-element counts are therefore used only for relative comparison between simulations employing the same mesh, material formulation, and failure criterion.

The damage parameters were calibrated using smooth tensile, notched, and shear specimens spanning different stress states and deformation modes [31,49]. The present process chain subjects material points to more complex and evolving loading histories than those individual calibration experiments. Application of the model to flange forming therefore represents an extension of the calibrated constitutive response to non-proportional process loading. The control calculations and fracture-development results provide process-level support for this application, but do not constitute an independent recalibration of the failure criterion.

This distinction is important when interpreting the circumferential results. The local $f$-field describes damage retained in elements that remain active, whereas deleted elements identify locations where the terminal constitutive failure condition has already been reached. Consequently, the final circumferential mean of $f$ and the deleted-element count are complementary rather than interchangeable measures: a configuration may contain fewer surviving regions of high $f$ because the most severely damaged material has already been removed numerically. Element deletion itself represents loss of local load-carrying capacity within the continuum formulation and is therefore not equivalent to an individual physical void, crack, or measurable crack length. Its spatial distribution is used here to compare the relative extent and localization of forming-stage fracture.

The same limitation applies when relating the final state to subsequent component performance. Surface-connected defects and small discontinuities are well established as fatigue-relevant stress concentrators [91,92], but the homogenized GTN void fraction cannot be converted directly into the defect size or crack geometry required for fatigue or fracture-mechanics assessment. Improved forming-stage surface integrity does not by itself establish improved service life. The process-quality assessment adopted here is therefore restricted to manufacturing-stage formability. Process conditions are compared using the occurrence and spatial extent of numerical fracture together with the distribution of retained subcritical damage. The predicted final material state can, in principle, serve as an initial condition for subsequent process or service simulations, but application-specific fatigue, corrosion, contact, and lifetime criteria remain outside the scope of the present work.

### 7.7. Validation scope and outlook

The experimental comparisons support the proposed framework at several complementary scales. The force and thickness comparisons provide quantitative assessments of the macroscopic response (Section 7.4). The thermal comparison supports the predicted peak-heating response but also reveals increasingly rapid numerical cooling after irradiation. At the microstructural scale, the EBSD-derived GND measurements provide an order-of-magnitude comparison with the simulated wall-immobile dislocation density, while the EBSD/SEM observations provide qualitative evidence for the different deformation and fracture states produced by cold and laser-assisted forming.

These comparisons should not be interpreted as a statistical validation of the complete process chain. Only one representative metallographic section was evaluated for each forming condition, and the corresponding circumferential positions were not registered to the numerical model. The measured thickness, GND density, grain morphology, and damage features therefore sample the circumferentially heterogeneous state identified numerically rather than providing pointwise spatial validation. The thermal model reproduces the irradiation peak more closely than the subsequent cooling response, introducing uncertainty into the exact temperature transferred to forming.

Within these limitations, the combined results demonstrate the central value of the proposed process-chain framework: process routes that exhibit similar global force and geometry can retain markedly different local constitutive and damage states. The circumferentially resolved transfer and evolution of the material-state variables therefore provide information that is inaccessible from global process quantities alone and enable the inherited shear-cut condition to be linked explicitly to the subsequent forming-stage response.

Future work should consequently focus on the aspects that currently limit quantitative local validation. Spatially registered EBSD/SEM measurements at several circumferential positions and repeated specimens would allow the predicted localization pattern and its variability to be assessed directly. Three-dimensional shear-cutting simulations could introduce realistic circumferential heterogeneity into the inherited edge state, while improved characterization of the laser footprint and cooling response would reduce uncertainty in the transferred thermal field. Extension of the constitutive framework to include recrystallization and phase-transformation kinetics would further broaden its applicable temperature range. Finally, transfer of the predicted post-forming material state into fatigue or other service-loading simulations would extend the present manufacturing-stage ICME framework toward component-performance assessment.

## 8. Conclusions

This work establishes a microstructure-informed ICME framework for the process-chain simulation of laser-assisted flange forming of S700MC steel. Shear cutting, localized laser heating, and flange forming are coupled through deterministic transfer of the deformed geometry, three dislocation-density state variables, void fraction, and the post-heating temperature field. Two methodological developments are introduced: a deterministic four-step variable-transfer procedure that maps the D-TMM state across simulations of differing dimensionality and mesh topology, and a circumferential statistical binning method that resolves the angular distribution of each field along the flange edge. The framework was assessed against thermal, force, geometrical, and local microstructural measurements. The principal conclusions are:

1. **Deterministic transfer of the inherited cutting state changes the subsequent constitutive response beyond what is represented by equivalent plastic strain alone.**
   The transferred dislocation-density populations and void fraction modify the local flow resistance, dislocation evolution, and damage trajectory during flange forming. Compared with geometry- and conventional transferred-state descriptions, MSV inheritance increases the magnitude of damage within the critical flange-edge sectors while leaving their principal angular positions largely unchanged.
2. **The characteristic circumferential damage localization results from the interaction between three-dimensional forming kinematics and the shear-sensitive damage formulation.** Control simulations show that suppressing the shear-sensitive contribution largely removes the localized void-fraction pattern, whereas activating it produces the two characteristic damage sectors. The inherited MSV state subsequently amplifies the damage severity

within these mechanically generated regions. Thus, plastic-strain magnitude alone is insufficient to explain the observed localization.

3. **Circumferential quantification reveals local differences that are largely hidden in global process measures.** Simulations with similar global force histories and comparable thickness profiles develop substantially different local dislocation-density and damage distributions. The standalone cold-forming simulation reproduces the experimental peak force within 3%, and representative thickness profiles show mean absolute deviations below 0.2 mm for both conditions. Despite this macroscopic agreement, the local edge states differ substantially between process configurations, demonstrating the need to complement macroscopic validation with spatially resolved state-variable assessment.
4. **Localized heating substantially modifies the forming response, although the thermal and constitutive scope must be considered.** The thermal model reproduces the experimentally measured heating response closely, with differences of approximately 10–30 °C near the end of irradiation for directly comparable conditions, while the subsequent cooling is predicted too rapidly and deviations increase to exceeding 100 °C for the highest-power condition. The selected forming region reaches approximately 550–600 °C, slightly above the 500 °C calibration range of the D-TMM formulation and therefore represents a limited constitutive extrapolation. Within this range, laser-assisted forming reduces forming resistance and numerical fracture and produces a less strongly localized deformation state compared with cold forming.
5. **Blank orientation provides an additional means of controlling the spatial position of forming-stage damage.** Inverting the shear-cut blank relocates the more severely affected side of the inherited edge relative to the outer flange surface and produces the lowest deleted-element count among the investigated configurations. The result represents redistribution rather than elimination of damage, since a non-zero retained damage field remains in the surviving flange material. The inverted configuration should therefore be interpreted as the most favourable condition within the investigated process space rather than as a universal optimum.

Overall, the study shows that process-chain predictions based only on global force, geometry, or scalar deformation measures can overlook local material-state differences that govern edge fracture. By preserving the cutting-induced dislocation and damage state through the heating stage and resolving its subsequent evolution during forming, the proposed framework provides a basis for comparing process routes at the level at which local failure develops, while also defining the limitations that must be addressed for subsequent service-life or higher-temperature applications.

## Declaration of generative AI and AI-assisted technologies in the writing process

During the preparation of this work the first author Karthik Ramalingam used AI tools (Anthropic and OpenAI) to assist with language editing and improving readability of the manuscript. After using this tool/service, the author reviewed and edited the content as needed and takes full responsibility for the content of the publication.

## CRediT authorship contribution statement

**Karthik Ramalingam:** Writing – review & editing, Writing – original draft, Visualization, Software, Methodology, Formal analysis, Data curation, Conceptualization. **Tobias Schmid:** Writing – original draft, Formal analysis, Data curation. **Bohang Gao:** Writing – original draft, Formal analysis, Data curation. **Florian Hüsing:** Writing – review & editing, Supervision, Methodology. **Christian Haase:** Writing – review & editing, Supervision, Methodology. **Christian Brecher:** Writing – review & editing, Supervision, Funding acquisition. **Ulrich Krupp:** Writing – review & editing, Supervision, Funding acquisition.

## Declaration of competing interest

The authors declare that they have no known competing financial interests or personal relationships that could have appeared to influence the work reported in this paper.

## Acknowledgements

The authors express their gratitude to the German Federal Ministry for Economic Affairs and Climate Action under the IGF program (Industrielle Gemeinschaftsforschung) for providing the grant for the overall framework. We also thank the Research Association EFB e.V. for supporting the research project "**Mikrostrukturbasierte Simulation zum Kragenziehen von AHSS**" under number 21257N, which enabled us to conduct this research and laid the foundation for this publication. The first author would like to gratefully acknowledge Dr.-Ing. S. Amir H. Motaman for sharing his finite element modeling work on hole-flanging simulations, which provided a valuable foundation and served as an important starting point for the present study, and Dr.-Ing. Marion Kreins for supporting microstructural characterizations.

## Appendix A. D-TMM model parameter expansions and mechanism kinetics

This appendix collects the explicit forms of the temperature- and strain-rate-dependent coefficients, the dislocation evolution mechanisms, and the void-fraction kinetics used in the D-TMM constitutive equations of Section 2.

### *Appendix A.1. Viscous flow stress*

The viscous component of the flow stress in Eq. (2) follows

$$\sigma_v = \sigma_{v0}\,\dot{\bar{\varepsilon}}_p^{m_v}, \tag{A.1}$$

with the reference viscous stress ($\sigma_{v0}$) and strain-rate sensitivity exponent ($m_v$) expanded as

$$\sigma_{v0} = \sigma_{v00}[1 + r_v(\widehat{T} - 1)^{s_v}],\ r_v < 0; 0 < s_v \leq 1, \tag{A.2}$$

$$m_v = m_{v0}\left[1 + r_v^m(\widehat{T}-1)^{s_v^m}\right]\dot{\widehat{\varepsilon}}_p^{m_v^m},\ \widehat{T} \equiv \frac{T}{T_0};\ \dot{\widehat{\varepsilon}}_p \equiv \frac{\dot{\bar{\varepsilon}}_p}{\dot{\varepsilon}_0}, \tag{A.3}$$

where $\sigma_{v00}$ and $m_{v0}$ are the reference values at $T_0$ and $\dot{\varepsilon}_0$, and $r_v$, $r_v^m$, $s_v$, $s_v^m$ are the temperature-dependence parameters.

*Appendix A.2. Modified void fraction*

The modified void fraction $f^*$ in the GTN yield function (Eq. (1)) accounts for void coalescence,

$$f^* = \begin{cases} f & if:\ f \le f_C \\ f_C + \dfrac{f_U^* - f_C}{f_F - f_C}(f - f_C) & if: f > f_C \end{cases}, \tag{A.4}$$

where $f_C$ is the critical void fraction at the onset of coalescence, $f_F$ is the void fraction at failure, and $f_U^* = \frac{1}{q_1}$.

*Appendix A.3. Dislocation evolution mechanisms*

Each mechanism term entering the dislocation balance equations (Eqs. (5)–7) takes a constitutive form proportional to a kinetic prefactor, the relevant dislocation density product, and the plastic strain rate. The complete set is

$$\dot{\widehat{\rho}}_{cm}^{gn} = Mc_{cm}^{gn}\frac{\widehat{\rho}_{cm}}{\sqrt{\widehat{\rho}_{ci} + \widehat{\rho}_{wi}}}\dot{\bar{\varepsilon}}_p; \tag{A.5}$$

$$\dot{\widehat{\rho}}_{xy}^{an} = Mc_{xy}^{an}\widehat{\rho}_{cm}\widehat{\rho}_{xy}\ \dot{\bar{\varepsilon}}_p; xy = cm,\ ci,\ wi; \tag{A.6}$$

$$\dot{\widehat{\rho}}_{xi}^{ac} = Mc_{xi}^{ac}\sqrt{\widehat{\rho}_{xi}}\,\widehat{\rho}_{cm}\ \dot{\bar{\varepsilon}}_p; x = c, w; \tag{A.7}$$

$$\dot{\widehat{\rho}}_{cm}^{tr} = Mc_{cm}^{tr}\widehat{\rho}_{cm}^{3/2}\ \dot{\bar{\varepsilon}}_p; \tag{A.8}$$

$$\dot{\widehat{\rho}}_{wi}^{nc} = Mc_{wi}^{nc}\widehat{\rho}_{ci}^{3/2}\ \widehat{\rho}_{cm}\ \dot{\bar{\varepsilon}}_p; \tag{A.9}$$

$$\dot{\widehat{\rho}}_{xi}^{rm} = Mc_{xi}^{rm}\widehat{\rho}_{xi}\ \dot{\bar{\varepsilon}}_p; x = c, w; \tag{A.10}$$

The kinetic prefactors and exponents depend on temperature and strain rate through

$$c_{xy}^z = c_{xy0}^z\left[1 + r_{xy}^z(\widehat{T}-1)^{s_{xy}^z}\right]\dot{\widehat{\varepsilon}}_p^{m_{xy}^z},\ xy \in \{cm, ci,\ wi\}, \tag{A.11}$$

$$m_{xy}^z = m_{xy0}^z\left[1 + r_{z_{xy}}^m(\widehat{T}-1)^{s_{z_{xy}}^m}\right]; xy \in \{cm, ci,\ wi\}, \tag{A.12}$$

where $z$ indexes the mechanism (*gn, an, ac, tr, nc, rm*) and the subscript 0 denotes reference values at $T_0$ and $\dot{\varepsilon}_0$.

*Appendix A.4. Void fraction kinetics*

The three contributions to the void fraction rate are

$$\dot{f}_g = (1-f)tr\left[\dot{\underline{\varepsilon}}_p\right], \tag{A.13}$$

$$\dot{f}_n = A\dot{\bar{\varepsilon}}_p;\ A = \frac{f_N}{S_N\sqrt{2\pi}}\exp\left[-\frac{1}{2}\left(\frac{\bar{\varepsilon}_p - \varepsilon_N}{S_N}\right)^2\right], \tag{A.14}$$

$$\dot{f}_s = K_w' \cdot f \cdot \omega\left(\underline{\sigma}\right)\cdot\frac{s_{ij}\dot{\varepsilon}_{ij}^p}{\bar{\sigma}};\ \omega\left(\underline{\sigma}\right) = 1 - \left(\frac{27J_3}{2\bar{\sigma}^3}\right)^2, \tag{A.15}$$

$$K_w' = K_w.\Omega(\eta);\ \Omega(\eta) = \begin{cases} 1 & \eta < \eta_1 \\ \dfrac{\eta - \eta_2}{\eta_1 - \eta_2} & \eta_1 \le \eta \le \eta_2 \\ 0 & \eta > \eta_2 \end{cases};\ \eta = \frac{\sigma_h}{\bar{\sigma}}; \tag{A.16}$$

where $f_n$ is the volume fraction of nucleating particles, $\varepsilon_N$ and $S_N$ are the mean and standard deviation of the nucleation strain, $K_w$ is the shear damage parameter, $s_{ij}$ is the deviatoric stress, $J_3$ is the third deviatoric stress invariant, $K_w'$ is the triaxiality modified shear factor and η is stress triaxiality.

## Appendix B. Thermo-Physical properties of the investigated S700 steel

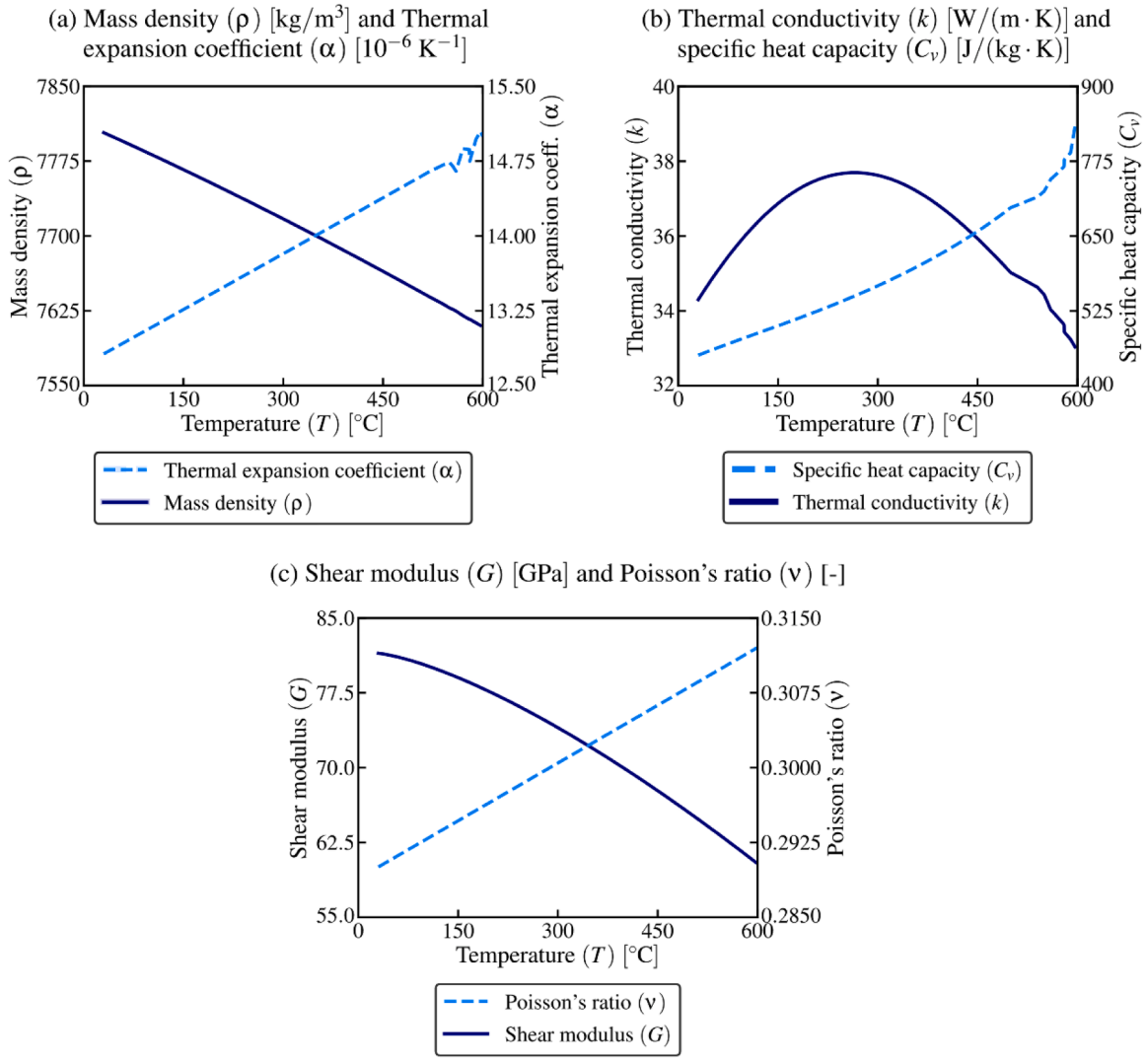



**Fig. B.1.** Thermo-Physical properties of the investigated S700 steel as a function of temperature [49].

## Appendix C. Constitutive model parameters

**Table C.1**
Reference parameters and independently measurable material constants used in the study.

| $T_0[C]$ | $\dot{\varepsilon}_0[s^{-1}]$ | $\rho_0[m^{-2}]$ | $M[-]$ | $b[m]$ |
|---|---|---|---|---|
| 25 | 0.1 | $10^{12}$ | 3 | $2.55 \times 10^{-10}$ |

**Table C.2**
Initial cell mobile, cell immobile, and wall immobile dislocation densities; viscous stress at reference conditions; and constitutive parameters related to the probability amplitudes of different dislocation processes, including mean interaction strengths for S700 steel.

| $c_{cm}^{gn}[-]$ | $c_{cm0}^{an}[-]$ | $c_{ci0}^{an}[-]$ | $c_{wi0}^{an}[-]$ | $c_{ci}^{ac}[-]$ | $c_{wi}^{ac}[-]$ | $c_{cm0}^{tr}[-]$ | $c_{wi0}^{nc}[-]$ |
|---|---|---|---|---|---|---|---|
| 2877.23 | 0.06004 | 0.09873 | 0.00984 | 8.20196 | 1.13865 | 1.60547 | 0.02423 |
| $c_{ci0}^{rm}[-]$ | $c_{wi0}^{rm}[-]$ | $\widetilde{\alpha}_{c0}[-]$ | $\widetilde{\alpha}_{w0}[-]$ | $\widehat{\rho}_{cm0}[-]$ | $\widehat{\rho}_{ci0}[-]$ | $\widehat{\rho}_{wi0}[-]$ | $\sigma_{v00}[MPa]$ |
| 11.049 | 0.02244 | 0.09901 | 0.31634 | 76.5583 | 228.333 | 342.86 | 344.263 |

**Table C.3**
Temperature sensitivity coefficients and exponents for the constitutive parameters and viscous stress of S700 steel.

| $r^{an}_{cm}[-]$ | $r^{an}_{ci}[-]$ | $r^{an}_{wi}[-]$ | $r^{tr}_{cm}[-]$ | $r^{nc}_{wi}[-]$ | $r^{rm}_{ci}[-]$ | $r^{rm}_{wi}[-]$ | $r^{G}_{\alpha c}[-]$ | $r^{G}_{\alpha w}[-]$ | $r_v[-]$ |
|---|---|---|---|---|---|---|---|---|---|
| 0.1744 | 0.654 | 1.2717 | 8.2286 | 0.7945 | 4.4965 | 4.5664 | − 0.6233 | − 0.0505 | − 1.9223 |
| $s^{an}_{cm}[-]$ | $s^{an}_{ci}[-]$ | $s^{an}_{wi}[-]$ | $s^{tr}_{cm}[-]$ | $s^{nc}_{wi}[-]$ | $s^{rm}_{ci}[-]$ | $s^{rm}_{wi}[-]$ | $s^{G}_{\alpha c}[-]$ | $s^{G}_{\alpha w}[-]$ | $s_v[-]$ |
| 4.0456 | 0.9959 | 1.4155 | 1.5952 | 3.9165 | 2.4535 | 8.0155 | 0.2449 | 1.2553 | 0.9363 |

**Table C.4**
Strain rate sensitivity coefficient along with its corresponding temperature sensitivity coefficient and exponent, and the dissipation factor.

| $m_{v0}[-]$ | $r^{m}_{v}[-]$ | $s^{m}_{v}[-]$ | $m^{m}_{v}[-]$ | $\kappa[-]$ |
|---|---|---|---|---|
| 0.0346 | 0.0785 | 5 | 0 | 2 |

**Table C.5**
GTN damage parameters calibrated for the D-TMM model.

| $f_0$ | $f_N$ | $f_C$ | $f_F$ | $q_1$ | $q_2$ | $q_3$ | $s_N$ | $\varepsilon_N$ |
|---|---|---|---|---|---|---|---|---|
| 0.00082 | 0.02872 | 0.05564 | 0.24025 | 1.66706 | 0.97297 | 2.779089 | 0.07575 | 0.1815 |
| $K_w$ | $\eta_1$ | $\eta_2$ | | | | | | |
| 0.5 | 0.8 | 1.3 | | | | | | |

## Data availability

Data will be made available on request.

## References


[1] Shakil S, Lu W, Puttonen J. Experimental studies on mechanical properties of S700 MC steel at elevated temperatures. Fire Saf J 2020;116:103157.
[2] Rashid MS. High-strength, low-alloy steels. Science 1980;208:862–9.
[3] Ma G, Gao B, Chen Z, et al. High-strength low-alloy steels for automobiles: microstructure and mechanical properties. Materials 2025;18:4660.
[4] Dalloz A, Besson J, Gourgues-Lorenzon A-F, et al. Effect of shear cutting on ductility of a dual phase steel. Eng Fract Mech 2009;76:1411–24.
[5] Wang K, Greve L, Wierzbicki T. FE simulation of edge fracture considering pre-damage from blanking process. Int J Solids Struct 2015;71:206–18.
[6] Uthaisangsuk V, Prahl U, Bleck W. Modelling of damage and failure in multiphase high strength DP and TRIP steels. Eng Fract Mech 2011;78:469–86.
[7] Overby D., Cathcart C., Yu X., et al. Edge stretchability of hot rolled high-strength low-alloy steel. In: *Contributed papers from materials science and technology 2019 (MS&T19)*. TMS, pp. 912–919.
[8] Kamibayashi K, Tanabe Y, Takemoto Y, et al. Influence of Ti and Nb on the strength–ductility–hole expansion ratio balance of hot-rolled low-carbon high-strength steel sheets. ISIJ Int 2012;52:151–7.
[9] Paul SK, Mukherjee M, Kundu S, et al. Prediction of hole expansion ratio for automotive grade steels. Comput Mater Sci 2014;89:189–97.
[10] Adamczyk RD, Michal GM. Sheared edge extension of high-strength cold-rolled steels. J Appl Metalwork 1986;4:157–63.
[11] Gläsner T, Sunderkötter C, Hoffmann M, et al. Zweistufiges Scherschneiden reduziert die Kantenrissempfindlichkeit. UTF-Sci forschungsmagazin für produktionstechnik. 2013. https://umformtechnik.net/content/location/72798.
[12] Comstock RJ, Scherrer DK, Adamczyk RD. Hole expansion in a variety of sheet steels. J Mater Eng Perform 2006;15:675–83.
[13] Centeno G, Silva MB, Cristino VAM, et al. Hole-flanging by incremental sheet forming. Int J Mach Tools Manuf 2012;59:46–54.
[14] Bambach M, Voswinckel H, Hirt G. A new process design for performing hole-flanging operations by incremental sheet forming. Procedia Eng 2014;81:2305–10.
[15] Levy BS, Gibbs M, Van Tyne CJ. Failure during sheared edge stretching of dual-phase steels. Metall Mater Trans A 2013;44:3635–48.
[16] Levy BS, Van Tyne CJ. Failure during sheared edge stretching. J Mater Eng Perform 2008;17:842–8.
[17] Hu XH, Sun X, Golovashchenko SF. Predicting tensile stretchability of trimmed AA6111-T4 sheets. Comput Mater Sci 2014;85:409–19.
[18] Ilinich AM, Golovashchenko SF, Smith LM. Material anisotropy and trimming method effects on total elongation in DP500 sheet steel. J Mater Process Technol 2011;211:441–9.
[19] Han S, Chang Y, Wang C, et al. Experimental and numerical investigations on the damage induced in the shearing process for QP980 steel. Materials 2022;15:3254.
[20] Ortiz-Membrado L, Parareda S, Casellas D, et al. High-speed nanoindentation and local residual stress analysis for cut edge damage in complex phase steels for automotive applications. Metals 2025;15:651.
[21] Larour P, Sandin O, Casellas D. Advanced cut-edge characterization methods for improved sheared-edge damage evaluation in high-strength sheet steels. Metals 2025;15:645.
[22] Paul SK. A critical review on hole expansion ratio. Materialia 2020;9:100566.
[23] Kim JH, Lee T, Lee CS. Microstructural influence on stretch flangeability of ferrite–martensite dual-phase steels. Crystals 2020;10:1022.
[24] Li Z, Liu L, Xue Q, et al. Study on microstructure characteristics and hole expansion mechanism of Ti–Nb–V microalloyed 900 MPa hot-rolled ferrite-bainite high hole expansion steel. J Mater Res Technol 2024;33:7469–81.
[25] Yoon JI, Lee HH, Jung J, et al. Effect of grain size on stretch-flangeability of twinning-induced plasticity steels. Mater Sci Eng A 2018;735:295–301.
[26] Paul SK. Effect of punch geometry on hole expansion ratio. Proc Inst Mech Eng Part B J Eng Manuf 2020;234:671–6.
[27] Shih H-C, Zhou D, Konopinski B. Effects of punch configuration on the AHSS edge stretchability. SAE Int J Engines 2017;10:2051–6.
[28] Ilinich A, Smith L, Golovashchenko S. Analysis of methods for determining sheared edge formability. Detroit, Michigan, United States: Epub ahead of print; 2011. https://doi.org/10.4271/2011-01-1062.
[29] Zhou M, Li Y, Hu Q, et al. Investigations on edge quality and its effect on tensile property and fracture patterns of QP980. J Manuf Process 2019;37:509–18.
[30] Sandin O, Larour P, Hammarberg S, et al. The influence of cut edge heterogeneity in complex phase steel sheet edge cracking: an experimental and numerical investigation. Eng Fract Mech 2025;322:111176.
[31] Ramalingam K, Schmid T, Hüsing F, et al. Thermo-micro-mechanical modeling of shear cutting and flange forming in S700 steel. Int J Mech Sci 2025:110764.
[32] Thipprakmas S, Phanitwong W. Finite element analysis of flange-forming direction in the hole flanging process. Int J Adv Manuf Technol 2012;61:609–20.
[33] Sartkulvanich P, Kroenauer B, Golle R, et al. Finite element analysis of the effect of blanked edge quality upon stretch flanging of AHSS. CIRP Ann 2010;59:279–82.
[34] Lin H-S, Lee C-Y, Wu C-H. Hole flanging with cold extrusion on sheet metals by FE simulation. Int J Mach Tools Manuf 2007;47:168–74.
[35] Hu XH, Sun X, Golovashchenko SF. An integrated finite element-based simulation framework: from hole piercing to hole expansion. Finite Elem Anal Des 2016;109:1–13.
[36] He J, Li S, Dong L. Experiments and FE simulation of edge cracking considering prehardening after blanking process. Int J Mater Form 2020;13:547–60.
[37] Park S, Cho W, Jeong B-S, et al. A dual-scale FE simulation of hole expansion test considering pre-damage from punching process. Int J Solids Struct 2022;236–237:111312.
[38] Li D, Wu H, Zhan X, et al. A new ductile fracture model for edge cracking prediction of ultra-high strength steel considering damage accumulation in blanking process. J Mater Eng Perform 2022;31:6880–90.

[39] Qian L, Ji W, Sun C, et al. Prediction of edge fracture during hole-flanging of advanced high-strength steel considering blanking pre-damage. Eng Fract Mech 2021;248:107721.
[40] Pham QT, Barlo A, Islam MS, et al. Uncertainty quantification for conical hole expansion test of DP800 sheet metal. Int J Mater Form 2025;18:5.
[41] Jeong K, Jeong Y, Lee J, et al. Prediction of hole expansion ratio for advanced high-strength steel with image feature analysis of sheared edge. Materials 2023;16:2847.
[42] Seyyedi SE, Gorji H, Mirnia MJ, et al. Prediction of ductile damage and fracture in the single- and multi-stage incremental hole-flanging processes using a new damage accumulation law. Int J Adv Manuf Technol 2022;119:4757–80.
[43] Motaman SAH, Schacht K, Haase C, et al. Thermo-micro-mechanical simulation of metal forming processes. Int J Solids Struct 2019;178–179:59–80.
[44] Amir H, Motaman S, Prahl U. Microstructural constitutive model for polycrystal viscoplasticity in cold and warm regimes based on continuum dislocation dynamics. J Mech Phys Solids 2019;122:205–43.
[45] Motaman S.A.H., Komerla K., Storms T., et al. Experimental and numerical investigation of dual phase steels formability during laser-assisted hole-flanging. Palermo, Italy, p. 060005.
[46] Chen T, Schmid T, Hüsing F, et al. Design of freeform optic module creating a ring-shaped laser beam profile for localized heating of sheet metals. https://www.wlt.de/sites/default/files/2023-09/Contribution_144.pdf; 2023.
[47] Min J, Wang J, Lian J, et al. Laser-assisted robotic roller forming of ultrahigh-strength steel QP1180 with high precision. Materials 2023;16:1026.
[48] Gunawan-Goullet De Rugy J, Hou Z, Gu Y, et al. Laser-assisted forming of ultra-high strength steels: a critical review of mechanisms, processes, and future directions. High-Temp Mater 2025;2:10017.
[49] Ramalingam K, Motaman SAH, Haase C, et al. Thermo-micro-mechanical modeling of plasticity and damage in single-phase S700 steel. Int J Mech Sci 2025;286:109909.
[50] Allison J, Backman D, Christodoulou L. Integrated computational materials engineering: a new paradigm for the global materials profession. JOM 2006;58:25–7.
[51] Allison J, Li M, Wolverton C, et al. Virtual aluminum castings: an industrial application of ICME. JOM 2006;58:28–35.
[52] Backman DG, Wei DY, Whitis DD, et al. ICME at GE: accelerating the insertion of new materials and processes. JOM 2006;58:36–41.
[53] Liu Z-K, Chen L-Q, Rajan K. Linking length scales via materials informatics. JOM 2006;58:42–50.
[54] Luo C, Hansson K, Song Z, et al. Modelling microstructure in casting of steel via CALPHAD-based ICME approach. Alloys 2023;2:321–43.
[55] Motaman SAH, Kies F, Köhnen P, et al. Optimal design for metal additive manufacturing: an integrated computational materials engineering (ICME) approach. JOM 2020;72:1092–104.
[56] Hürkamp A, Dér A, Gellrich S, et al. Integrated computational product and production engineering for multi-material lightweight structures. Int J Adv Manuf Technol 2020;110:2551–71.
[57] Schmitz GJ, Engstrom A, Bernhardt R, et al. Software Solutions for ICME. JOM 2016;68:70–6.
[58] Karhausen K, Kopp R. Model for integrated process and microstructure simulation in hot forming. Steel Res 1992;63:247–56.
[59] Pietrzyk M. Through-process modelling of microstructure evolution in hot forming of steels. J Mater Process Technol 2002;125–126:53–62.
[60] Khan D, Zagade P, Gautham BP. Integrated modelling of hot forging of low-alloyed steels for an ICME workflow. SN Appl Sci 2019;1:1358.
[61] Khan D, Gautham B. Integrated modeling of carburizing-quenching-tempering of steel gears for an ICME framework. Integrating Mater Manuf Innov 2018;7:28–41.
[62] Rudnizki J, Zeislmair B, Prahl U, et al. Thermodynamical simulation of carbon profiles and precipitation evolution during high temperature case hardening. Steel Res Int 2010;81:472–6.
[63] Laschet G, Shukla M, Henke T, et al. Impact of the microstructure on the U–O forming simulations of a ferrite–pearlite pipeline tube. Steel Res Int 2014;85:1083–98.
[64] Helm D., Butz A., Raabe D., et al. Microstructure-based description of the deformation of metals: theory and application. 63.
[65] Zhang H, Diehl M, Roters F, et al. A virtual laboratory using high resolution crystal plasticity simulations to determine the initial yield surface for sheet metal forming operations. Int J Plast 2016;80:111–38.
[66] Baiker M, Helm D, Butz A. Determination of mechanical properties of polycrystals by using crystal plasticity and numerical homogenization schemes. Steel Res Int 2014;85:988–98.
[67] Zhang K, Holmedal B, Hopperstad OS, et al. Multi-level modelling of mechanical anisotropy of commercial pure aluminium plate: crystal plasticity models, advanced yield functions and parameter identification. Int J Plast 2015;66:3–30.
[68] Han F, Diehl M, Roters F, et al. Using spectral-based representative volume element crystal plasticity simulations to predict yield surface evolution during large scale forming simulations. J Mater Process Technol 2020;277:116449.
[69] Zhang K, Holmedal B, Hopperstad OS, et al. Modelling the plastic anisotropy of aluminum alloy 3103 sheets by polycrystal plasticity. Model Simul Mater Sci Eng 2014;22:075015.
[70] Mirnia MJ. Microstructural damage analysis of AA6061-T6 sheet under different stress states using a crystal plasticity RVE model. Mater Today Commun 2026;54:115561.
[71] Butz A, Lossau S, Springub B, et al. On the modeling of dual phase steels: microstructure-based simulation from the hot rolled sheet to the deep drawn component. Int J Mater Form 2010;3:73–6.
[72] Tjahjanto DD, Eisenlohr P, Roters F. Multiscale deep drawing analysis of dual-phase steels using grain cluster-based RGC scheme. Model Simul Mater Sci Eng 2015;23:045005.
[73] Sobotka E, Kreyca J, Poletti MC, et al. Analysis and modeling of stress–strain curves in microalloyed steels based on a dislocation density evolution model. Materials 2022;15:6824.
[74] Shin S-H, Lee S-I, Hwang B. In-situ SEM/EBSD investigation of tensile deformation-driven microstructural changes in low-carbon HSLA steels with ferrite-bainite microstructures. Mater Charact 2023;206:113418.
[75] Brecher C, Schmid T, Krupp U, et al. Mikrostrukturbasierte simulation zum kragenziehen von ahss. Hannover: Europäische Forschungsgesellschaft für Blechverarbeitung e.V.; 2023.
[76] Tvergaard V. Influence of voids on shear band instabilities under plane strain conditions. Int J Fract 1981;17:389–407.
[77] Bachmann F, Hielscher R, Schaeben H. Texture analysis with MTEX – free and open source software toolbox. Solid State Phenom 2010;160:63–8.
[78] Lee E-H, Yang D-Y, Yoon JW, et al. Numerical modeling and analysis for forming process of dual-phase 980 steel exposed to infrared local heating. Int J Solids Struct 2015;75–76:211–24.
[79] Klápště D, Moravec J, Švec M. Effect of thermal cycle on grain growth kinetics and formation of CCT diagram of HSLA steel S700MC. JOM 2025;77:7828–41.
[80] Pantleon W. Resolving the geometrically necessary dislocation content by conventional electron backscattering diffraction. Scr Mater 2008;58:994–7.
[81] Calcagnotto M, Ponge D, Demir E, et al. Orientation gradients and geometrically necessary dislocations in ultrafine grained dual-phase steels studied by 2D and 3D EBSD. Mater Sci Eng A 2010;527:2738–46.
[82] Estrin Y, Kubin LP. Local strain hardening and nonuniformity of plastic deformation. Acta Metall 1986;34:2455–64.
[83] Mughrabi H. Dislocation wall and cell structures and long-range internal stresses in deformed metal crystals. Acta Metall 1983;31(9):1367–79. https://doi.org/10.1016/0001-6160(83)90007-X.
[84] Estrin Y, Tóth LS, Molinari A, et al. A dislocation-based model for all hardening stages in large strain deformation. Acta Mater 1998;46:5509–22.
[85] Chu CC, Needleman A. Void nucleation effects in biaxially stretched sheets. J Eng Mater Technol 1980;102:249–56.
[86] Nahshon K, Hutchinson JW. Modification of the Gurson model for shear failure. Eur J Mech - ASolids 2008;27:1–17.
[87] Nielsen KL, Tvergaard V. Ductile shear failure or plug failure of spot welds modelled by modified Gurson model. Eng Fract Mech 2010;77:1031–47.
[88] Nielsen KL, Tvergaard V. Effect of a shear modified Gurson model on damage development in a FSW tensile specimen. Int J Solids Struct 2009;46:587–601.
[89] Muljono D, Ferry M, Dunne DP. Influence of heating rate on anisothermal recrystallization in low and ultra-low carbon steels. Mater Sci Eng A 2001;303:90–9.
[90] Li P, Li J, Meng Q, et al. Effect of heating rate on ferrite recrystallization and austenite formation of cold-roll dual phase steel. J Alloys Compd 2013;578:320–7.
[91] Krupp U, Düber O, Christ H-J, et al. Application of the EBSD technique to describe the initiation and growth behaviour of microstructurally short fatigue cracks in a duplex steel. J Microsc 2004;213:313–20.
[92] Murakami Y, Beretta S. Small defects and inhomogeneities in fatigue strength: experiments. Models Statist Implic 1999;2:123–47.